Evaluating Aerial Ku-Band Radar Altimetry over Landfast First-Year Sea Ice

by

Paul Donchenko

A thesis
presented to the University of Waterloo
in fulfillment of the
thesis requirement for the degree of
Master of Science
in
Geography

Waterloo, Ontario, Canada

I hereby declare that I am the sole author of this thesis. This is a true copy of the thesis, including any required final revisions, as accepted by my examiners.

I understand that my thesis may be made electronically available to the public.

Abstract

Recent studies have challenged the assumption that Ku-band radar, used by the CryoSat-2 satellite altimetry platform, fully penetrates the dry snow cover of Arctic sea ice in the winter. There is also uncertainty around the proper technique for handling retracker threshold selection in the Threshold First-Maxima Retracker (TFMRA) method which estimates the ice surface elevation from the radar echo waveform. The purpose of this study was to evaluate the accuracy and penetration of the TFMRA retracking method applied to ASIRAS (an airborne version of CryoSat-2's SIRAL sensor) radar altimetry returns, investigate the effect of surface characteristics and explore methods for improving the accuracy.

The ice surface elevation estimate (s_r) from ASIRAS was evaluated by comparing to the snow surface measured by aggregating laser altimetry observations from the Airborne Laser Scanner (ALS), and the ice surface measured by subtracting ground observations of snow depth from the snow surface. Due to the lack of a surface that could be used to calibrate the ASIRAS and ALS elevations, the location of the waveform relative to the observed snowpack boundaries could not be reliably established. The accuracy, penetration and the effect of surface properties were examined by investigating patterns that were consistent among different alternative calibration methods.

The perceived penetration of the ice surface estimate s_r was found to increase with the retracker threshold and the function of the relationship dependent on surface properties. The slope of the trend was increased by a deformed ice surface, a deeper snow cover, an absence of salinity and a larger snow grain size. As a result, the ideal retracked threshold, one that would achieve 100% penetration, varies depending on properties of the surface being observed. Under conditions such deep snow or a large grain size, the retracked elevation s_r was found in some cases to not penetrate fully the snowpack. This would cause an overestimation of the sea ice freeboard and as a consequence, the sea ice thickness.

Results suggest that using a single threshold with the TFMRA retracking method will not yield a reliable estimate of the snow-ice interface when observed over an area with diverse surface properties. However, there may be potential to improve the retracking method by incorporating knowledge of the sensed surface. Characteristics of the waveform that described its shape, such as the return width and pulse peakiness, were found to

be correlated with the estimate error and penetration. These could be combined with remotely sensed surface properties, such as the ice deformity, to select an ideal retracker for individual returns with an additional offset to account for the incomplete penetration of Ku-band over appropriate surface characteristics.

Acknowledgements

This work could not have been possible without the help of the many wonderful people who have guided me on this journey. Richard Kelly was not only a supervisor who provided all the necessary resources, but an amazing mentor who has done his best to support me in the fulfillment of my academic goals and my personal growth. Josh King is a key collaborator who has provided guidance in every aspect of this research and was crucial in helping transforming small ideas into polished results. I would also like to thank Wesley Van Wychen, for his valuable insights, suggestions and discussion.

A special thanks to Environment and Climate Change Canada (ECCC) for funding and executing the 2014 Eureka campaign to collect the ground-based observations used in this study, and the European Space Agency (ESA) for funding and collecting the airborne data.

For their advice and support, I am also indebted to my friends, the outstanding researchers at the University of Waterloo, past and present, which include Aaron Thompson, Vicky Vanthof, Lindsay Wong, Qinghuan Li, Margot Flemming, Nastaran Saberi, Sabrina Li, Hongjing Chen and Gary Feng. Most importantly, I am grateful to my parents, Natalie and Paul, my brother Mike and my partner Weijing Su, for their unwavering support and confidence in my abilities.

Table of Contents

List of Tables

List of Figures

Chapter 1

General Introduction

The Arctic sea ice, in its remoteness, has been seen throughout most of human history as an untouchable wilderness and a permanent characteristic of the Earth. A growing body of research has revealed the sea ice to be a fragile environment, suffering rapid and accelerating deterioration caused by anthropogenic climate change (Notz and Stroeve, 2016). The extent and thickness of the sea ice fluctuates annually, with a maximum in March and a minimum in September. An analysis of multi-decadal sea ice trends, from submarine surveys in the late 1970s to present-day satellite observations, found a 10% loss in the extent of the Arctic sea ice winter maximum and more than 50% loss in the summer minimum (Serreze and Meier, 2019). In the same period, the average thickness of the ice at the end of the melt season has decreased by approximately 2 meters, or 66% (Kwok and Markus, 2018).

Starting in the early 2000s, the rate of decrease has accelerated, driven primarily by rapid losses of thick multi-year ice (Serreze and Stroeve, 2015). From 1999 to 2017, multi-year ice has lost 2 million square kilometers of extent (Kwok and Markus, 2018) and now makes up less than 40% of the ice cover, where it used to be 50 to 60% (Serreze and Stroeve, 2015). The acceleration of sea ice loss in the Arctic is likely caused by multiple compounding feedback mechanisms. Shrinking ice extent decreases the amount of high-albedo (reflective) cover over the ocean, increasing the amount of radiation absorbed and accelerating sea ice loss through rising Arctic ocean temperatures (Curry et al., 1995).

Reductions in sea ice thickness caused by warmer summer temperatures have made the ice floe more sensitive to climate forcing and increased inter-annual variations in both extent and thickness, which have made future predictions much more difficult (Serreze and Meier, 2019). These feedback mechanisms, along with other climate effects are responsible for the amplification of climate change in polar regions (Smith et al., 2018). Given the trend of CO2 emissions and rising temperatures, the Arctic was predicted to have nearly ice-free ($<$ 1 million km2) summers before the end of this century (Overland and Wang, 2013), but losses in recent years have been larger and the prevalence of thin seasonal ice has made future predictions even more challenging (Serreze and Stroeve, 2015).

Due to the amplification of rising temperatures in the Arctic, sea ice trends act as valuable indicators of polar and global climate (Serreze and Stroeve, 2015). Arctic sea ice is a critical component of the global climate system and its loss will affect ocean currents, atmospheric circulation, marine life and human activities. The freshening of the upper layer of the Arctic Ocean due to melting ice could reduce the transfer of heat through convection due the reduced salinity gradient of the water column, which may prevent gyre circulation and have consequences for the global thermohaline circulation (McPhee et al., 1998; Aagard and E.C.Carmack, 1989). Climate models have also indicated that a decline in sea ice concentrations could increase the prevalence of atmospheric circulation patterns resembling the Arctic Oscillation and North Atlantic Oscillation negative phases, resulting in older winters throughout Siberia and, large parts of Europe and North America (Vihma, 2014). Overland et al. (2015) found that Arctic melt has the potential to amplify extreme weather events at the mid-latitudes, such as snow storms and tropical storms.

Sea ice also plays an important role as a habitat for Arctic wildlife, and a northward shift of the marginal ice zone disrupts the complex ecosystem that keeps populations in balance (Descamps et al., 2017). Marine species such the ringed seal, bearded seal and walrus, all rely on thick, snow covered sea ice as a platform for breeding and buildings dens. Insufficient snow covers have resulted in pups being born exposed to the elements and a heightened mortality rate (Smith and Lydersen, 1991). Polar bears rely on sea ice to hunt seals and build up fat deposits for the winter. Without a thick ice and snow cover, they are unable to build dens for their cubs and nurse for a sufficient period of time (Freitas et al., 2012). Sea ice also provides a seasonal bridge along the migration routes that Arctic

animals, such as polar bears and reindeer, rely on for travel between breeding and feeding grounds (Derocher et al., 2011; Hansen et al., 2010).

Perhaps one of the most controversial implications of Arctic sea ice decline is its impact on human activities. The Northwest Passage (NWP) is a series of marine routes between north-western Canada and the north coast of Alaska that pass through the Canadian Archipelago. The routes vary depending on the annual sea ice conditions, but have often required moderate ice breaking capabilities (Liu et al., 2017). In 2007, the sea ice reached a sufficiently low extent as to allow for the passage of regular freighters and cruise vessels. With the impending losses in ice cover, an easily navigable NWP has become a lucrative possibility, saving 10 days for Europe to Asia trips and 4 days from trips across North American coasts (Melia et al., 2016). Advocates of NWP shipping have pointed to the potential fuel savings and carbon emissions reductions from shorter trips, but studies have estimated that pollutants and aerosols emitted from Arctic-going vessels can further damage the environment and offset those cost savings (Lindstad et al., 2016).

In the likely situation that the Northwest Passage becomes a regular shipping route, the long term scale and distribution of sea ice extent will be critical for both maintaining and monitoring the route to ensure minimal and impact on Arctic environment. Variability in the sea ice extent is driven by the magnitude of climate forces such as temperature and currents, but also by the properties of sea ice that make it sensitive to climate forcing (Serreze and Stroeve, 2015). As a result, models that produce accurate ice forecasts will require an estimation of ice thickness that not only covers the entire Arctic Ocean, but also describes its distribution at a high resolution (Serreze and Meier, 2019).

Distributed estimates of sea ice thickness at the Arctic scale require the use satellite platforms such as CryoSat-2. One of the current methods of estimating sea ice thickness is described by R. Kwok and G. F. Cunningham (2015) as the application of a hydrostatic equilibrium model to measurements of the elevation of the ice surface above the water and the depth of its snow cover. Snow depth is estimated using a climatology developed by Warren et al. (1999) based on Arctic surveys from 1954 to 1999, and is adjusted for a lower current-millennium snow depth by applying a coefficient determined from 2011 aerial surveys by Operation Ice Bridge (Laxon et al., 2013; Kurtz and Farrell, 2011). Ice freeboard is estimated by comparing ice and ocean surface elevations using the SIRAL

Ku-band (13.5 GHz) radar altimeter aboard the CryoSat-2 satellite platform.

Lab tests conducted in 1995 by Beaven et al. suggested that Ku-band radar should penetrate through dry snow and its primary return signal should be reflected from the ice surface. More recent studies carried out in the Arctic have found that Ku-band radar might not fully penetrate the snowpack and that the bulk of the return signal comes from above the ice surface (Willatt et al. 2011).

These findings were supported by Nandan et al. (2017a) who determined that the presence of first-year ice (FYI) snowpack salinity or contrast in density and grain size between snow layers could reduce the penetration of Ku-band radar such as CryoSat-2. Recent studies have highlighted the need for an improved understanding of how snow properties and ice surface characteristics such as salinity, roughness and grain size affect the scattering interface location of Ku-band radar (Kwok and Haas, 2015; Ricker et al., 2014).

1.1 Research Objectives

To improve the understanding of how the Ku-band signal from a radar altimeter (such as CryoSat-2) interacts with snow-covered Arctic sea ice, observations from radar and laser altimetry from an airborne platform are compared with coincident ground measurements of surface properties. The purpose of this study is to evaluate the accuracy of the ASIRAS radar altimeter, which serves as a proxy for the CrySat-2 SIRAL sensor, determine what characteristics affect its accuracy and if it can be improved. To accomplish this goal, the following objectives are set:

1. Evaluate ASIRAS Ku-band radar altimeter measurements of the snow-ice interface and quantify penetration into the snowpack
2. Investigate the effect of surface characteristics on the penetration and accuracy of the snow-ice interface elevation estimate
3. Explore methods of improving the accuracy of the elevation estimate using remotely sensed data that can be collected from a satellite and obtained at the Arctic scale

Chapter 2

Background

2.1 Arctic Sea Ice

2.1.1 Ice Structure

Ice is the solid form of water molecules whose constituents are two hydrogen atoms and a single oxygen atom, giving it the chemical formula H2O. The electron orbital configurations of hydrogen and oxygen cause them to form a polar covalent bond. The higher electronegativity of oxygen and lower electronegativity of hydrogen causes the two hydrogens to assemble on one side of the molecule and form a 104.5° angle with the oxygen atom. Due to their relative electronegativities, the hydrogen side carries a partial positive charge and the oxygen side a partial negative charge, causing the molecule to become polarized. In a compact, rigid structure, similarly charged components of the water molecules will repel, forcing them into a lattice arrangement where a single hydrogen atom will sit at the line between each two oxygen atoms within the lattice (Figure 2.1).

The structure of the ice lattice (or its absence) depends on the temperature and pressure of its environment, combinations of which are categorized into forms. The form I_h is the most common, and the one present in sea ice. Other forms are rare due to their exclusive occurrence under extreme conditions. In the lattice of I_h type ice, the molecules form

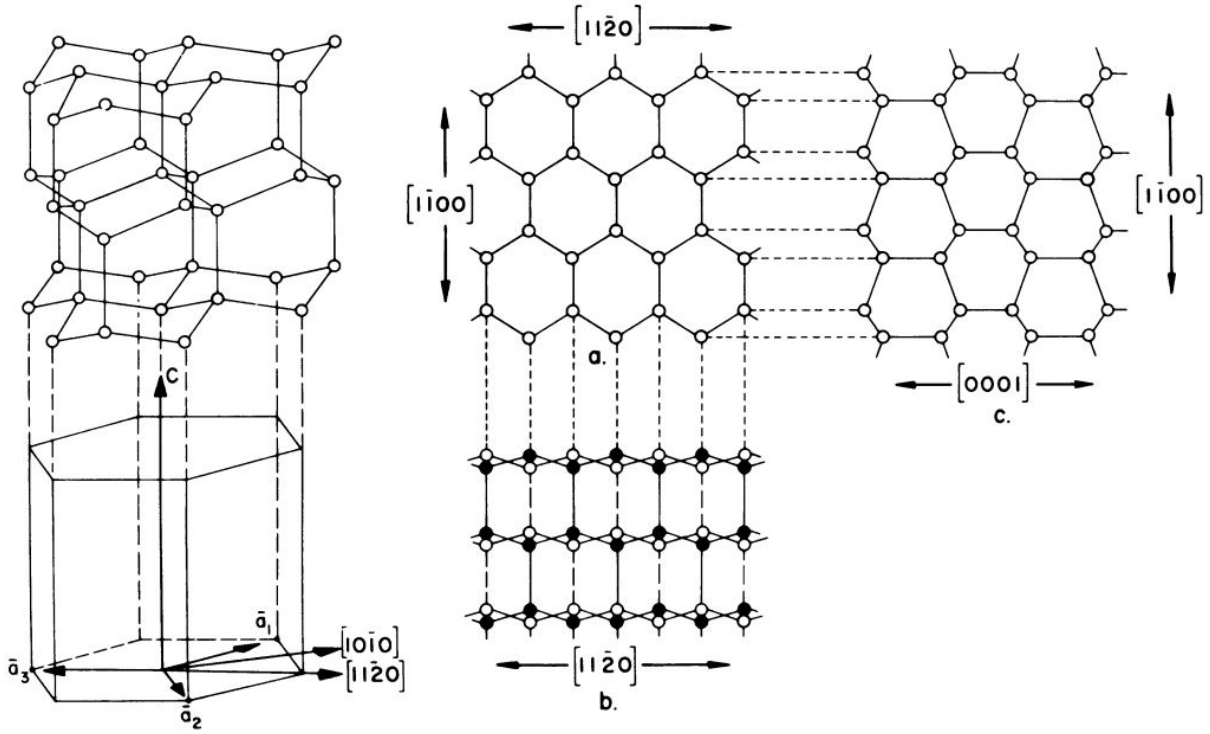

Figure 2.1: The molecular arrangement in the crystal lattice structure of ice I_h (Weeks and Ackley, 1986)

layers of tetrahedral arrangements that have hexagonal symmetry along the basal plane, marked by the a-axes in Figure 2.1. The c-axis, which is perpendicular to the basal plane, is known as the principal hexagonal axis. Unit layers along the basal plane are connected to each other by only two bonds, compared to the four bonds connecting units along the c-axis. The result is a weaker cohesion between layers and a vulnerability to shear forces along the basal plane. This structure also leads to significantly faster growth along the basal plane's six a-axes compared the c-axis, producing crystals that are flat and circular or hexagonally dendritic.

The lattice arrangement is sustained by the hydrogen bonds between adjacent hydrogen and oxygen atoms of different molecules, and allows for a greater distance between the water molecules than in their liquid state. This distance is responsible for the unusual

characteristic of ice's lower density than water. At temperatures above the melting point (0 °C at atmospheric pressure), the kinetic energy of the molecules is stronger than the hydrogen bonds, and the molecules fall out of alignment, moving closer together. At atmospheric pressure, the density increases with temperature until 3.8 °C, where thermal expansion will cause the density to decrease. This is a crucial property of sea ice because it both allows ice to float on water, and causes it to start forming at the surface and move downward.

2.1.2 Sea Ice Formation

Sea ice formation is initiated by the transfer of heat from the surface of a warmer ocean to the cooler and dryer air. Since the cooling of the water begins at the surface, an unstable vertical temperature and density gradient is formed that cool the top few meters of water to within a tenth to near freezing point. Once the surface layer is supercooled to just below freezing, ice crystal growth begins to accumulate around nuclei of impurities in the water. These crystals grow into thin circular disks, and upon reaching a maximum diameter of 2 mm to 3 mm, dictated by the thermal conductivity of the salt composition, collapse into smaller crystals, which then begin dendritic growth. Dendritic growth continues under calm seas, but water turbulence can result in inter-crystal collisions and friction, collapsing these structures.

The growth process generally occurs in three layers which are the surface layer, transition zone and the columnar zone. In the surface layer, small perturbations in the water will cause most of the flat, buoyant crystals to align their basal growth plane in parallel with the surface of the water. Crystals eventually intersect, forming flat continuous skims across the surface of the water. Turbulent sea conditions cause friction among colliding crystals, breaking the arms of their dendritic growth and forming frazil ice. This ice is formed of platelets and needles and has a slushy consistency that is easily deformed. Aggregations of frazil ice can form thin layers known as grease ice, and under lateral wave motion will cluster into thick-rimmed disks known as pancake ice, which can range from 30 cm to 3 m in diameter (Carsey, 1992). Rafting occurs when wave motion causes pancakes to collide and push over each other, forming thicker layers. Under calm sea conditions, the frazil ice can

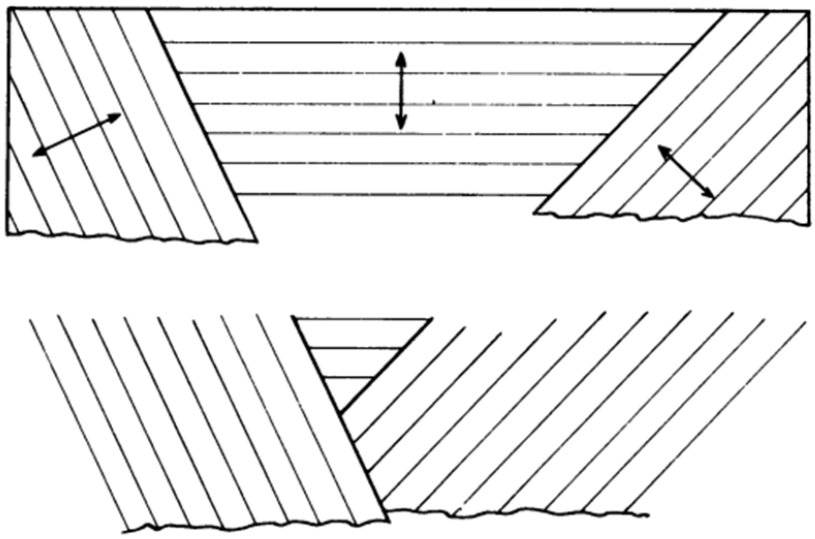

Figure 2.2: Representation of geometric selection, where crystals with vertically oriented c-axes (marked by arrows) intersect with their neighbours, cutting off their growth. This allows crystals with horizontally oriented c-axes to dominate the growth process. (Weeks and Ackley, 1986)

form dark floes of ice called nilas, which can be up to 10 cm thick. As freezing continues, sea ice fills the open water until it forms a continuous surface which can contains a mixture of forms, depending on the ocean conditions.

Once the growths converge, the interface between the bottom of the ice and water becomes insulated from the cold air. The freezing of seawater below the surface of a frozen floe is known as congelation growth. Newly developed crystals become trapped in their orientation, and those with horizontally oriented basal (primary growth) plane will collide with adjacent crystals, halting their expansion and favoring the growth of crystals with a vertically oriented basal plane (Figure 2.2). This process is known as geometric selection and occurs across a vertical distance of 5 to 10 centimeters in a layer known as the transition zone (Perey and Pounder, 1958). Vertical growth then occurs in the columnar zone where ice crystals form parallel sets of thin, vertical plates that can be tens of centimeters long.

Because the vast majority of dissolved salts present in seawater are not able to integrate

into the lattice structure of ice, salts are ejected from the ice as it growths. An increased salinity at the advancing edge establishes a vertical density gradient and induces convective mixing, transporting heat from lower layers up to the surface. The columnar plates tend to be oriented parallel to the direction of water currents as this enables the buildup of ejected salts to be transported from interface, speeding up growth (Weeks and Gow, 1978).

At the ice-water interface, the edges of the plates are tapered, with distances between the ends ranging from 0.1 to 1 mm (Figure 2.3b). The distance is dependent on the growth rate, with faster growth leading to larger gaps between the plates (Nakawo and Sinha, 1984). As the crystals grow and the plates expand, saline water remaining in the grooves becomes trapped and forms brine inclusions . The ejection of salts from the forming ice increases the salinity of the brine inclusions, lowering their freezing temperature and causing them to become constitutionally supercooled, which allows the brine to remain mostly liquid even as the ice is frozen (Weeks and Ackley, 1986). The vertical zone between the ends of the plates and the closing of the gap that traps brine can range from 1 to 3cm and is the known as the skeletal layer (Maykut, 1985).

The growth rate of the ice is dependent on the thickness and the temperature. As the ice becomes thicker, it becomes more difficult for heat from the ice-water interface to reach the top of the ice and be exchanged with the air. The growth rate decays exponentially until it reaches a thermodynamic equilibrium, where heat can no longer be lost (Figure 2.4). In the Arctic, this occurs at approximately 3 meters, although sea ice has been known to reach thermodynamic growth thicknesses of up to 12 meters (Weeks and Hibler, 2010) under rare conditions that are likely no longer present due to polar warming. Ice floes achieve these thicknesses over many years of growth, and ice within its first year of growth generally reaches a thickness between 30 cm to 100 cm (Maykut, 1985).

Wind and ocean currents affect the formation even after the surface has solidified. The majority of Arctic sea ice is in constant motion and cracks, known as leads, can form and expose the ocean surface. At the edge of the ice extent the floes are usually tens of meters in diameter, while closer to the poles, the ice is subject to less turbulence and floes can be kilometers across. The collision of floes can result in rafting and the formation stacks that can become thicker ice floes over time. This is one of the primary growth mechanisms after ice has reached its thermodynamic equilibrium (Weeks and Ackley, 1986).

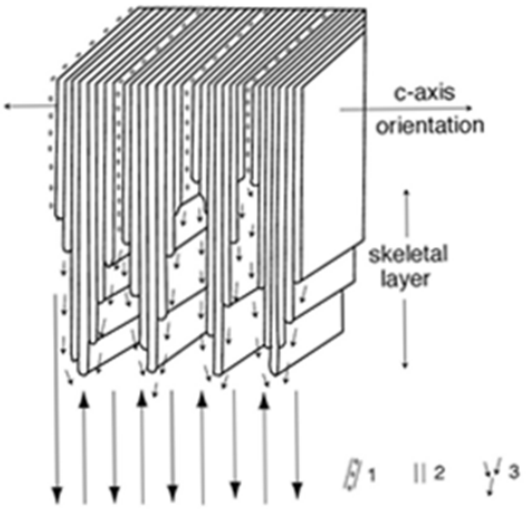

(a) (Maykut, 1985)

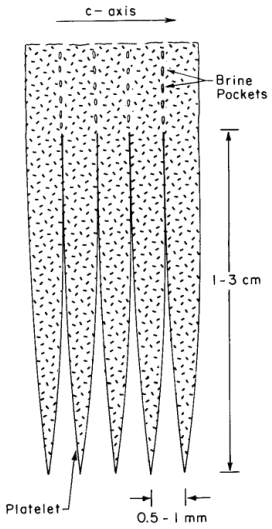

(b) (Weeks and Hibler, 2010)

Figure 2.3: The skeletal layer of the advancing ice column showing the inclusion of brine between the crystal plates.

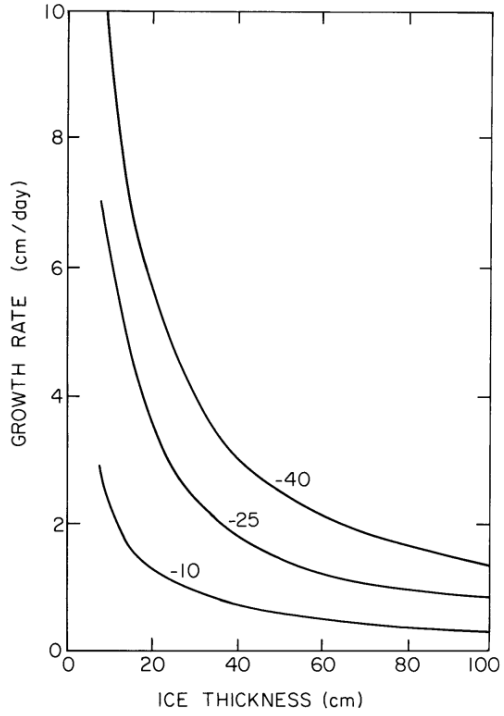

Figure 2.4: The exponential decay of ice thermodynamic growth rates for three temperatures in degrees Celsius as the thickness increases. (Maykut, 1985)

Colliding floes can also cause edges to break off and form large chunks of ice known as rubble, which forms piles called ridges. The ridges can span the full intersecting edges of adjacent floes, and can be kilometers long. The height of a ridge above the ice surface is referred to as the sail height. Ice that has survived multiple years of melt is more porous, breaks into smaller pieces and tends to form shorter sails than ice formed in the current season (Carsey, 1992).

2.1.3 Sea Ice Evolution

Newly formed brine inclusions are pressured by changes in temperature to move vertically within the ice floe. As ice cools the edges of the brine pocket freeze, increasing the pressure and forming cracks due to the expansion. Brine is expelled from the pocket and can move up through the ice layer. The brine can spill onto the surface of the ice, or wick upwards through a covering snowpack by way of capillary action. Because the top layers of ice are colder, the brine is denser and tends to drain downward through the more permeable lower layers of ice. As a result, the vertical profile of first year ice shows a minimum salinity in the center of the ice pack (Figure 2.5a-d).

Arctic sea ice formation in begins in the late fall and reaches a peak extent and thickness in early spring before the start of the melt season. Individual floes that have formed within the freezing season are known as first-year ice. Historically, around half of the ice present during the winter would melt during the summer, but the effects of Arctic warming have raised the percentage to two-thirds (Weeks and Hibler, 2010). First-year ice is particularly transient as the vast majority melts before the next freezing onset. First-year ice that survives into the early fall season is called multi-year ice.

During the summer, increased temperature causes sea ice to undergo changes that reduce its bulk salinity and deform its surface topography. Meltwater forms on the surface and drains into brine inclusions whose volume has also expanded due to the melting of its containing ice structure. Channels form between the inclusions and most of the brine is flushed out, with the remaining brine being mixed with meltwater, reducing its salinity. Air fills the gaps left behind by the brine, causing the ice to become porous (Weeks and Ackley, 1986).

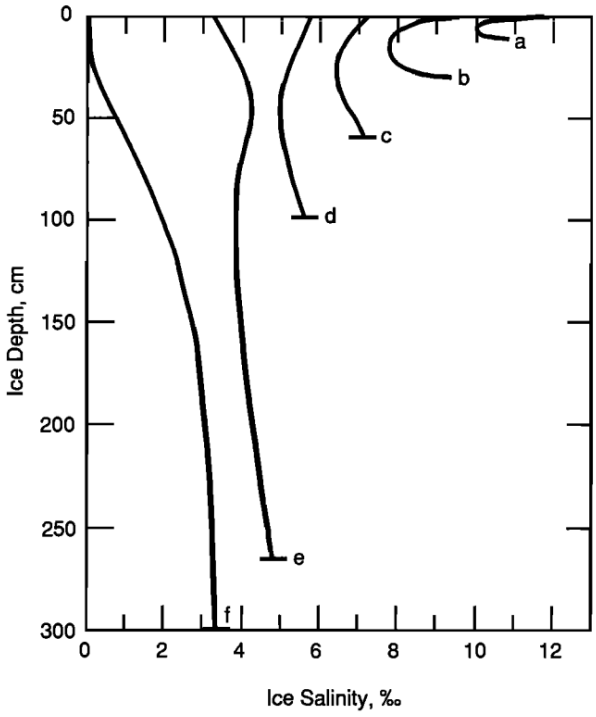

Figure 2.5: Vertical salinity profiles of various Arctic sea ice types. A-D: samples of first-year ice of increasing thickness. E: multi-year ice with a low freeboard. F: multi-year ice underneath a hummock (Maykut, 1985)

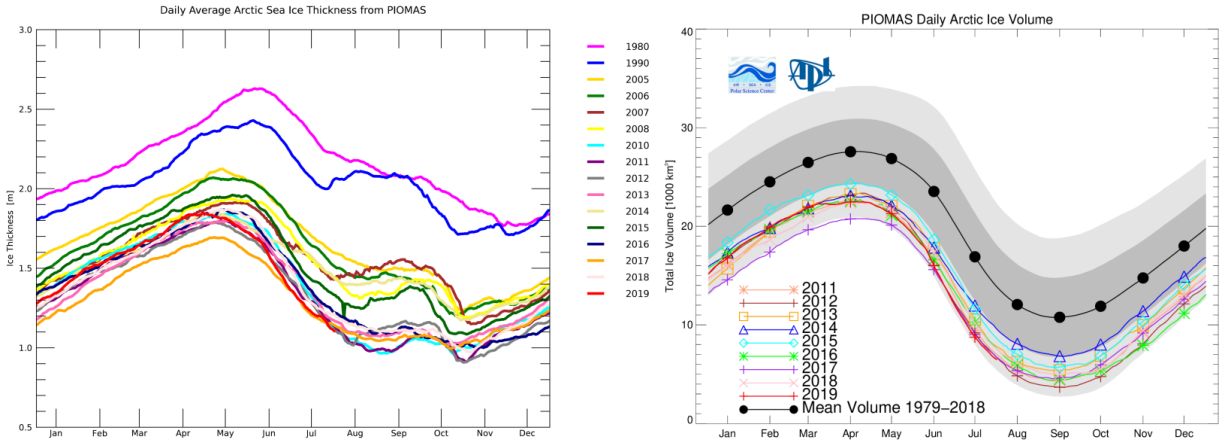

Figure 2.6: Seasonal fluctuations of Arctic sea ice thickness and volume from the PIOMAS model (Schweiger et al., 2019)

At the sea ice surface, meltwater pools into depressions called melt ponds that are 50cm to 1m deep (Carsey, 1992), absorb more solar energy than the ice and accelerate the melting process. By the end of the summer, melt ponds cover 10 to 30% of the Arctic sea ice surface (Maykut, 1985). Hummocks are bumps on the surface of the ice that can be caused by the adjacent melting of level surface, rubble or ridges, the latter of which form larger hummocks.

The transition from first-year to multi-year ice caused by repeated melt and refreeze cycles significantly changes the morphology of the ice. The surface of ice becomes rougher while the interior becomes more porous and less saline. By the start of the September freezing period, 40 to 70% of the ice volume has been lost and the average thickness reduced by 30 to 50% since the maximum in April (Schweiger et al., 2019).

Prior to the significant climate-change induced sea ice losses of the last three decades, multi-year sea ice covered a majority of the Arctic Ocean. Its area has decreased by slightly over 10% per decade from 1985 to 2017, falling from 7.5 to 4.5 million km^2 (Serreze and Meier, 2019). The oldest and thickest ice is now concentrated along the northern coasts of Greenland and the Canadian Archipelago (Figure 2.7).

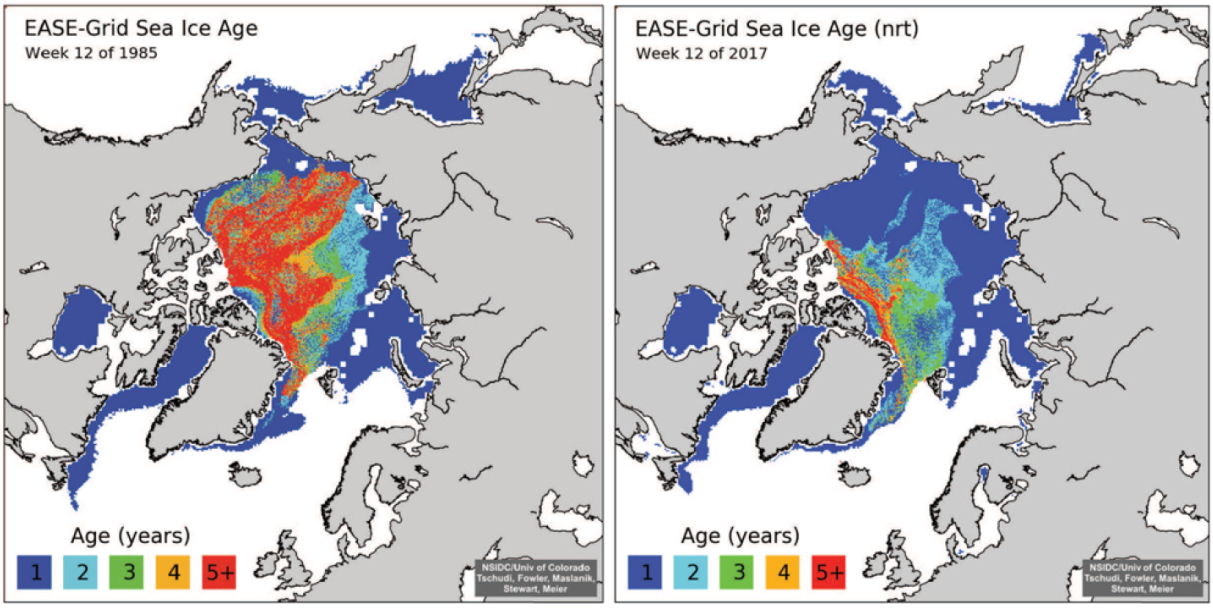

Figure 2.7: Spatial distribution of sea ice age in the Arctic during the end of March extent maximum in 1985 and 2017 (Serreze and Meier, 2019)

2.1.4 Snow on Sea Ice

The majority of snowfall in the Arctic occurs in the summer and early fall, when the surface of the ocean is uncovered by ice and acts as a source of moisture (Weeks and Hibler, 2010). When freezing first starts, snow crystals on the surface of the water provide a nucleation site for ice crystals to form (Weeks and Ackley, 1986). Snowfall accumulation begins over multi-year ice in the early freezing period when temperatures cool and over first-year ice once a stable surface of ice has formed. Warren et al. (1999) conducted surveys of the seasonal accumulations and distributions of Arctic snow in 1997-1998 and integrated their results to develop a model of Arctic snow cover that has been used by studies for the last two decades (Ron Kwok and G F Cunningham, 2008; Kwok et al., 2011; Jennifer King et al., 2018).

Results from the W99 study showed that snow buildup occurs most rapidly in the early season from August to November, gaining 15 to 25 cm on average. Once the ice becomes continuous and leads close up, snow accumulation slows down to 5 to 10 cm between November and May, until it melts again in the summer. Snow is deepest near the North coast of Greenland (8 to 46 cm) and shallower towards the Beaufort and Barents Seas (0 to 32 cm) (Figure 2.8). If a thick snow cover forms over thin ice, its weight can push the floe down and cause ocean water to flood the surface. Due to lower precipitation rates and thicker ice, it was previously understood that this occurrence in much rarer in the Arctic than the Antarctic (Thomas and Dieckmann, 2010), but the thinning of ice in the last decade has increased its frequency (Provost et al., 2017).

A study conducted between October 1998 and October 1999 as part of the Surface Heat Budget of the Arctic Ocean (SHEBA) program by Sturm et al. (2002) investigated the year-round stratigraphy evolution of the Arctic sea ice snow cover. Multiple deposition and storm events under varying environmental conditions result in a diverse range of layers being formed (Figure 2.9). The first layer was found to a be an approximately 10 cm layer of snow deposited before October and that had transformed into ice. Snow-ice production occurs when becomes soaked with rainwater, seawater from flooding, or meltwater, and refreezes to form a dense, ice-like layer. The majority of the snowpack was composed of depth hoar and wind slab layers that developed during short (less than 24 hours) but

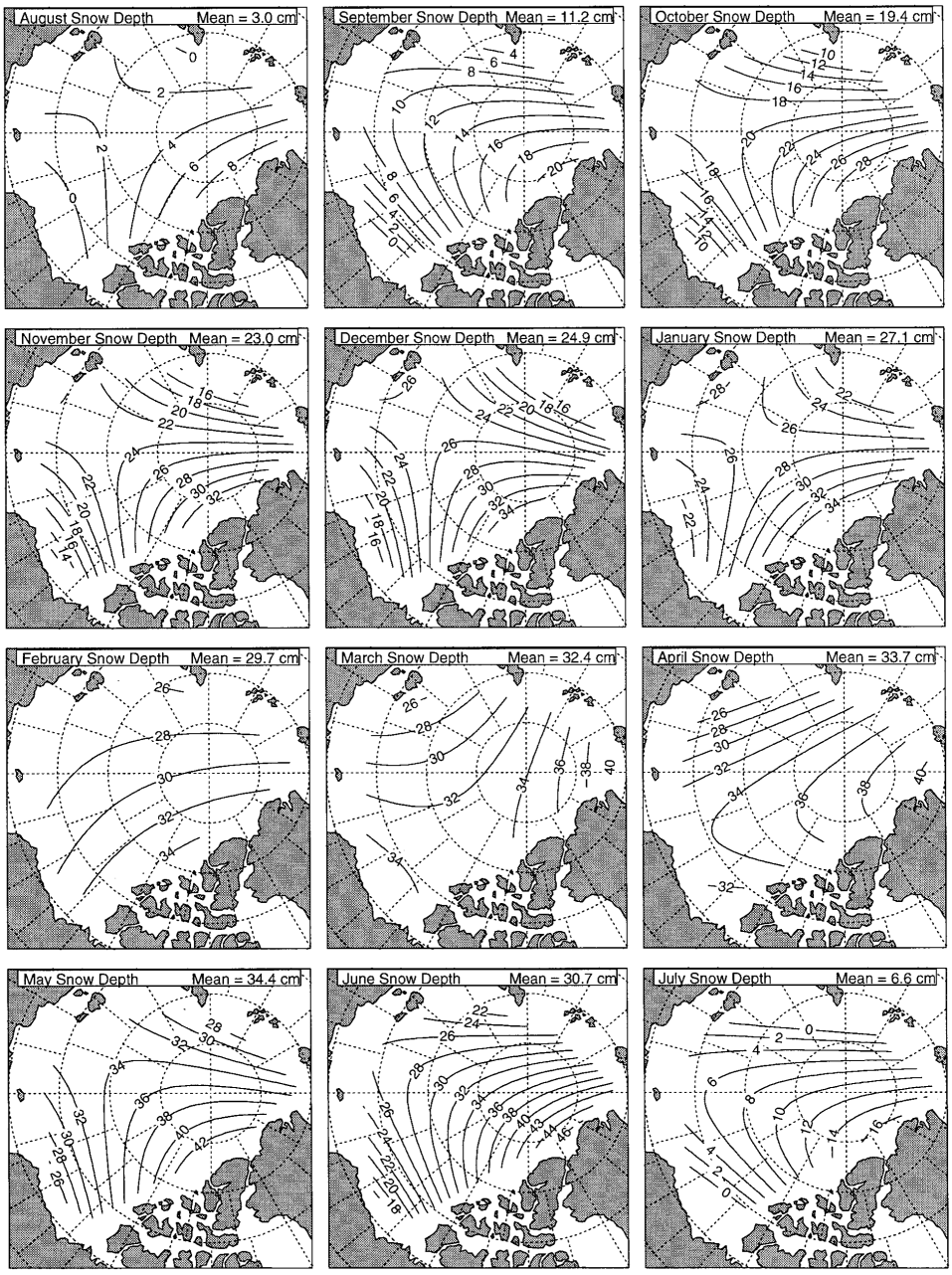

Figure 2.8: Interpolation of seasonal and spatial variations in snow depth in the Arctic based on observational data (Warren et al., 1999)

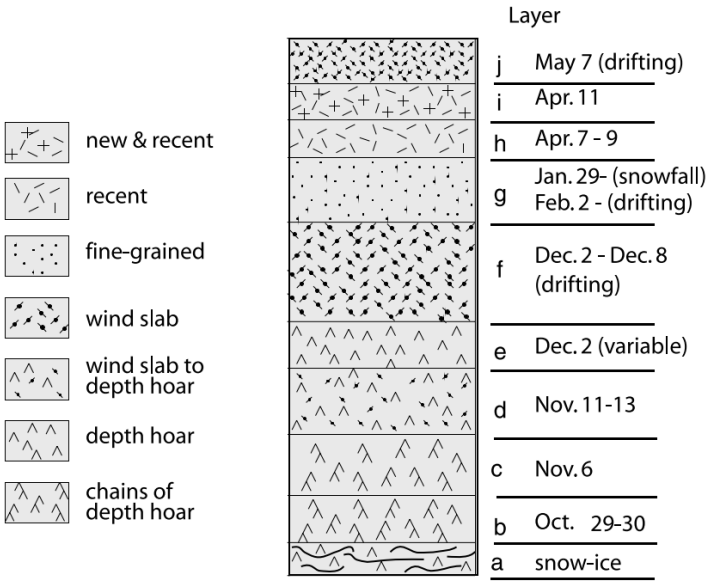

Figure 2.9: Generalized stratigraphy layers of a snowpack over Arctic sea ice observed between October 1997 and October 1998 by Sturm et al. (2002)

distinct storm events.

The lower layers were comprised of depth hoar that was deposited and formed between late October and late November. Depth hoar is a comprised of faceted crystals 5 to 15 mm in diameter that form a low density and brittle structure which is highly permeable and a good insulator. It is formed when snow crystals are subjected to a negative temperature gradient (colder at the surface than at the bottom) for a period of a week or more. Its resultant structure is dependent on the magnitude of the temperature gradient and wind speed conditions of its deposition (Akitaya, 1974).

The next layer consisted of wind slab which had formed in early December. Wind slab occurs when repeated collisions from high winds cause the edges of snowflakes to break off, reducing them to rounded grains approximately 0.3 to 0.8 mm in diameter. The crystals can come from either snowfall during the storm event or from uplifted surface snow. Within a few days of settling, surface heating will cause the grains to sinter and form a strong dense layer (Sturm et al., 2002).

2.2 Microwave Remote Sensing Principles

Microwave remote sensing is the observation of distant features by way of electromagnetic (EM) radiation in the spectrum of 300Ghz to 300Mhz (Hitchcock, 2004). The use of the microwave radiation confers two main advantages over other types of remote sensing: it can penetrate the atmosphere and does not require the sun as a source of illumination. The majority of the interaction between microwaves and remotely sensed features is governed by their electric permittivity ε, which describes how the material interacts with the electric field of propagating EM waves that pass through it and is dependent on the atomic structure and the organization of its electric charges (Woodhouse, 2006).

2.2.1 Permittivity and Emissivity

EM waves propagate through space as transverse waves that have both an electric and magnetic component whose amplitudes are perpendicular to each other and to the direction of propagation. As EM waves travel through matter they are affected by its electric permittivity ε and magnetic permeability μ. For the vast majority of features observed by remote sensing, their magnetic permeability contrast with that of free space is negligible $\mu \cong \mu_0$, so it is often ignored (Stiles and Ulaby, 1981).

ε is a complex number which has both a real component ε' and an imaginary component ε''. They can be referred to as dielectric constant and the loss factor respectively, though the terms are deprecated and not used in more recent literature, where ε is called the complex permittivity and ε' the permittivity (Carsey, 1992; Nandan et al., 2016). A higher ε' generally results in less penetration and more surface scattering, while a higher ε'' results in more absorption and transformation of EM energy into other sources such as heat (Shokr and Sinha, 2015).

$$\varepsilon = \varepsilon' - i\varepsilon'' \tag{2.1}$$

As electromagnetic (EM) radiation passes through a medium, its energy is lost through absorption and scattering. This loss is described by the extinction coefficient κ_e which

is the sum of the absorption coefficient κ_a and the scattering loss κ_s. Absorption is the transformation of the propagating energy into other forms such as heat and is a function of medium's ε_r. Scattering is the induced change in propagation direction of the energy caused by perturbations in the ε_r among the constituents of the medium (Carsey, 1992). The loss of propagating energy can also be described by the rate of exponential decay called the attenuation κ, which is dependent on the ε_r of the medium and the wavelength of the radiation (Woodhouse, 2006). Because the attenuation for microwaves through atmospheric gasses is low, the radiation experiences very small losses when passing through them. The attenuation will inversely affect the penetration depth, which is the distance that the EM wave will travel before its power is reduced by a factor of e and is a function of the relative permittivity ε_r and the wavelength λ. Woodhouse (2006) note that the penetration depths δ_p can be approximated by

$$\delta_p = \frac{\lambda\sqrt{\varepsilon_r'}}{2\pi\varepsilon_r''} \tag{2.2}$$

When an EM wave reaches the interface between two mediums with contrasting ε_r, part of the energy will be reflected while the rest will be refracted (Woodhouse, 2006). Specular scattering occurs over a flat surface and its resultant direction depends on the incidence angle. Diffuse scattering occurs over a rough surface, where a random topography will scatter uniformly, while a patterned surface with a regularity approaching the emitted wavelength, such as ocean waves, can create interference patterns (Carsey, 1992). If the surface is sufficiently rough or the incidence angle is low, a portion of the energy may be reflected back into the direction of the emitter, or into its future location if the emitter is coupled with a sensor and stationed on a moving platform such a plane or a satellite (Figure 2.11). This reflected energy is called the backscatter, and its received power relative to the emitted power and target area size is measured in dB as the backscatter coefficient σ^0 (Woodhouse, 2006).

Another key property of features measured in microwave remote sensing is the emissivity ϵ, which is the ratio of the temperature brightness of the feature and the brightness of a blackbody at the same temperature (Woodhouse, 2006). This property affects the amount of EM radiation a feature will emit, and allows it to be observed passively by sensors that

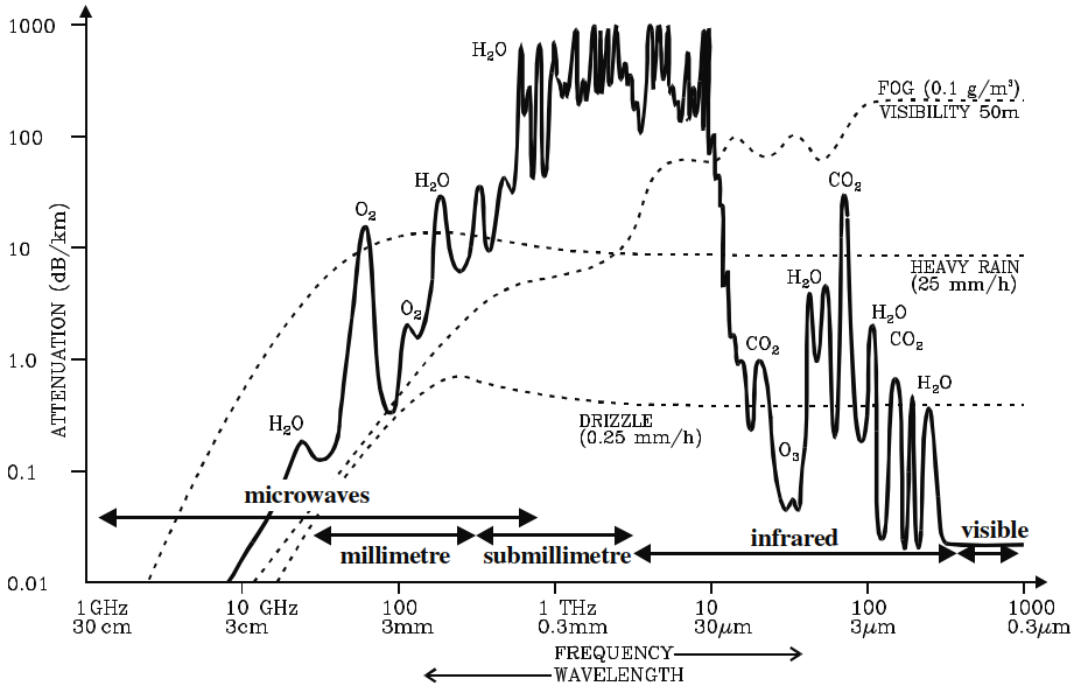

Figure 2.10: Attenuation of EM waves through different types of atmosphere. The solid dark line is for a nominally clear sky while dotted lines are for events where additional moisture is present. (Woodhouse, 2006)

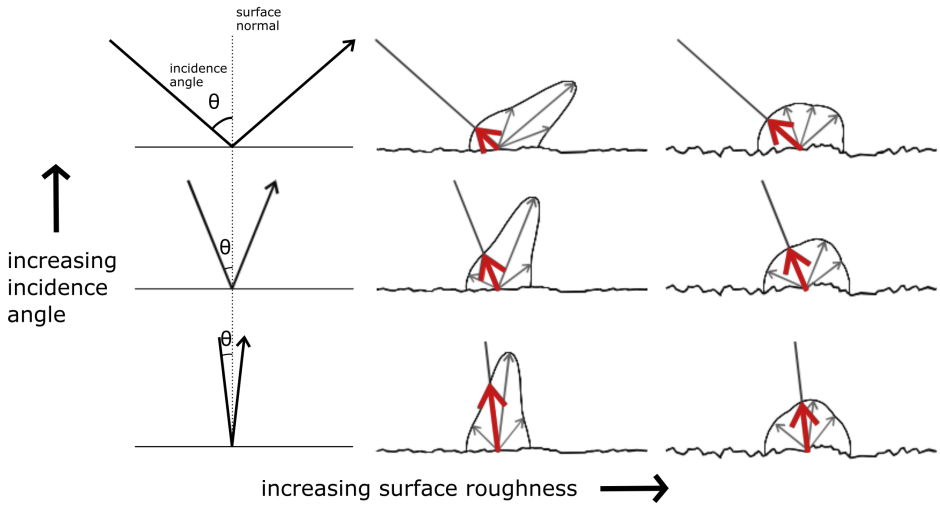

Figure 2.11: Surface scattering patterns for various incidence angles and surface topographies. Leftmost column shows specular scattering while the right two columns show diffuse scattering with the backscatter highlighted by a bolded red arrow. Adapted from Woodhouse (2006)

without having to emit any radiation. The radiation is emitted from a surface layer whose thickness is related to the penetration depth δ_p.

2.2.2 Polarization

EM waves are transverse, meaning that their amplitude is 2-dimensional along a plane perpendicular to the direction of propagation. If a wave only has amplitude along one axis of the plane, it is said to be linearly polarized in that direction and the angle of that axis relative to a reference plane along the direction of propagation is the orientation angle. Polarized waves can combine to form waves that are elliptically or circularly polarized and the combination of waves with a phase difference can result in a polarization whose orientation changes with propagation.

EM radiation that is emitted from energized volumes of matter, such as the fluorescent gas in light bulbs or the sun, comes from a larger number of molecules which have diverse orientations and whose emission is unpolarized. Remote sensing instruments can emit radiation by running an alternating current through a dipole antenna, which produces microwaves that are polarized in the direction parallel to the antenna. Waves emitted with no polarization that reflect from a flat surface can have their amplitude in the direction normal to the surface reduced, causing them to become polarized (Lacomme, 2001). The orientation of structures within a medium can also affect how it interacts with polarized waves, such as the selective reflectance of radio waves (Kovacs and Morey, 1978).

2.2.3 Characteristics of Sea Ice and Snow Cover

Like most natural materials, the interaction of sea ice and its snow cover with microwaves is governed by the relative permittivities of its constituents: air, ice, water and brine. The contrast between air and free space is very small, so it usually not considered (Stiles and Ulaby, 1981).

Pure ice has a static ε' and a very low ε'', resulting in an absorption of 0.09 dB/m and a penetration depth of approximately 100 m (Rees, 2006). Dry snow with few impurities

is primarily composed of ice crystals with pockets of air, and its properties are similar to those of pure ice. Empirical models fitted over observations show that the ε_r'' for dry snow increases with snow density and impurity concentration, decreases with temperature and has a minimum at 1 to 5 GHz (Mätzler, 1987). Hallikainen et al. (1986) have also found the a larger grain size in dry snow can also contribute to increased absorption. Because the loss factor of pure ice and dry snow is so low, interactions with microwaves are dominated by volume scattering (Rees, 2006). The penetration depth in dry cold snow can vary from tens of meters in the lower frequency C (4 GHz to 8 GHz) and L(1 GHz to 2 GHz) bands (Rignot et al., 2001) to only a few meters in the Ku band (13.5 GHz) (Rémy et al., 2015). Nandan et al. (2017a) found that the penetration of Ku, X and C-band radiation in snow covering sea ice was reduced by the presence of saline layer, and variations in grain size and density among its layers.

The permittivity for liquid water is at least two orders of magnitude higher than that of ice crystals due to its conductivity and the free motion of its polar molecules (Evans, 1965). The presence of dissolved salts in seawater increases its conductivity and results in a higher permittivity at frequencies below 10 GHz (Carsey, 1992). The ε_r' decreases with temperature, but stabilizes above 100 GHz while the ε_r'' has a maximum at approximately 1 GHz (Ulaby et al., 1982).

The dielectric properties of wet snow are determined primarily determined by its volume of water content and with a transition towards the properties of water at 0 °C as the water content increases (Hallikainen et al., 1986). The microwave penetration depth can range from 10 meters at 1 GHz to centimeters at 37 GHz (Figure 2.12a).

Due to the complex nature of sea ice and its diverse inclusions of constituents, the exact permittivity as a function of measurable properties such as salinity, temperature and density is difficult to model, with high variability among ice types. In a review of literature between 1971 and 1988, Rees (2006) found that permittivity decreased with temperature and was higher for first-year and newly formed ice (such as frazil) than for older multi-year ice due the latter's reduced salinity and porosity (Figure 2.12b).

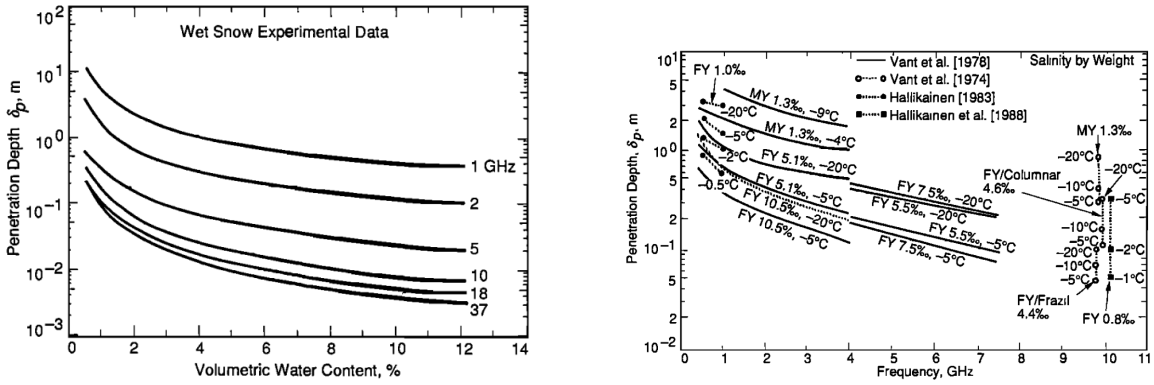

(a) (**Wet Snow**) (b) (**Sea Ice**)

Figure 2.12: Penetration depths of wet snow and sea ice and various type of sea ice. Compiled from a review of existing literature by Carsey (1992)

2.3 Microwave Remote Sensing of Arctic Sea Ice

Microwave remote sensing techniques usually acquire information about features through the use of two techniques: passive sensing by measuring their emitted microwave radiation, or active sensing by sending out microwave signals and measuring the backscatter returned from the target features.

The various surfaces of Arctic sea ice and its surrounding ocean have a diversity of microstructure, moisture content and temperature properties which affect their emissivities across the microwave spectrum. The value and distribution of these emissivities across the microwave spectrum can be used to distinguish surfaces using a passive microwave sensor. Recent studies have shown that data passive microwave sensors on satellite platforms can be used to estimate Arctic sea ice thickness (Naoki et al., 2008; Nakata et al., 2019), sea ice concentration (Ivanova et al., 2015), snow cover thickness (Maaß et al., 2013; Rostosky et al., 2018) and detect leads (Röhrs and Kaleschke, 2012).

The two main remote sensing techniques that use active microwave sensors are scatterometry and radar altimetry. In both cases, a short-duration pulse of microwave radiation is sent at a target and later received by an antenna over the same duration. Scatterometer instruments are tuned to obtain a high resolution cross section of the feature and have

been used to make inferences about snowpack structure (Frey et al., 2015) and classify sea ice (Brath et al., 2013), while altimeters are tuned to more accurately measure the range between the sensor and a target surface (Quartly et al., 2018).

2.3.1 Estimating Arctic Sea Ice Thickness

The investigation of changes in Arctic sea ice thickness and volume since 1958 by Kwok (2018) provide an overview of the methods that have been used to measure Arctic sea ice thickness for the past 70 years. The datasets are split into four main periods based on their collection method: two sets collected using submarines from 1958 to 1997, ICESat from 2003 to 2008 and Cryosat-2 from 2011 to 2017. The shift in methods from submarines to ICESat and then to Cryosat-2 was necessitated by the unavailability of submarine data after 1999 and the loss of ICESat in 2009.

Rothrock et al. (1999) combined data from multiple earlier studies that transcribed ice draft measurements collected almost annually from 1958 to 1997 by US Navy submarines as part of their regular navigation and reconnaissance activities. The ice draft is the height of the ice floe below the water surface and can be used to estimate the total ice thickness based on knowledge of its properties such as density, which were collected during a 1981 field campaign (Bourke and Garrett, 1987). The ice draft was measured using the upward-looking sonar sensors at the top of the submarine. Signals were manually interpreted to distinguish the bottom of the ice and the open water surface. The difference between these two ranges provided an estimate of the ice draft, whose error was later established to be approximately 25cm for each track (Rothrock and Wensnahan, 2007). Data from 1997 to 1999 was collected as part of the SCICEX program, a collaboration between the US navy and leading oceanographers in which annual submarine cruises were performed across the Arctic (Edwards and Coakley, 2003).

In the five year period between 2003 and 2008, ice thickness was estimated using a combination of ice surface measurements from ICESat, ice concentration from Aqua and snow depth based on precipitation estimates from weather forecasting (Ron Kwok and G F Cunningham, 2008). ICESat is a satellite platform carrying the GLAS laser altimeter. It uses a 1064 nm wavelength beam that has a 70 m footprint (with a 170 m spacing) and

an elevation measurement accuracy of 15 cm over sea ice (Ron Kwok, 2004). ICESat was used to measure the elevation of the air-snow interface over snow covered ice, the air-ice interface over bare ice and the sea surface elevation over open water relative to the TOPEX/POSEIDON ellipsoid.

The thickness of the snow cover was calculated by simulating the snow accumulation cycle based on precipitation estimates from the European Centre for Medium-Range Weather Forecasts (ECMWF). Snow could only accumulate over sufficiently dense ice floes, so ice concentrations and drift patterns were estimated using the Aqua satellite's AMSR-E 89-GHz channel radiometer (Ron Kwok and G F Cunningham, 2008). Based on the principles of hydrostatic equilibrium, the depth of the snow cover h_fs and height of the surface (including snow) above the sea surface h_f, can be used to estimate the thickness of the ice h_i (total freeboard) which is given by

$$h_i = (\frac{p_w}{p_w - p_i})h_f - (\frac{p_w - p_s}{p_w - p_i})h_{fs} \tag{2.3}$$

As constant value of 1024 kg/m^3 is used for water, the density of snow is obtained from Warren et al. (1999) based on the time of year and the density of ice a constant value of 0.925 obtained from Schwarz and Weeks (1977).

Estimating sea ice thickness from Cryosat-2 observations follows similar principles. Cryosat-2 carries the Ku-band (13.575 GHz) SIRAL sensor which has a radar footprint of approximately 0.31 km along-track and 1.67 km across-track. Due to the low ε_r of snow and its contrast with saline sea ice, Ku-band radar should pass through the snow and reflect strongly from the ice surface underneath. Early observations conducted under simulated sea ice conditions by Beaven et al. (1995) proposed that the primary scattering interface for Ku-band radar over snow covered sea ice is the snow-ice interface. Scattering would also occur at the air-snow interface and within the snowpack, but a simulation performed by Makynen and Hallikainen (2009) suggested that with Ku-band radar over sufficiently dry ($< 1\%$ volumetric wetness) snow, the magnitude of this secondary scattering would be low and the primary scattering of the snow-ice interface would still be discernible.

Prior to the expected and failed launch of the first CryoSat in 2005, an aerial mounted version of the SIRAL known as the Airborne Synthetic Aperture and Interferometric Radar

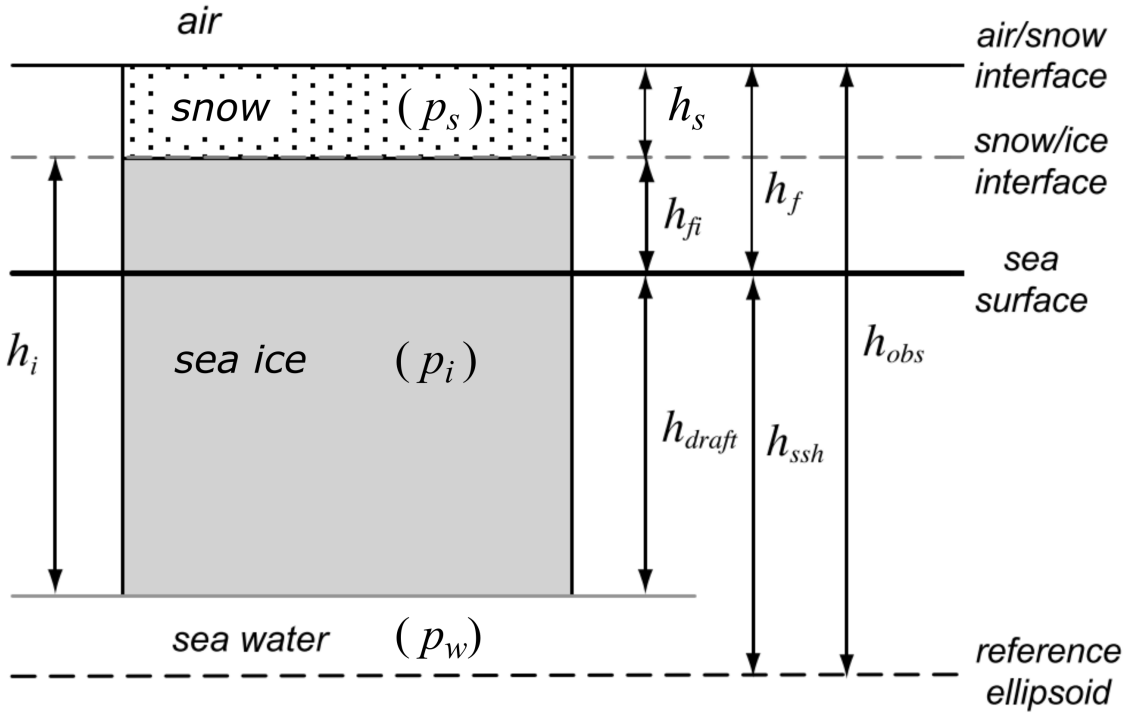

Figure 2.13: Schematic showing the components of sea ice with a snow cover floating in sea water. Vertical arrows are labelled with height variables and areas are labelled with density variables in brackets. Adapted from (R. Kwok et al., 2009)

Altimeter System (ASIRAS) was designed and deployed for the purpose of validating the unproven concepts of polar SAR/interferometric pulse-limited altimetry. Additional objectives included studying the Ku-band signal penetration into dry ice and providing data to optimize the signal processing algorithms (Lentz et al., 2002). Studies using ASIRAS over Arctic sea ice, found that Ku-band radar only partially penetrated the snow pack (Willatt et al., 2011; Hendricks et al., 2010). Data collection was performed in the late spring (April to May) with snow temperatures as high as $-4\,^{\circ}\mathrm{C}$, which could have reduced the penetration either through the presence of moisture or a reduced permittivity (Gerland et al., 2012). R. Kwok and G. F. Cunningham (2015) noted that scattering from the snow-air interface can widen the backscatter response and reduce the range towards the primary scattering surface, increasing the derived freeboard and overestimating the thickness of the sea ice. One method for reducing the effect of the scattering at the air-snow interface is known as threshold first-maxima retracker (TFMRA), which involves retracking the radar return to interpret the position of the snow-ice interface based on percentage (threshold) of the return power of the first peak (Helm et al., 2014). Ricker et al. (2014) analyzed the effectiveness of various thresholds, but found that the accuracy of individual selections varied across ice types and seasons.

Nandan et al. (2017a) investigated microwave backscatter over snow covered first-year ice and found that a reduced penetration of Ku-band radar could be caused by the presence of saline layers due to wicking and contrast in snow properties such as density and grain size between layers. Nandan et al. (2017b) proposed a method for correcting the impact of snow salinity on the Cryosat-2 freeboard retrieval by applying a thickness-dependent correction factor. Jennifer King et al. (2018) also found that the Ku-band radar primary scattering interface and that this could be responsible for an overestimate in the calculation of sea ice thickness from Cryosat-2 data. Recent studies have stressed the need for a better understanding of how Ku-band radar interacts with the diverse Arctic sea ice snowpack, and how these interactions vary across different regions and seasons (Jennifer King et al., 2018; Ricker et al., 2014; Kwok and Markus, 2018).

An investigation of current literature shows that there is potential for an improvement in the understanding of how Ku-band radar interacts with snow covered Arctic sea ice. The goal of this study is to evaluate how the accuracy and penetration of the ice surface

estimate based on the airborne ASIRAS radar altimeter, a proxy of the CryoSat-2 satellite's SIRAL sensor, changes with properties of the observed ice surface and its snow cover. This will be accomplished by comparing the ASIRAS signal with a measurement of the snow and ice surface from laser altimeter (ALS) and ground snow depth measurements.

Chapter 3

Evaluating Aerial Ku-Band Radar Altimetry over Landfast First-Year Sea Ice

3.1 Introduction

Arctic sea ice is the expanse of meters-thick ice floes that covers the ocean at the North Pole (Carsey, 1992). It experiences an annual growth and melt cycle, with thickness and extent reaching a peak in March, and a minimum September. Historically, the ice would extend down to a latitude of 45°N in March, and 70°N in September (Parkinson et al., 1999), but due to large scale decline of ice volume in the last few decades, the minimum extent of 1970s has become the current maximum (Kwok and Markus, 2018). Arctic sea ice is a critical component of Earth's climate system. The annual freeze and melt cycle has a strong influence on both ocean and atmospheric currents (Peings and Magnusdottir, 2014; Rosenzweig et al., 2019), and disruption of this cycle can cause shifts to more extreme weather patterns in other parts of the globe (Vihma, 2014).

The highly reflective surface of sea ice also moderates the amount of solar radiation absorbed by the ocean, and the loss of ice cover has increased the temperature of the

water, creating a feedback loop which has accelerated the loss of both sea ice thickness and coverage (Rosenzweig et al., 2019). Climatology models extrapolating on current trends have projected a nearly sea-ice free summer near the mid-21st century, but the uncertainty of these models is high due to internal variability of the Arctic climate (Serreze and Meier, 2019) and the omission of multiyear sea ice fluxes (Overland and Wang, 2013). Previous models have underestimated the scope of volume loss due to insufficiently dense or accurate measurements of sea ice thickness (Serreze and Stroeve, 2015) and the inclusion or improvement of these measurements would significantly improve the accuracy of the projections (Day et al., 2014).

Sea ice thickness can be estimated by applying the principles of hydrostatic equilibrium to measurements of the sea ice height above the ocean (freeboard), the density of sea ice, ocean water and the density and thickness of the snow covering the sea ice (Forsström et al., 2011). A current method of obtaining Arctic Ocean scale estimates of sea ice thickness is to measure the sea ice freeboard using CryoSat-2 and snow depths from the W99 (Warren et al., 1999) climatological study (Laxon et al., 2013). Estimates based on the W99 model may no longer be representative of the current Arctic snow cover due to recent changes in the Arctic climate system (Webster et al., 2014), so reduction coefficients of 0.5 to 0.7 have been applied to the snow depth over first-year ice based on the results of Operation Ice Bridge (OIB) Arctic campaigns (Ron Kwok et al., 2017; Laxon et al., 2013; Kurtz and Farrell, 2011).

CryoSat-2 is a satellite radar altimeter whose Ku-band (13.5 GHz) signal is expected to scatter from the snow-ice interface and identify the elevation of the ice surface (Laxon et al., 2013). This assumption has been challenged by recent studies which suggested that when observing snow-covered sea ice, the dominant scattering return of the Ku-band may come from within snowpack, likely due to perturbations of snow properties such as salinity and grain size (Jennifer King et al., 2018; Nandan et al., 2017a; Nandan et al., 2017b). Since the basin-scale sea ice thickness estimates calculated from CryoSat-2 observations are critical for projecting changes in Arctic sea ice, it is important to both quantify and improve its accuracy as much as possible, which is the purpose of this study. To accomplish this goal, the following objectives are set:

1. Evaluate ASIRAS Ku-band radar altimeter measurements of the snow-ice interface and quantify penetration into the snowpack

2. Investigate the effect of surface characteristics on the penetration and accuracy of the snow-ice interface elevation estimate

3. Explore methods of improving the accuracy of the elevation estimate using remotely sensed data that can be collected from a satellite and obtained at the Arctic scale

3.2 Data and Methods

This study compares radar and laser altimetry with ground observations collected over land-fast first-year sea ice near Eureka, Nunavut, Canada. Altimetry data were collected by the European Space Agency during the CryoVEx 2014 Arctic campaign and ground observations were collected between March 24th, and April 2nd, 2014 by Environment and Climate Change Canada (ECCC).

A Twin Otter aircraft carrying the Airborne SAR/Interferometric Radar Altimeter System (ASIRAS) and Airborne Laser Scanner (ALS) flew a path coinciding with the ECCC ground campaign on March 25th 2014, at an altitude of approximately 350 meters and a ground-reference flight speed of 250 m/s (Hvidegaard et al., 2014). The flight produced 66,120 radar returns and 10,078,030 ALS points along an approximately 43 km long track. ALS is a 904 nm wavelength (Near Infra-Red) Reigl laser scanner with a horizontal resolution of 70 cm by 70 cm and a vertical accuracy of 10 cm (Hvidegaard et al., 2014). The position of the aircraft measured relative to the WGS84 ellipsoid using a combination of two Global Positioning System (GPS) antennas and an Inertial Navigation System (INS) whose combined accuracy is 2 cm (Hvidegaard et al., 2014). The ASIRAS altimeter has a vertical range resolution of approximately 10 cm, but the primary uncertainty of its measurements comes from the interpretation of the radar waveform return (Ricker et al., 2014).

The ALS points covered a width of approximately 150 m across-track. ASIRAS is a 13.5 GHz (Ku-band) radar altimeter with a footprint width of 20 m across and 3 m along

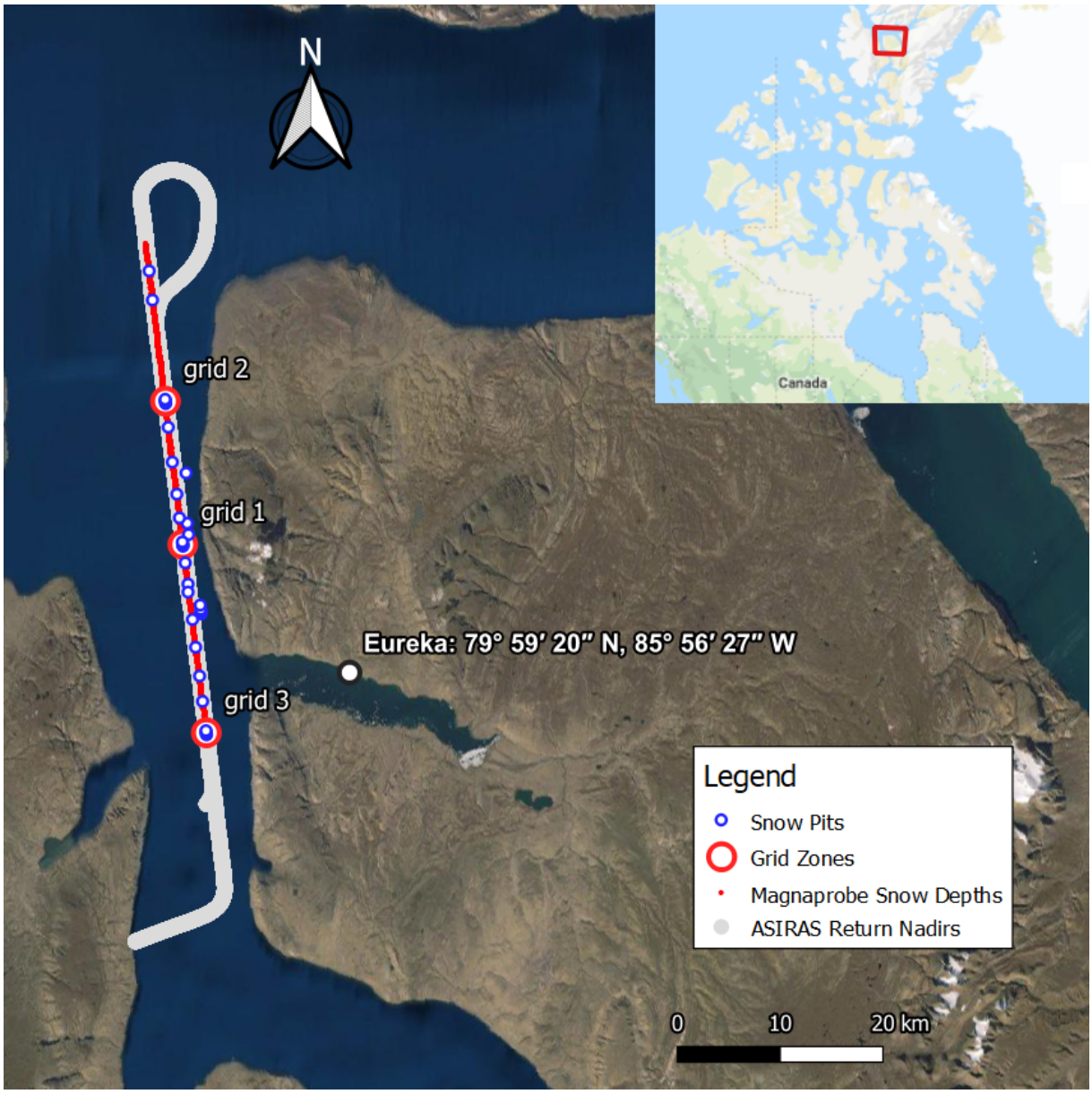

Figure 3.1: Study area map showing dataset locations. ASIRAS returns collected by the Twin Otter flight are in light grey. Snow depth observations collected by ECCC magnaprobes are in red and snow pits in blue. The research and weather station at Eureka, Nunavut is approximately 13 km West of the flight path.

track when flown in low-altitude mode at 300 m above ground. The electromagnetic properties of the instruments allow the laser scanner to measure the surface of the snowpack and the radar altimeter to penetrate the snow and measure the elevation of the snow-ice interface. The elevations of these surfaces can then be compared to obtain the snow depth over sea ice, which is then used to model sea ice thickness (Kurtz et al., 2013).

Ground observations were collected between March 26th and April 3rd, 2014 by ECCC over a 46 km path following the CryoVEx flight line (Joshua King et al., 2015). Snow depth measurements were collected using Snow-Hydro Magnaprobes supported with Global Positioning System (GPS) sensors with a horizontal accuracy of 2 m. A total of 37,320 collocated measurements were obtained at a spacing of approximately 2 m along the flight line track, with transects branching out orthogonally at random intervals at lengths of up to 100 m.

An additional 20,440 measurements were collected from three zones situated approximately 1 km, 18 km and 31 km North of the start of the track. Each zone was a measurement grid of 21 lines covering 500 m along the track and 14 lines covering 250 m across-track. Measurements of snow density were obtained using ESC30 gravimetric snow samplers at 174 points along the track, spaced between 200 m to 1 km apart. An additional 54 points were obtained at the same 3 zones as the snow depths, in grids of 3 lines along and 6 lines across-track.

Vertical profiles of the snowpack properties were collected by digging 37 pits along the course of the track, 13 of which were within 10 meters of a radar altimeter nadir. Density profile measurements were made using a 100 cm^3 box-style cutter and weighed with a hanging scale. The uncertainty of the density measurement process is expected to be 8 % but could potentially be larger due to the use of a hanging weight scale (Joshua King et al., 2018). Temperature was measured by a rod with embedded 10K thermistors at 4cm increments. A YSI EcoSense EC-300A sensor was calibrated in prepared solution of saline water that simulated the properties of seawater and used to measured the salinity with an accuracy of $\pm$ 0.2 PS. The pit stratigraphy profile and layering was determined by manually inspecting the snowpack and with a finger hardness test. Grain sizes and classifications were determined by selecting 3 grains deemed to be representative of the layer and measuring their small and largest diameters using a 2 mm compactor card and a

field microscope.

Nandan et al. (2017a) identified that the snowpack parameters which had the most impact on the Ku-band microwave penetration were the snow salinity and snow grain size, followed by the density and temperature. These properties were measured as vertical profiles using snow pits. Ideally, the profile layers could be matched up with radar altimeter echoes collected in proximity of the snow pits. Due to uncertainties in determining the sensor offset, such an alignment was not feasible, so the snowpack properties were summarized, per pit and correlated with the error and waveform shape measurements for returns within whose footprint each pit was located.

Salinity was summarized by calculating whether any saline layers (PSU > 0) were present in the target snowpack and by averaging the salinity for all layers in the snowpack. For the grain size, the minimum and maximum grain diameters across all snow grain samples in the pit were averaged for each pit, with an additional ratio of the min/max diameter averaged for each pit to represent the general roundness of the grains. Nandan et al. (2017a) noted that perturbations of snow properties (e.g. grain size, snow temperature) between snowpack layers caused scattering above the snow-interface, so the variance of the properties was also summarized for each pit. The variance for snowpack salinity was not calculated since pits would have at most 3 saline layers, and including this measurement would require more detailed slices of snow layers. The mean and variance of the snow density and temperature was similarly summarized for each pit.

The 2014 ECCC study also produced a grid of 8 m resolution square cells covering the study area. This grid provided a binary classification of whether the ice was deformed by classifying RADARSAT-2 C-band radar scenes using a K-means binary reclassification based on *a priori* knowledge (Joshua King et al., 2015).

In order to assess the accuracy of ASIRAS in mapping the snow-ice interface, the radar waveform was retracked to estimate the elevation of the interface within the echo. The elevation was then compared to the observed elevation of the ice surface, which was obtained by subtracting the snow depth from the snow surface elevation. The standard for retracking Ku-band sea ice altimeter waveforms was the threshold first maxima re-tracker (TFMRA). This method finds a point on the echo with a value equal to a given percentage

(threshold) of the maximum echo value, and that is the closest such point on the leading edge of the waveform, which is the left side of the first instance of the echo's maximum value. An example of a leading edge is marked in blue in Figure 3.2.

The threshold percentage can vary from 40 % to 80 % (Ricker et al., 2014), but 40 % has been shown to reduce the influence of volume scattering in both the ASIRAS and Cryosat 2 platforms (Jennifer King et al., 2018). To evaluate the effect of the TFMRA threshold selection on the error, thresholds of 20 % to 100 % (at peak value) at a 10 % interval were used. The plane carrying the sensor platform can be subjected to variations in pitch and roll, causing the sensor target to deviate from the nadir. These deviations can result in waveform blurring and errors when retracking elevations. To reduce these errors, returns with a roll or pitch deviation greater than 1.5° are excluded from the analysis (Jennifer King et al., 2018).

The ASIRAS return can also be characterized by the shape of the waveform, which can be described by measuring the return width (RW) and pulse peakiness (PP). The return waveform is composed of echoes from various scattering interfaces that the radar signal encounters as well as noise caused by the sensor's operation. One method for distinguishing the return from the base noise level is by locating the left and right edge of the return, which are the points on the leading and trailing edges that are 1 % of the peak value and are closest to the peak (Zygmuntowska et al., 2013). The distance between the peak and these respective points is the left and right RW, while their sum is the full RW.

The PP is generally calculated as the ratio between the maximum echo return power and either the sum or the mean of the total echo power. The PP value can be used to indicate a specular surface scatter (high PP) or a diffuse surface scatter (low PP), and is commonly used to distinguish between open ocean, leads and sea ice (Peacock and Laxon, 2004). A modified left and right PP can also be calculated as the average between the PP of the three bins left and right of the peak, and was originally done to identify echoes that were adjacent to a lead (Ricker et al., 2014). Although data in this study has no leads, the left and right PP measures may have potential in identifying returns that are adjacent to a deformed ice zone, which could also have off-nadir effects on the waveform. The PP and RW measures of the waveform shape have primarily been used to classify returns as leads or different types of sea ice (Ricker et al., 2014).

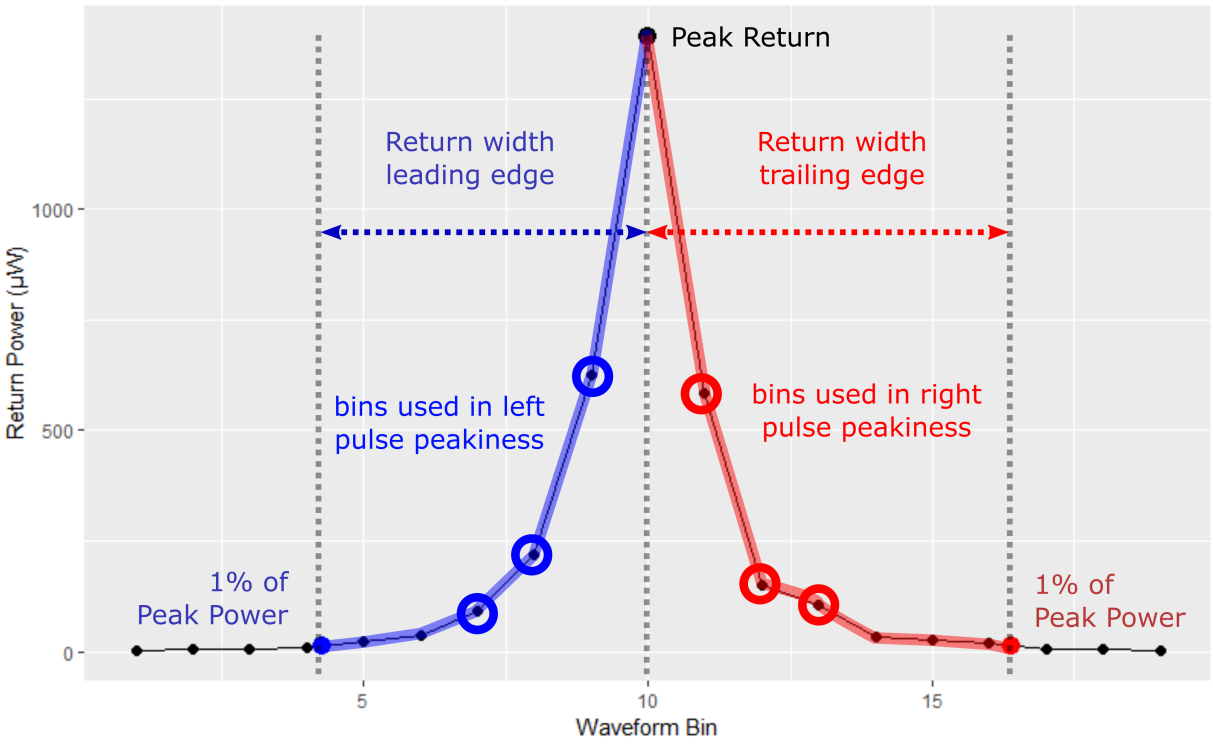

Figure 3.2: A typical ASIRAS echo waveform with the leading edge marked in blue and the trailing edge marked in red. The circled points are the bins used to calculate the left and right PP.

While the study only covers landfast first-year sea ice, the measurements' parameterization of the waveform may be beneficial due to the known effect of surface roughness on the shape of the waveform (Makynen and Hallikainen, 2009). Surface characteristics can have a left or right bias in their effect on the waveform, so an additional ratio (left/right) measurement was calculated for both the left and right RW and PP.

The ice surface elevation for each return is calculated by aggregating snow depth and snow surface elevation point measurements within a given footprint centered around the radar altimeter nadir. The size and shape of the footprint may be calculated based on the flight and sensor properties (Willatt et al., 2011) or by applying a circular footprint with a static radius from the nadir (Jennifer King et al., 2018). Since the sensor used in the

ASIRAS radar altimeter is based on the SIRAL sensor used in Cryosat 2, its footprint can be estimated using the same principles (Mavrocordatos et al., 2004).

Zone	Snow Depth (cm)			Snow Surf. Elvtn. (m)			Ice Surf. Elvtn. (m)			Snow Dens. (kgm^{-3})		
	n	$\bar{x}$	σ	n	$\bar{x}$	σ	n	$\bar{x}$	σ	n	$\bar{x}$	σ
Grid 1	8822	16.0	4.5	35044	6.71	0.08	8822	6.56	0.09	20	317.68	32.08
Grid 2	7812	21.3	7.8	51177	7.07	0.10	7812	6.86	0.11	21	282.22	40.67
Grid 3	8702	13.7	5.3	58004	6.34	0.07	8702	6.12	0.09	17	339.15	24.71
Track	32424	17.8	10.0	9933805	9.98	13.64	32424	6.69	0.30	170	306.95	45.52
All	57760	17.4	8.7	10078030	9.94	13.55	57760	6.62	0.30	228	308.02	44.27

Table 3.1: The count (n), mean ($\bar{x}$) and standard deviation (σ) of observations for snow depth (cm), the elevation of the snow and ice surfaces above the WGS84 ellipsoid (m) and the snow density (kgm^{-3})

For the tracks used in this study, the ASIRAS altimeter was flown in single-antenna SAR, low-altitude mode. Due to the nadir-facing orientation of the sensor, the footprint is pulse-doppler-limited, with an approximately rectangular shape, as shown in Figure 3.3. The footprint is estimated by taking a disk of radius r and cropping a slice of width Δx around the nadir, in the along-track direction. The radius of the pulse-limited footprint r is given by

$$r = \sqrt{h \cdot \frac{c}{B}} \tag{3.1}$$

where h is the sensor-to-surface range (300 m to 400 m), c is the speed of light within a vacuum and B is the bandwidth (1 GHz) (Scagliola, 2013). The width of the sharpened beam-limited footprint Δx is given by

$$\Delta x = h \frac{\lambda}{2 \cdot N \cdot v} PRF \tag{3.2}$$

where λ is the center wavelength (2.221 cm), N is the number of sharpened beams in the Doppler domain (64), v is the ground-speed of the sensor (70 m/s) and PRF is the pulse repetition frequency (2.5 kHz) (Mavrocordatos et al., 2004; Scagliola, 2013). This results in

a footprint that is approximately 2 meters in the along-track and 20 meters in the across-track direction. The along-track footprint width is referred to as the "sampling resolution" (Hawley et al., 2006), and corresponds to the spacing between nadirs of the radar altimeter returns, forming a continuous track of observations along the flight path.

Measurement of the surface such as snow depth, surface elevation and ice deformity classification are aggregated to this footprint for each return to estimate the surface characteristics being observed by the radar altimeter. To evaluate whether this footprint is the best method for aggregating measurements, circular areas of radii ranging from 8 to 4 meters are also used as aggregation footprints.

An additional parameter called h_{topo} is calculated as the difference between the 95th and 5th percentile of snow surface elevations within the footprint. Newman et al. (2014) used h_{topo} as a proxy for the ice surface roughness to filter out radar observations in areas of high topographic variability where the radar altimetry-derived snow depths tended to underestimate those observed *in situ*.

Due to the positioning and structure of the sensor platform during flight, the ALS and ASIRAS sensors have a relative elevation offset that needs to be calibrated against a common surface. The offset is applied to the ASIRAS radar return windows to align them with the ALS observations. In the case of CryoVEx, the offset is calculated over runways (Hvidegaard et al., 2014), using corner reflectors (Willatt et al., 2011), and over open water (Jennifer King et al., 2018). Although none of these options were available on the same day as the flights over the Eureka study area, data over runways were available for two flights: March 23rd at Sachs Harbour and March 26th at Canadian Forces Station (CFS) Alert. For each flight, the difference between the elevation retracked from the radar altimeter was compared to the average elevation of ALS measurements within the radar altimeter footprint to estimate the sensor offset. Returns were filtered to use only those with a pitch and roll deviation of less than 1.5° and whose footprints were within the runway boundary specified in the campaign documentation. The calibrations based on the March 23rd, and March 26th runway data are henceforth referred to as the R23 and R26 calibrations respectively.

Another option for calibrating the offset is to use the distance between the estimated

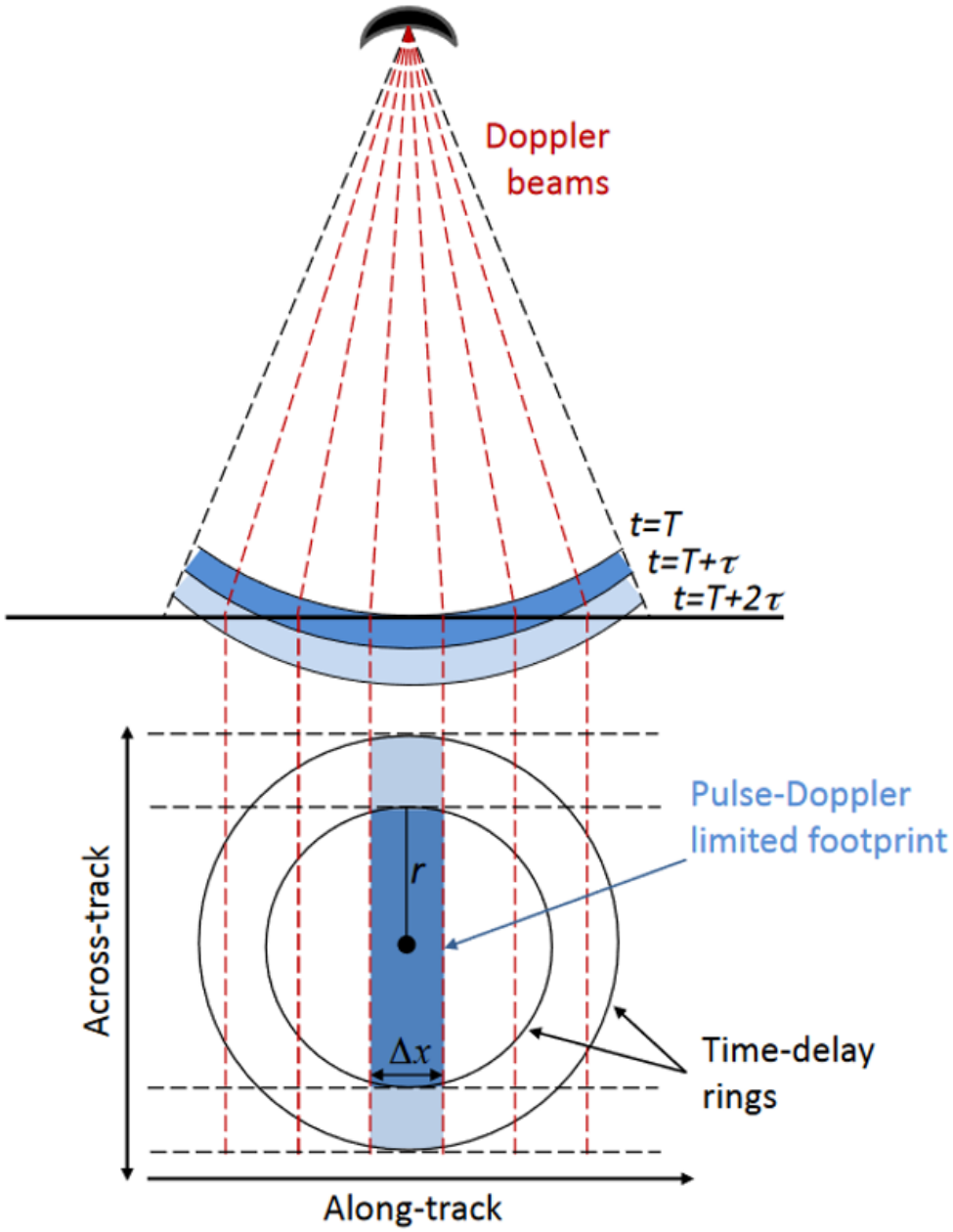

Figure 3.3: A side and top view of the pulse-doppler-limited sensor beam geometry. The footprint observed by each return is marked in dark blue. (Scagliola, 2013)

and observed snow-ice interfaces in returns over an area of shallow snow, flat ice and good coverage of snow depth observations. The Grid 3 zone was selected based on its absence of deformed ice, shallowest snow cover and lowest variability in snow and ice surface elevations (Table 3.1). Records meeting these criteria were selected and the difference between their estimated and observed snow-ice interface elevation were used to establish a shallow-snow offset. To reduce the effect of snowpack volume scattering on the radar waveform, only returns with an average observed snow depth of less than 10 cm were considered. This method will be referred to as the Shallow Snow in Grid 3 (SS3) calibration method.

An offset is calculated for each retracker threshold and applied to the retracked elevation to align it with the ALS surface observations, consistent with the methods of prior literature (Ricker et al., 2014; Hvidegaard et al., 2014; Jennifer King et al., 2018). Figure 3.4 shows how the distribution and variability of the offset observations vary change with the retracker threshold for each calibration method.

To evaluate the ability of the Ku-band radar altimeter to measure the elevation of the snow-ice interface, the penetration of radar signal and the accuracy of the interface estimate are calculated. Given a snow surface (snow-air interface) elevation of s_{as} and the retracked elevation s_r, the penetration distance of the radar signal into the snowpack is given by

$$P = s_{as} - s_r \tag{3.3}$$

The penetration can also be expressed relative to the observed snow dept h_s, which yields the proportion of the snowpack penetrated

$$P_r = \frac{P}{h_s} \tag{3.4}$$

Determining how well the retracked elevation measures the ice surface requires knowledge of the ice surface elevation (snow-ice interface), which is calculated as

$$s_{si} = s_{as} - h_s \tag{3.5}$$

The distance between the retracked elevation s_r and the observed ice surface elevation s_{si} is the error of the snow-ice interface estimate given by

$$E = s_r - s_{si} \tag{3.6}$$

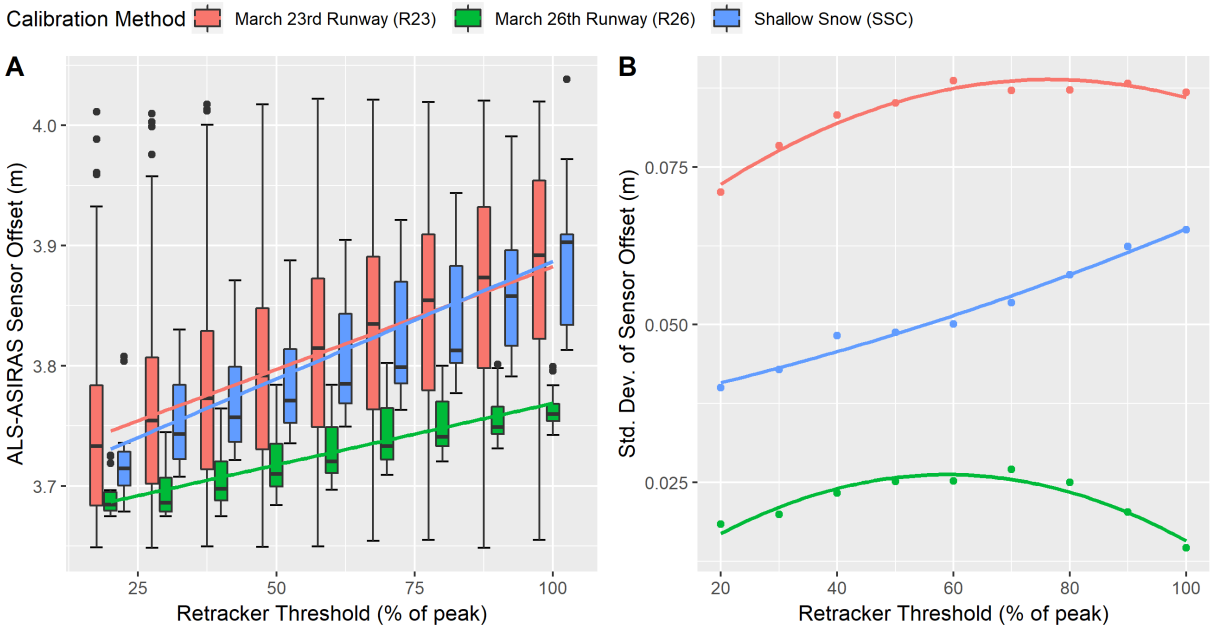

Figure 3.4: A) Boxplots of each method's sensor offset distribution at each retracker threshold. Comparison of the sensor offsets calibrated using returns with shallow snow against those calibrated using returns over runways on other dates. Linear fits are applied for each method to visualize the general slope of the offset-threshold relationship. B) Standard deviation of the offset for each calibration method, across the retracker threshold with a 2nd degree polynomial fit applied.

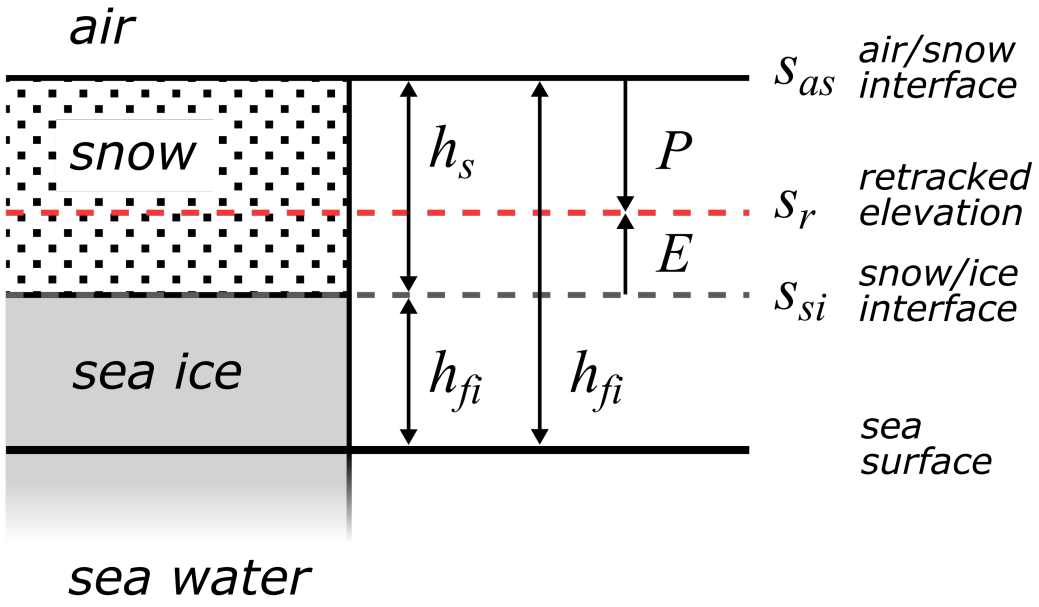

Figure 3.5: Schematic of a simplified snow on sea ice model showing the physical representation of variables used to calculate the penetration and error.

Grouped over a number of observations, the estimate of error E can provide an indicator of the bias in the estimate of the snow-ice interface. To measure the magnitude of the retracked elevation's deviation from the snow-ice interface elevation s_{si}, the absolute error can be calculated as

$$E_a = |E| \tag{3.7}$$

It can also be useful to measure the absolute error E_a relative to the snow depth to see how the error responds to characteristics other than the snowpack thickness over a track with varying snow depths.

$$E_{ra} = \frac{E_a}{h_s} \tag{3.8}$$

3.3 Analysis

When evaluating the accuracy of the estimate, it is necessary to investigate the effect of parameter selection on the estimate outcome. The calculation of the estimated snow-ice interface elevation s_r is dependent on footprint size, the retracker threshold and whether an adjustment for snowpack density is applied. To develop an accurate picture of the effect of the parameters on the estimate, the effect of variations in the snowpack and ice surface roughness must be reduced by evaluating the relationship over a region which does not have deformed ice. The region should also contain a dense grid of observations covering both the along-track and across-track directions. One such region is the gridded zone labeled number 3 in the 2014 Eureka campaign data. The effect of parameters on the accuracy of the estimate is quantified by comparing the error for radar returns within the grid 3 zone, and using offsets from each of the three calibration methods: March 23rd runway (R23), March 26th runway (R26) and using shallow snow (SS3).

3.3.1 Observation Aggregation Footprint

In Figure 3.6, the estimated penetration is compared for both the radar footprint (calculated from equations 3.1 and 3.2) and a circular footprint with a radius of 8 m, which is used in a study of ASIRAS over snow-covered sea ice by Jennifer King et al., 2018. The 8 m footprint has a slightly lower mean estimated penetration P_r, and a lower penetration variability when compared to the radar footprint. An extended v of this pattern is seen in Figure 3.7, where the mean and standard deviation of E_{ra} and P_r are plotted for footprint of radii between 8 and 40 meters. Both of the errors' mean and standard deviation have minima between 15 and 20 meters, with decrease of 5 to 10 percentage points from the 8-meter radius to the minimum. The M26 calibration shows a decrease twice that of the other calibrations, and the radius at the minimum value of the standard deviations of both errors is slightly larger than the other calibrations.

Since E_{ra} is the magnitude of deviation in P_r from 100 %, a decrease in P_r away from a 100 % penetration should result in an increase of E_{ra}. The decrease of the mean and standard deviation of E_{ra} and P_r towards the 15 to 20 meter range in Figure 3.7 indicates

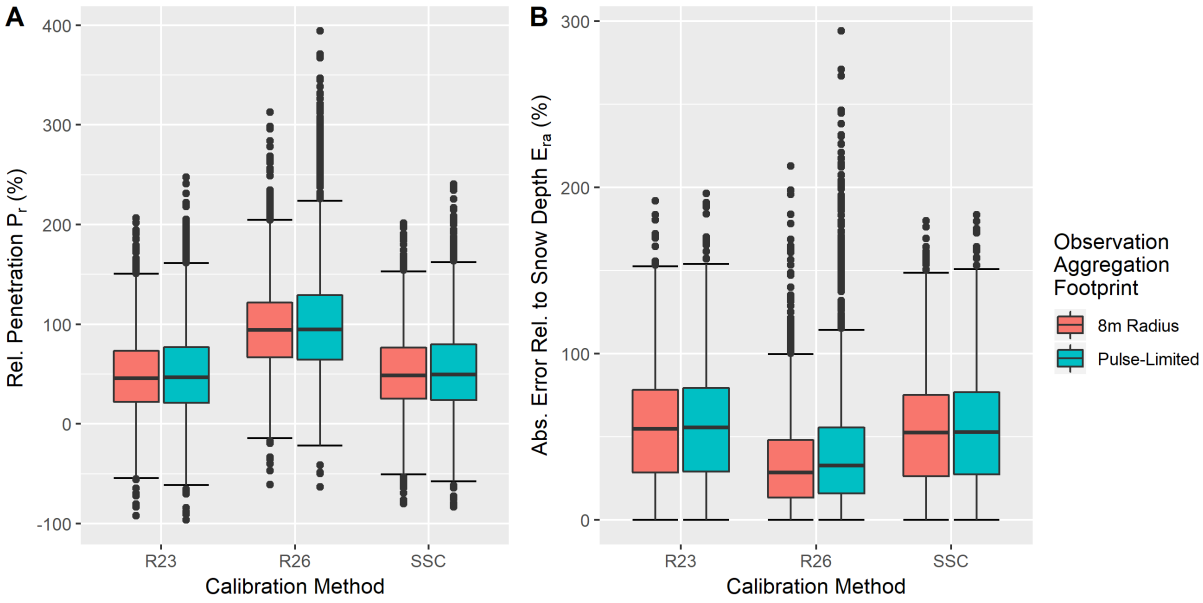

Figure 3.6: Boxplots showing the distribution of P (A) and E_{ra} (B) for the pulse-doppler-limited footprint and a circular footprint with an 8-meter radius, grouped into the three offset calibration methods.

that aggregating surface measurements to a circular footprint of 15 to 20 meters may provide a better estimate of the surface characteristics observed by the ASIRAS radar altimeter.

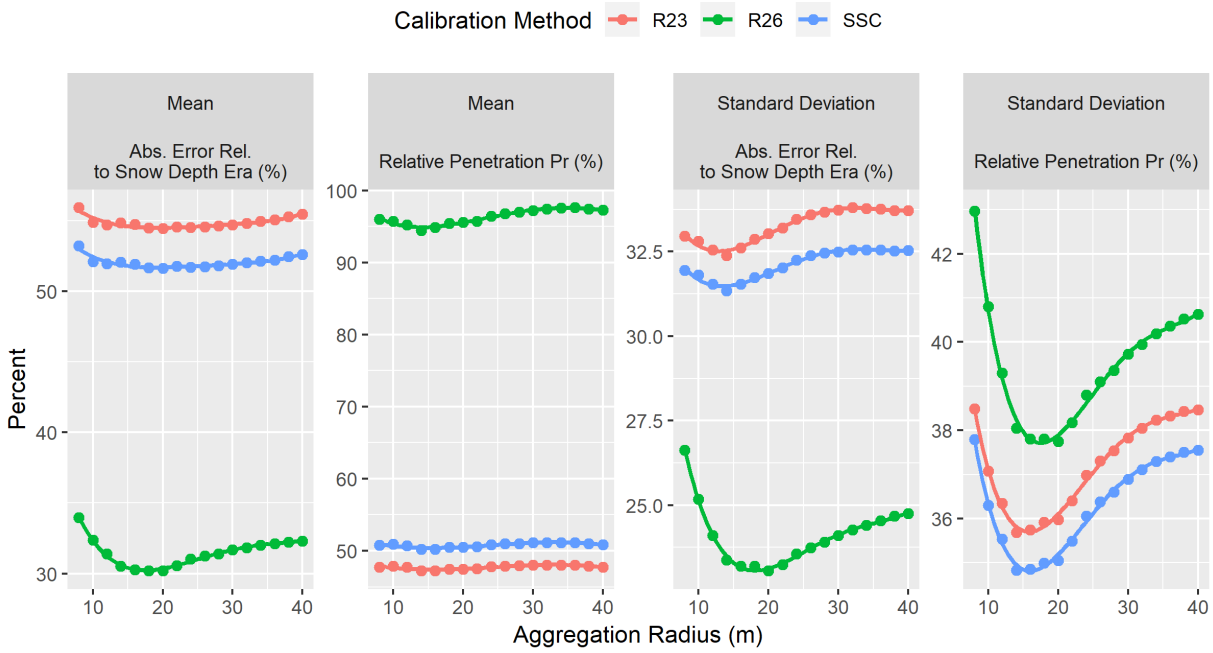

Figure 3.7: Mean and standard deviation of P_r and E_{ra} for circular footprints of 2 to 40 meters at 2-meter increments, fitted with 4th degree polynomial curves.

3.3.2 Propagation Bias due to Snow Density Correction

When a microwave signal passes through the snowpack, its speed is reduced relative to the propagation of EM in a vacuum such that

$$c_{snow} = \frac{c}{\sqrt{1 + 2p_s}} \tag{3.9}$$

where p_s is the density of the snow in g/cm^3 (Kurtz et al., 2013). This introduces a propagation bias into the ice surface elevation estimate, causing an underestimate of the snow depth and an overestimate of the radar freeboard (Mallett et al., 2019). Figure 3.8 shows the effect of applying this correction on the error and penetration. The estimated ice surface elevation is shifted upwards closer to the snow surface, and increases the E_{ra} for the R23 and SS3 calibrations as it moves the mean penetration further from 100 %. Since not applying the correction results in a large part of the returns appearing below the ice surface and a larger variability in the penetration, the adjustment will be applied in further analyses.

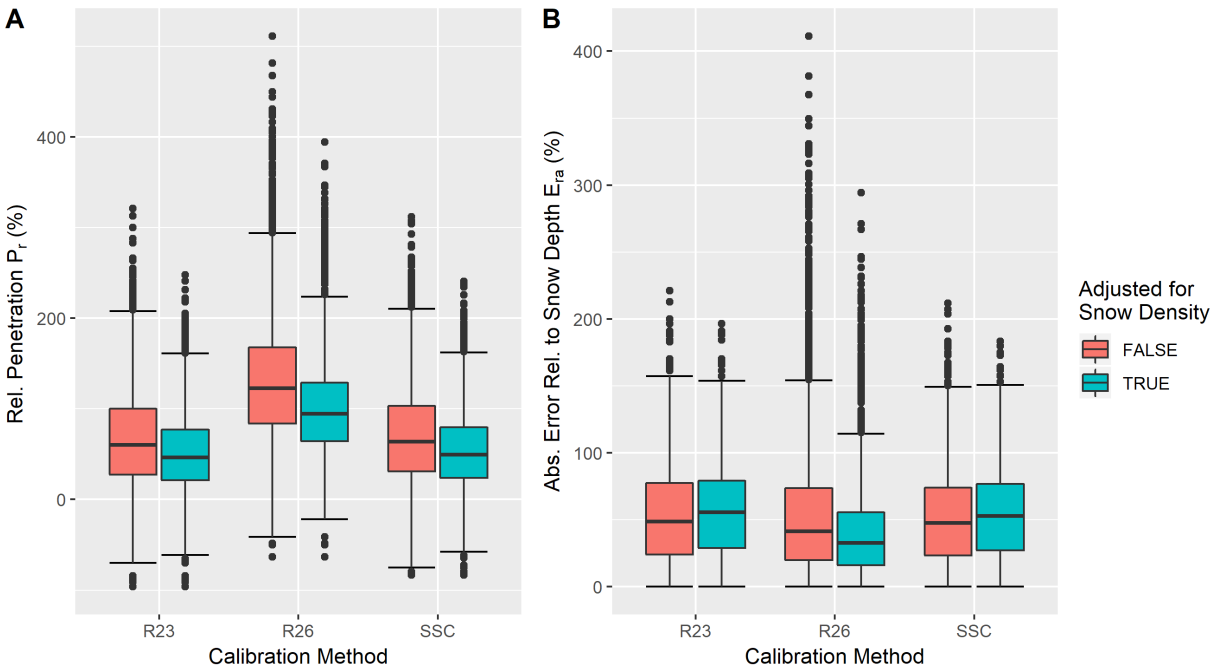

Figure 3.8: Boxplots showing the distribution of P_r (A) and E_{ra} (B) with the adjustment for snow density applied and not applied. Grouped into the three offset calibration methods.

3.3.3 Retracker Threshold Selection

The effect of retracker threshold selection on the accuracy of the ice surface estimate was visualized by plotting boxplots of the estimated relative penetration P_r across the selected threshold for each calibration method in Figure 3.9. Since the change in variability is difficult to see on the boxplots, the standard deviation is plotted alongside them. The relative penetration increases with the retracker threshold, and the standard deviation of the penetration has a minimum at the 40 % to 60 % threshold for all calibration methods. The R26 calibration method has a lower standard deviation but a higher penetration, which crosses the 100 % mark at the 60 % threshold.

When selecting a calibration method for the sensor offset, the SS3 calibration is preferred over the two runway calibrations. The R23 runway ALS measurements were flagged as poor quality, while the R26 calibration resulted in a mean penetration was too close to 100 %, with approximately half of the snow-ice interfaces estimated to be below their observed elevation. The estimated interface may appear below the observed interface in cases where snow-depth measurements are too sparse or far from the nadir, and do not represent the snow depth observed by the radar altimeter (Willatt et al., 2011). This can indicate that the sensor offset values in the R26 calibration are too low, since the analysis was performed over an area with a high density of snow depth measurements, and the ASIRAS dominant scattering interface is usually within the snowpack (Kern et al., 2015; Jennifer King et al., 2018; Ricker et al., 2014).

Ricker et al. (2014) highlighted the need for an improved understanding of how changes in the snowpack and ice surface affect the selection of a threshold that will give the closest estimate of the snow-ice interface. To cover a wider surface variability, including deformed ice surfaces, the analysis is expanded to returns across the entire track. To better represent surface variability, a 16 meter footprint is used, and the analysis is limited returns that have more than 10 snow depth observations within the footprint. Figures 3.10 and 3.11 show how the percent of retracked elevations s_r above, below and within the snowpack changes with the threshold. Since a larger threshold will select a location the echo deeper into the snowpack, the proportion of s_r above the snowpack will decrease and below the snowpack will increase in response to the threshold. For most variables, the 60% threshold yields

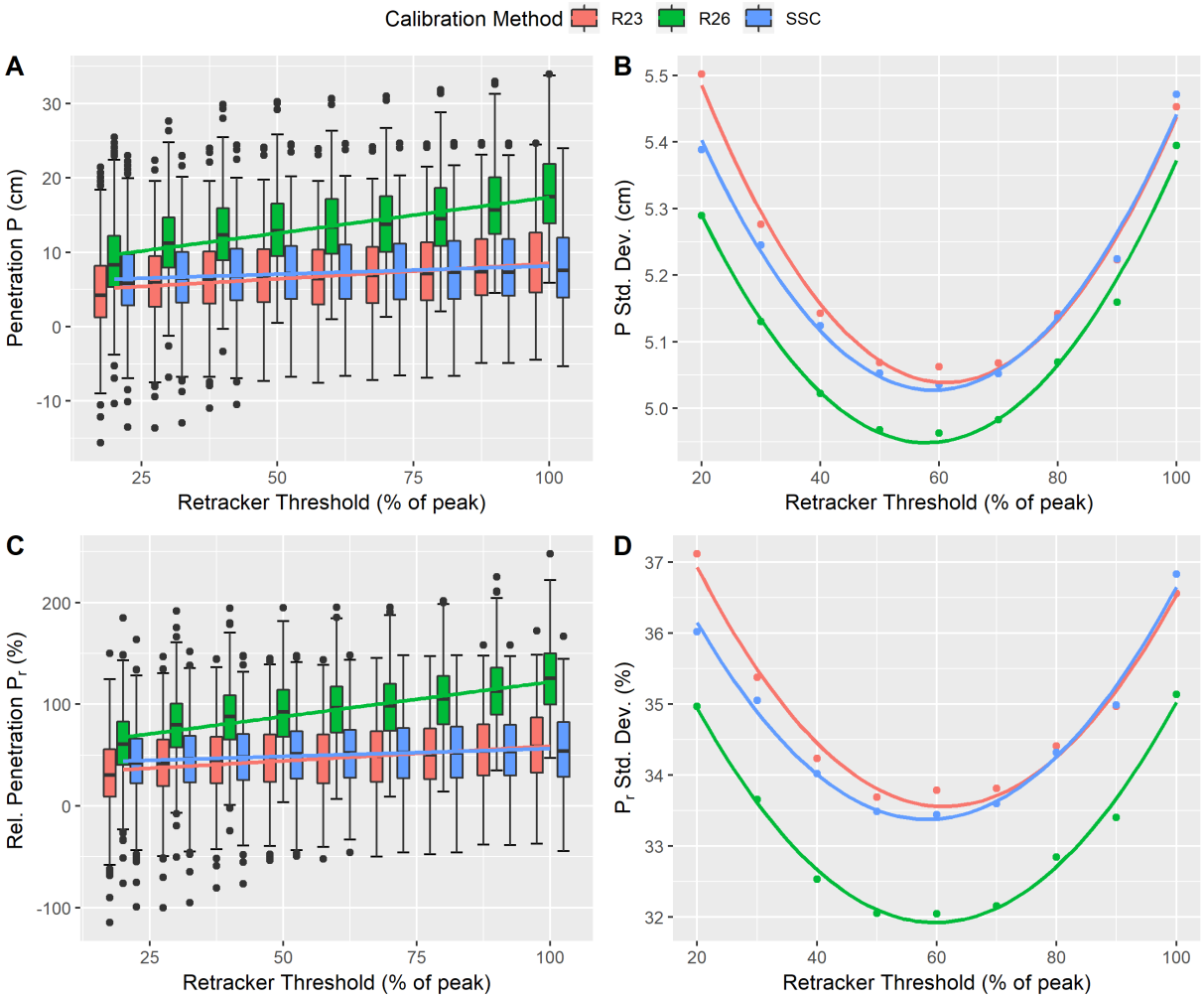

Figure 3.9: Boxplots showing the distribution of the penetration P (A) and relative penetration P_r (C) for each calibration method, across the retracker threshold. A linear fit is applied to show the difference in slope between the calibrations. Standard deviations of the penetration P (B) and relative penetration P_r (D) for each calibration method, across the retracker threshold. A 2nd degree polynomial fit is applied.

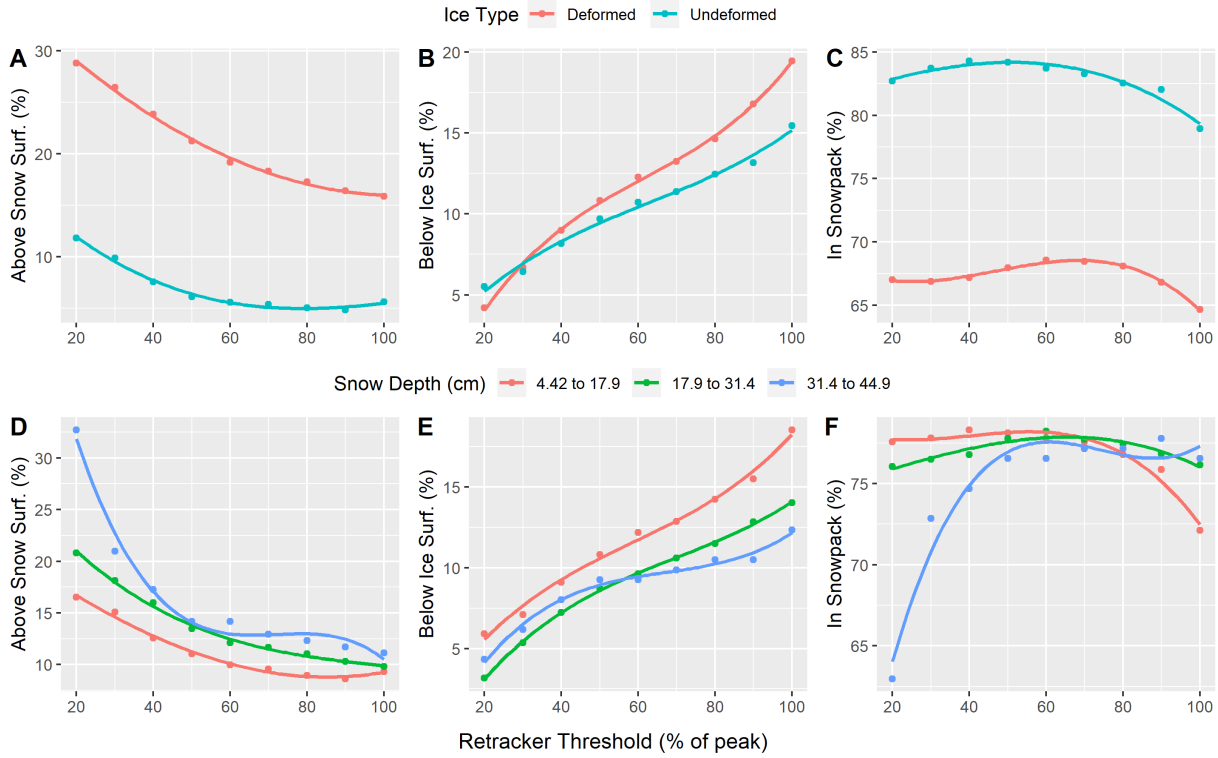

Figure 3.10: Proportion of retracked scattering surfaces (s_r) located above the snowpack, below the ice surface and within the snowpack. Proportions are shown across retracker threshold selections for evenly stratified categories of surface characteristics A-C) ice deformed classification D-F) snow depth

the highest proportion of s_r within the snowpack. The deformed ice classification (Figure 3.10c) is an exception, where deformed ice has a higher ideal threshold than undeformed ice. Figures 3.10c and 3.11c,f,i show that even at an ideal threshold, a deformed ice surface, absence of salinity and a small grain size or ratio will result in a lower proportion of s_r falling within the snowpack.

A similar analysis can be applied to the measures P and P_r to investigate how threshold selection affects the penetration, and if there exists an ideal threshold that would achieve 100% penetration P_r through the snowpack. Figures 3.12 and 3.13 show that the penetration distance P generally increases with threshold, but its rate varies depending on

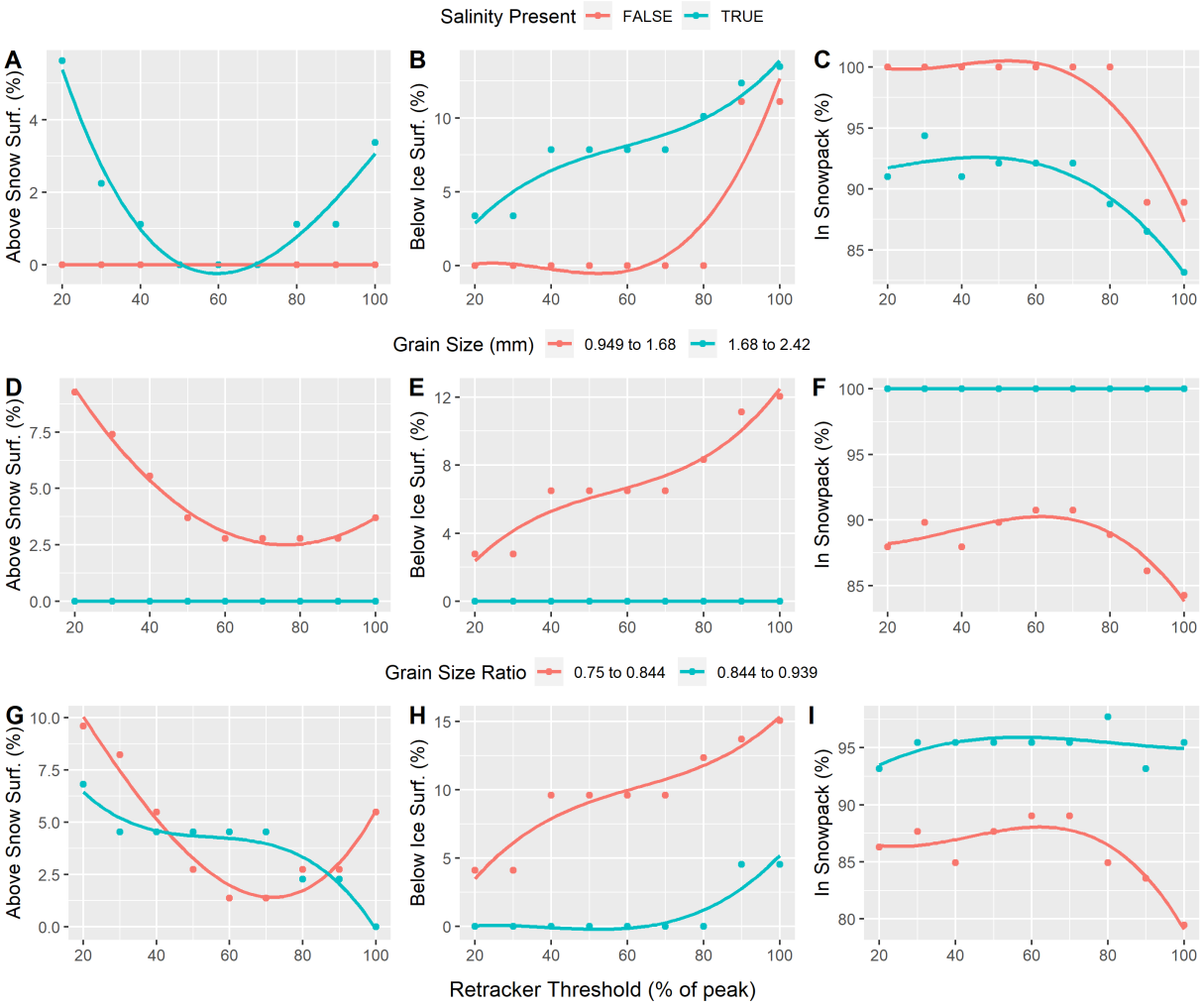

Figure 3.11: Proportion of retracked scattering surfaces (s_r) located above the snowpack, below the ice surface and within the snowpack. Proportions are shown across retracker threshold selections for evenly stratified categories of snow pit characteristics A-C) presence of salinity in the snowpack D-F) average snow grain size G-I) snow grain size ratio (between smallest and largest diameter of selected grains)

the snowpack and ice surface properties. Figure 3.12e suggests that the penetration is greater in deeper snow, but this is likely due to the penetration-limiting bias introduced by shallow snow. When the snow depth is accounted for in Figure 3.10f, the penetration and its rate of change with threshold appears to be the same across varying snow depths. The opposite effect is observed in Figures 3.12a and b, where the penetration P for both deformed and undeformed ice appears to be similar, but when accounting for snow depth, a larger percentage of the snowpack is penetrated over undeformed ice, likely because the snow is deeper over rougher ice. Deformed ice also displays a higher variability in both P and P_r (Figures 3.12c and d). An increased penetration distance and slope with respect to threshold are also observed for a snowpack without salinity, a smaller grain size and/or a lower grain size ratio.

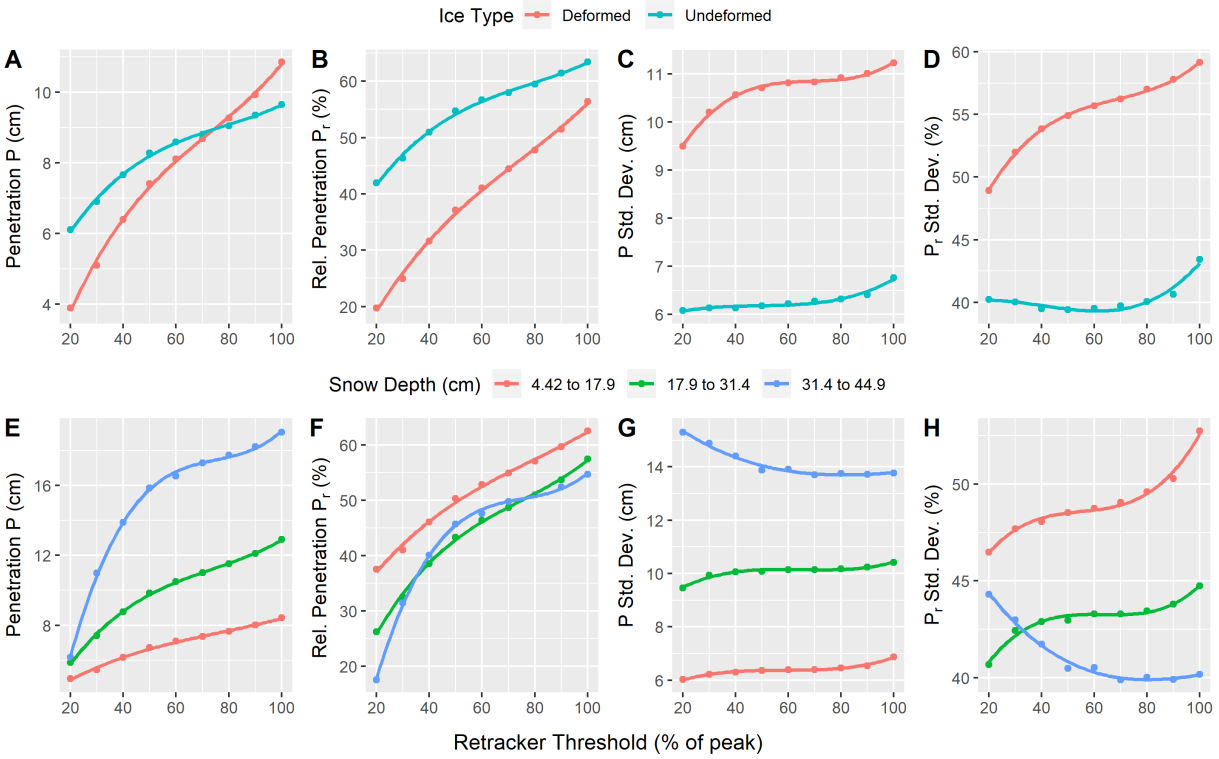

Figure 3.12: Mean and standard deviation of the estimated penetration P and penetration relative to the snowpack depth P_r across retracker threshold selections for evenly stratified categories of surface characteristics A-D) ice deformed classification D-F) snow depth

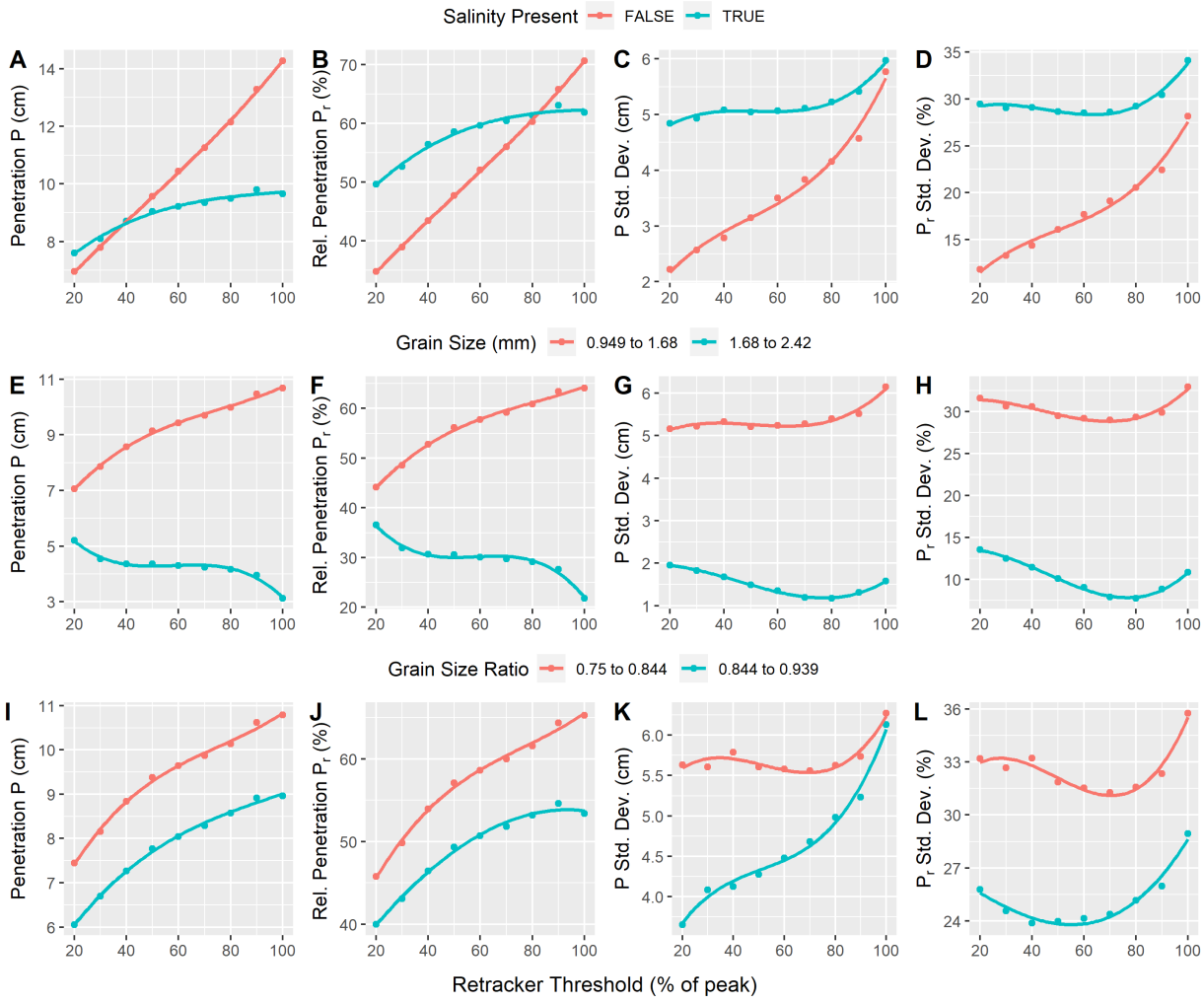

Figure 3.13: Mean and standard deviation of the estimated penetration P and penetration relative to the snowpack depth P_r across retracker threshold selections for evenly stratified categories of snow pit characteristics A-C) presence of salinity in the snowpack D-F) average snow grain size G-I) snow grain size ratio (between smallest and largest diameter of selected grains)

3.3.4 Cross-Correlation Between Surface, Sensor and Error Variables

The penetration and snow-ice interface estimate error can also be compared to observations of surface and sensor characteristics to investigate their relationships, and if they can be used to better understand and improve the error. A correlation matrix of the surface characteristics, waveform shape and estimate errors is calculated using the Kendall rank correlation coefficient. For the retracked elevation s_r used to calculate the error and penetration, a 60% retracker threshold was selected due it yielding the highest proportion of s_r within the snowpack (Figures 3.10 and 3.11).

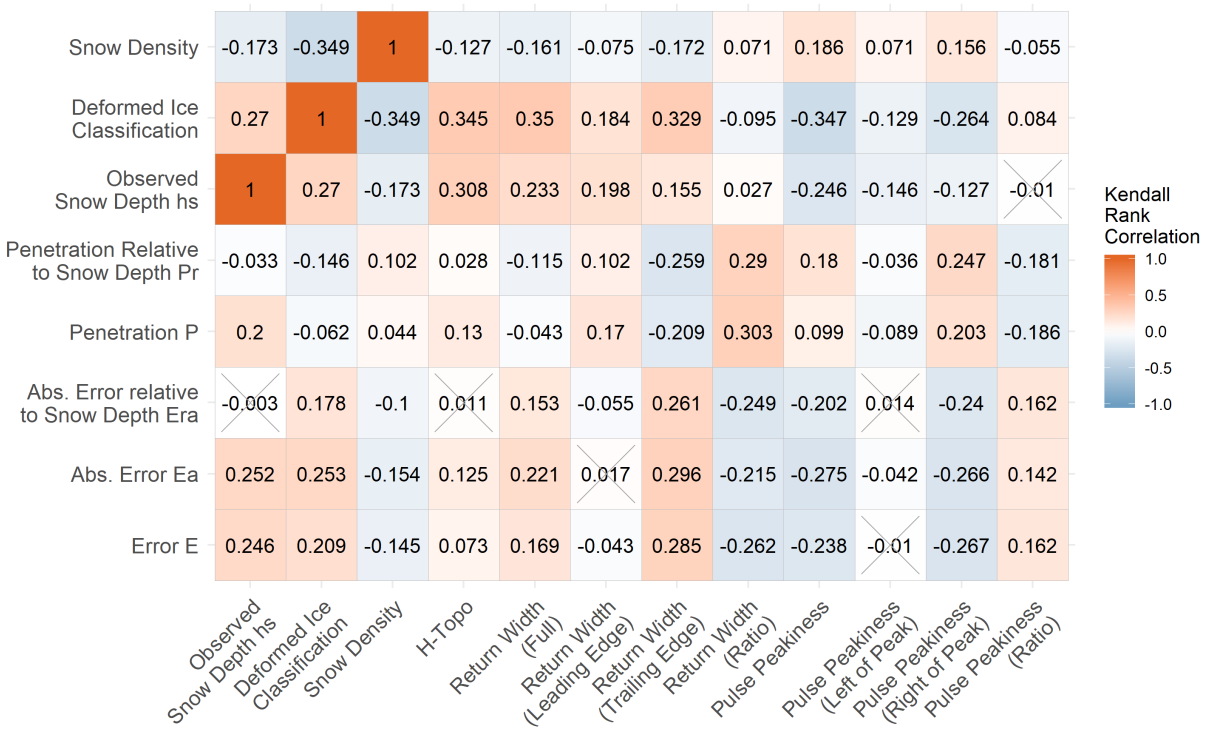

Figure 3.14: Correlation matrix of snow-ice surface estimate error measures, observed surface characteristics and measures of the echo waveform shape. Non-significant correlations are crossed out.

3.3.5 Effect of Variables on Waveform Shape

The presence of statistically significant correlations between measures of the waveform shape (PP and RW) and surface characteristics (Figure 3.14) suggests that there may be visible patterns in the shape of the waveform that change based on the properties of the observed surface. To visualize these patterns, the returns were split into equally sized groups based on their measurement value of the surface and shape characteristics analyzed in the correlation matrix. The waveforms of these groups were then aligned based on the bin of the first peak return value, and then averaged within the group to produce Figure 3.15.

Since the emitted power of the radar altimeter is a constant 5W, the plots show how different surface properties can affect the strength of the return. The scale contrast between groups can also obscure the bias that a change in characteristic value can have on the leading or trailing edge of the waveform. To observe this aspect, the same waveforms are normalized by scaling the maximum return power to 1, as shown in Figure 3.16. The surface and depth of the snowpack may be affected by the topology of the ice surface, so the waveforms are additionally grouped over the ice deformed class to isolate better isolate the effects of the snowpack characteristics 3.17.

A correlation matrix comparing the summary of snow pit measurements to ice surface estimate error (Figure 3.18) was calculated using the Kendall rank coefficient, with grain size ratio being the only variable to show a significant correlation. A similar correlations matrix of snow pit variables with the measures of waveform shape was also calculated (Figure 3.19), and a waveform visualization was produced for the variables that showed significant correlations (Figures 3.20 and 3.21).

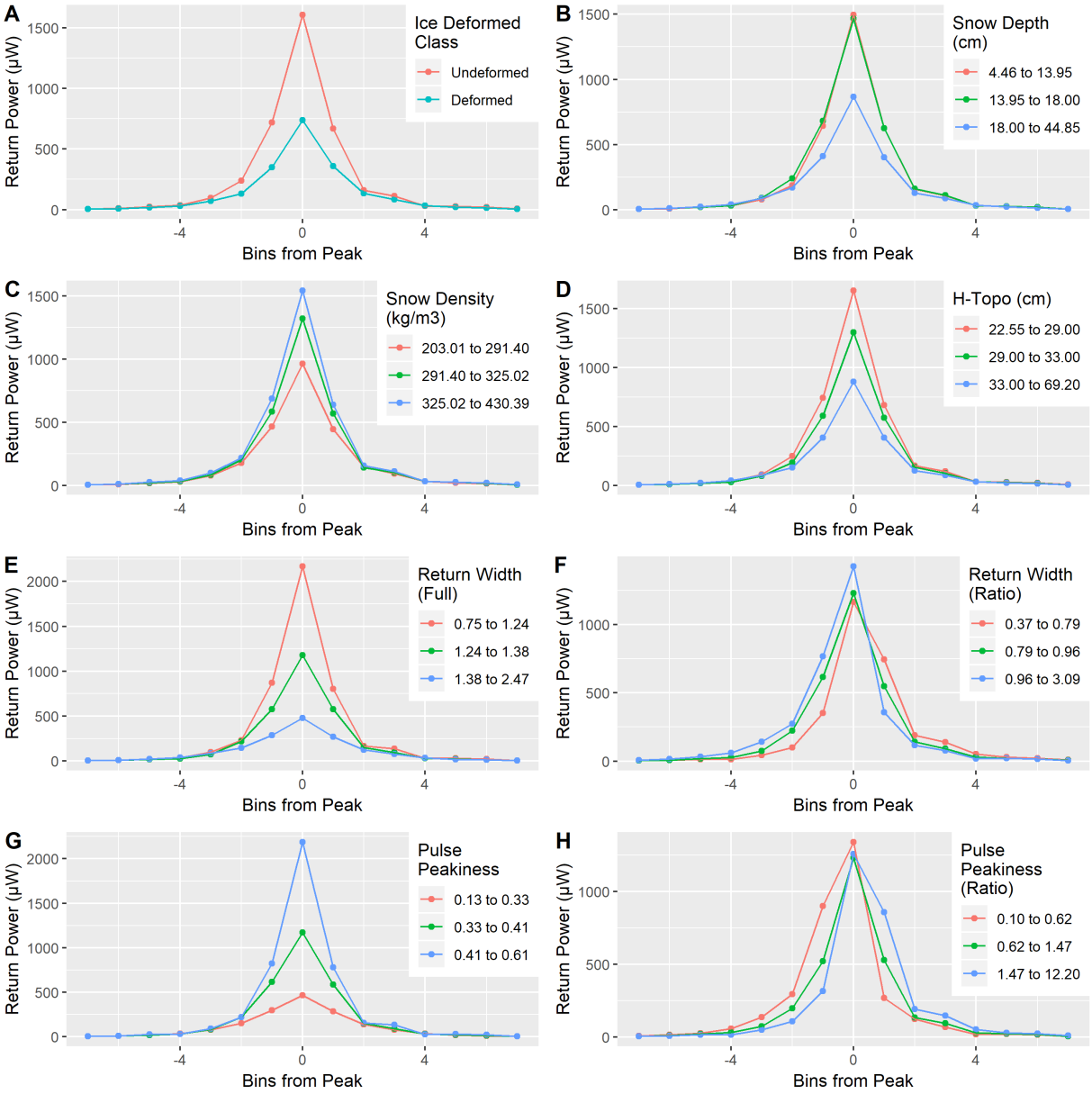

Figure 3.15: Average echoes aligned by their peaks and grouped by surface and waveform shape characteristics.

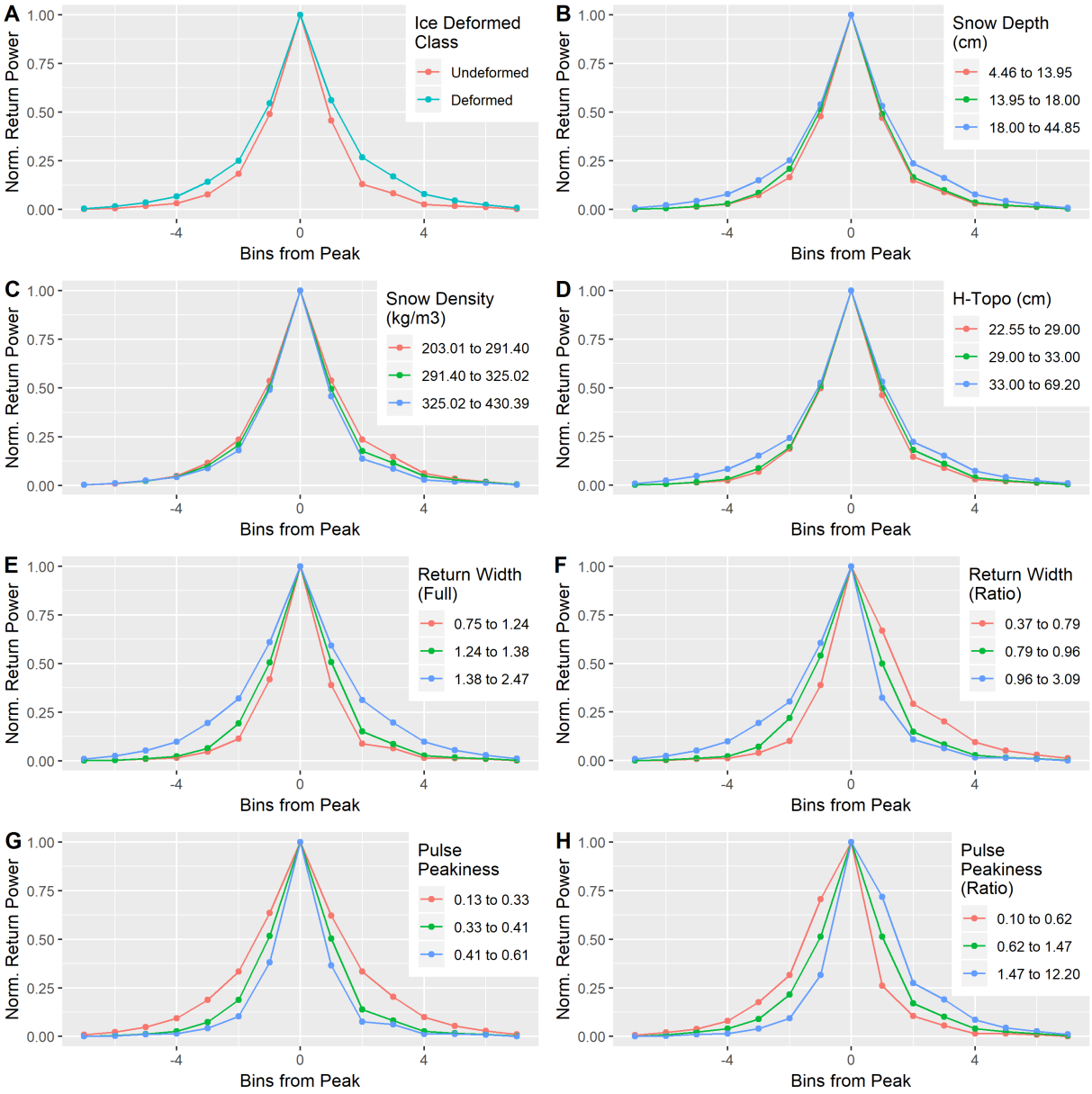

Figure 3.16: Average echoes aligned by their peaks and grouped by surface and waveform shape characteristics. The return power is normalized across all echoes so the difference in shape between groups can be visualized.

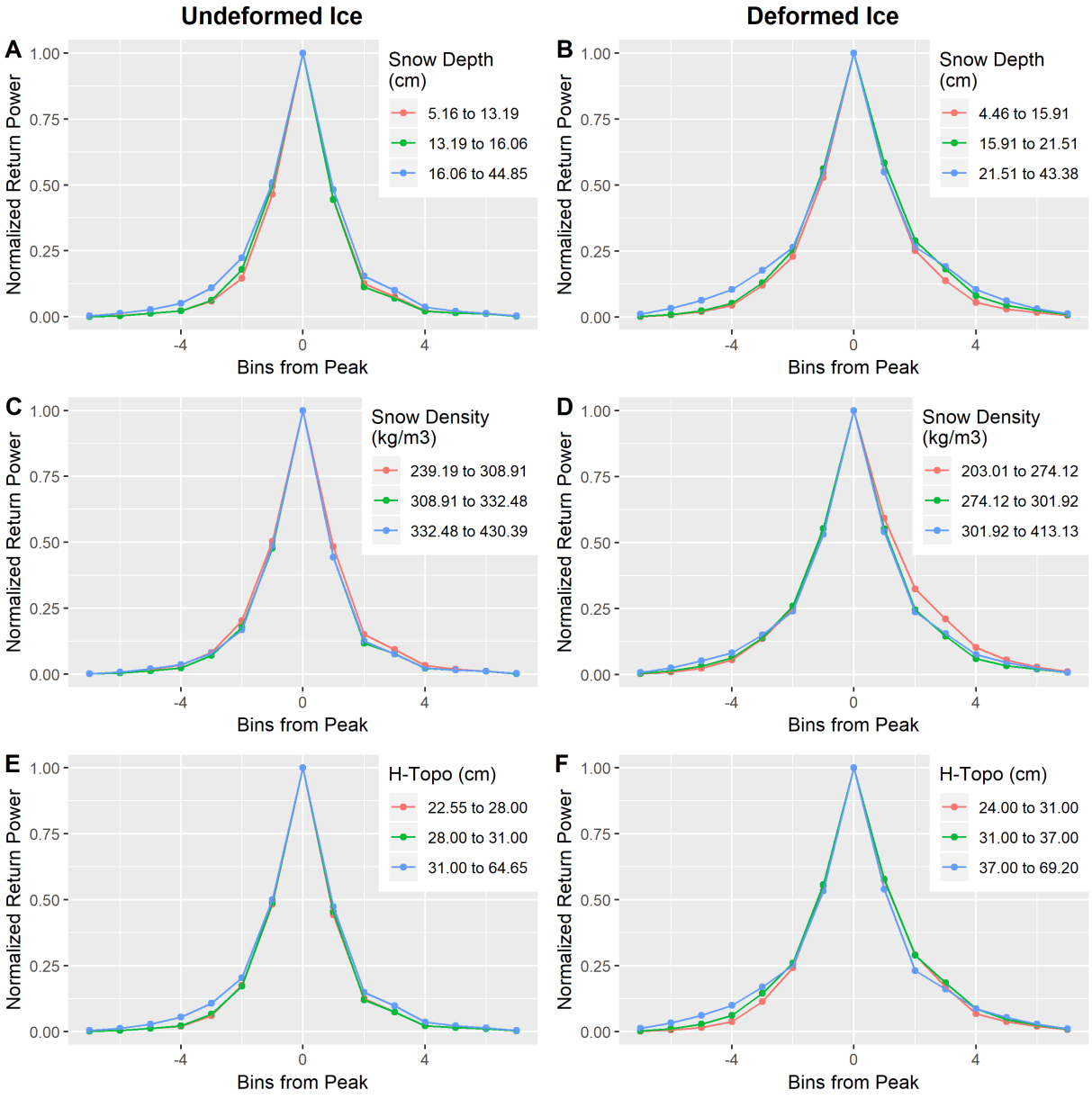

Figure 3.17: Average echoes aligned by their peaks and grouped by surface and waveform shape characteristics. The waveforms are also grouped by the ice deformed class where the left column (A, C, E) is for returns over undeformed ice and the right columns (B, D, F) is over deformed ice. The return power is normalized across all echoes so the difference in shape between groups can be visualized.

Figure 3.18: Correlation matrix of ice surface estimate error variables with snowpack characteristics measured in snow pits located within 10 meters of an ASIRAS nadir. Non-significant correlations are crossed out.

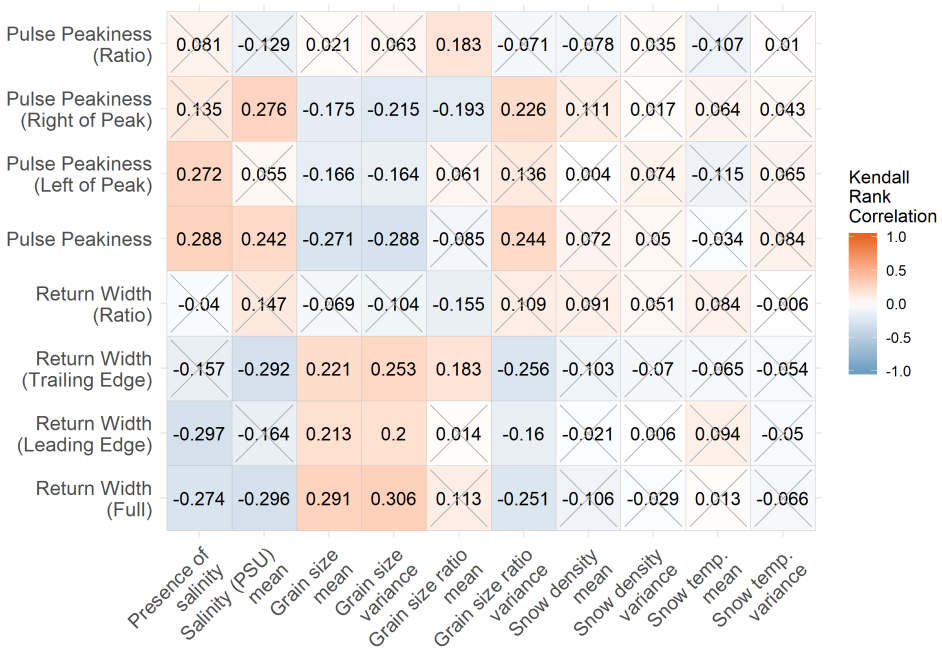

Figure 3.19: Correlation matrix of waveform shape measures with snowpack characteristics measured in snow pits located within 10 meters of an ASIRAS nadir. Non-significant correlations are crossed out.

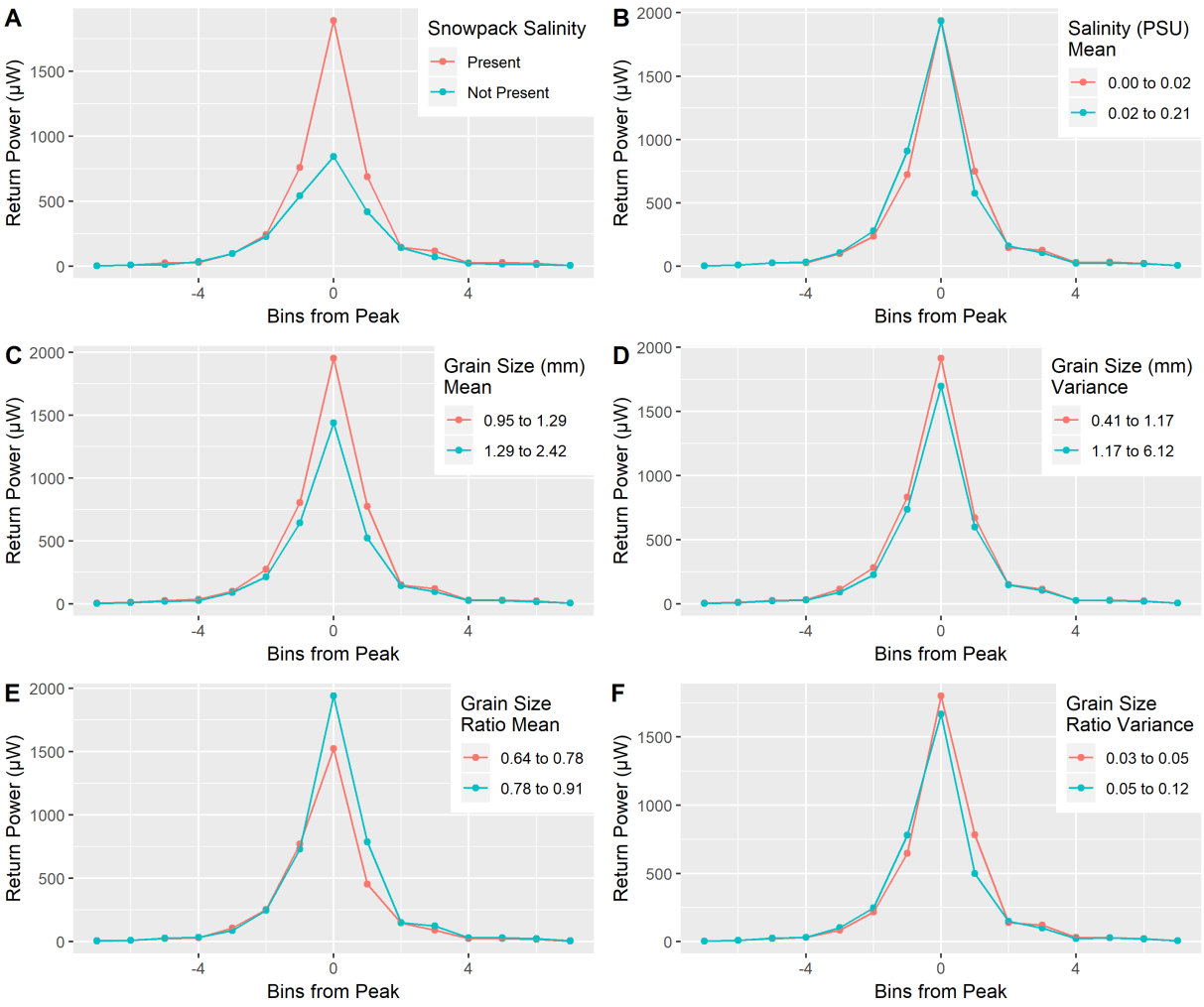

Figure 3.20: Average echoes aligned by their peaks and grouped by pit snowpack properties.

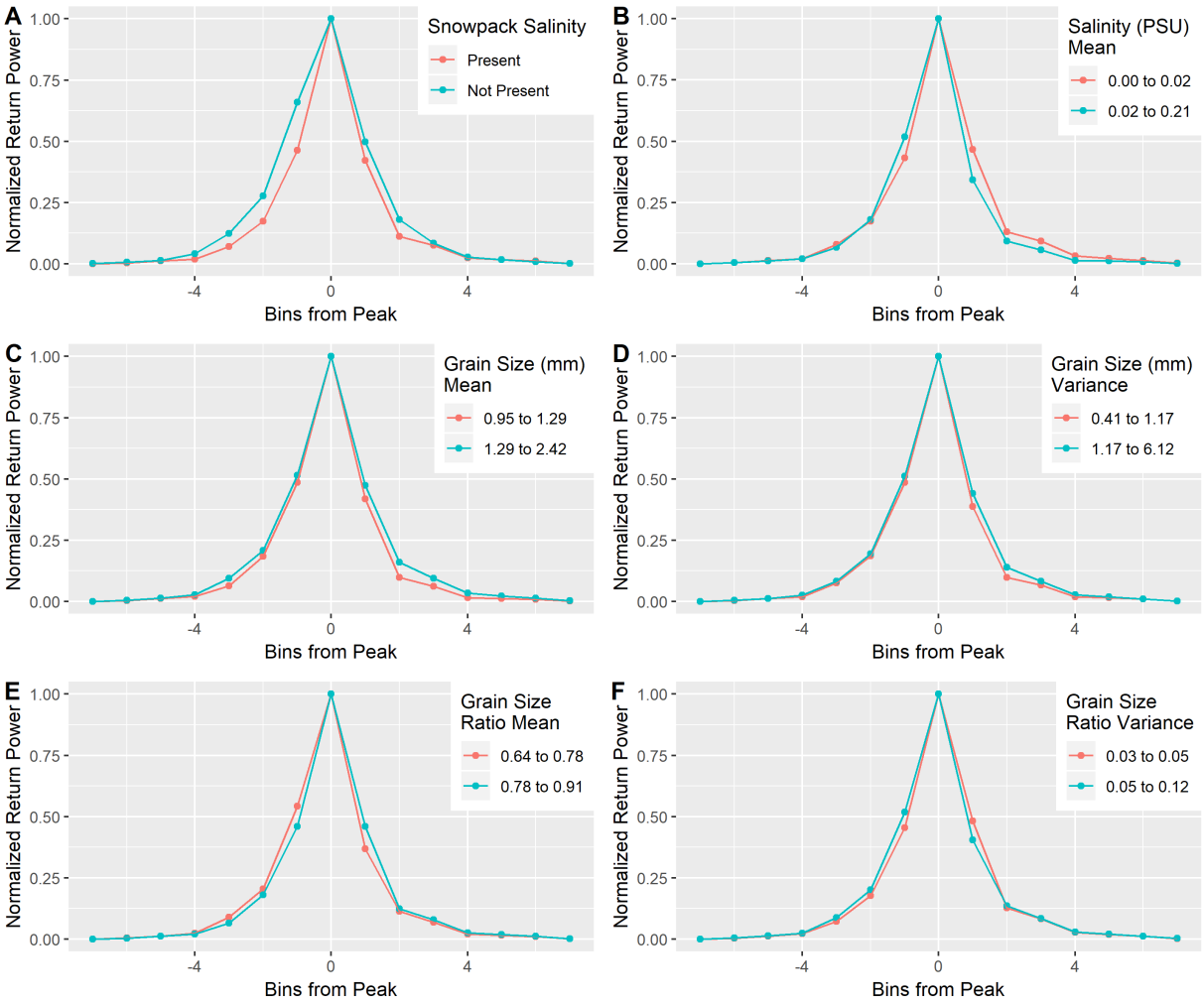

Figure 3.21: Average echoes aligned by their peaks and grouped by pit snowpack properties. The return power is normalized across all echoes so the difference in shape between groups can be visualized.

3.4 Discussion

Establishing the sensor offset in this study suffers from issues that prevent an accurate location of the ASIRAS retracked elevation relative to the snow surface observed by the ALS. One problem is that there are no non-snow-covered flat surface in the study area from which both the high frequency ALS and lower frequency ASIRAS will reflect at close to the same elevation. The CryoVEx campaign had 3 sites at which runway calibrations were performed, but the suggested offsets collected from these tracks varied by as much as 10 cm, suggesting that they could not be reused in other tracks. The SS3 offset calibration method described in section 3.2 attempts to locally estimate the sensor offset, but its accuracy is complicated by the presence of a thin (10 cm) snow cover. Figures 3.6 to 3.9 show that while the estimated penetration and error using SS3 differed from R23 and R26, the shape of their response to changes in parameters (such as footprint size and retracker threshold) were very similar. This would suggest that SS3 is a valid method for making inferences about the relationship between the retracked radar elevations and characteristics of the surface.

Another challenge with the sensor offset is its variability. Even across the short tracks used to calibrate the offset, its standard deviation ranges from 2 cm to 8 cm (Figure 3.4). In the CryoVEx campaign report, the highest quality offset calibration (April 28th at Akureyri, Iceland) shows a similar standard deviation of 7 cm, although it uses the Offset Center of Gravity (OCOG) retracker (Hvidegaard et al., 2014). A comprehensive explanation for the source of the offset was not found in the CryoVEx campaign report or literature that discussed methods for calibration (Willatt et al., 2011; Jennifer King et al., 2018). It is not clear whether the variability of the offset is caused by observing an imperfectly smooth surface, or by noise within the instrument setup.

Considering the uncertainties surrounding the sensor offset, it is unlikely that the estimate of the retracked elevation s_r is representative of its actual elevation or position relative to the snow surface observed by the ALS. Although this prevents an accurate interpretation of the penetration P and error E, their response to changes in model parameters and surface characteristics can provide insights into how the snow-ice interface estimate is affected by sea ice and its snow cover.

The radar altimeter footprint is an important component of this analysis because its extent dictates which ground observations are aggregated to obtain an estimate of surface properties. Applying formulas 3.1 and 3.2 to the parameters of the sensor in this study yields a pulse-doppler-limited footprint of 20 meters by 2 meters, which should represent the maximum extent viewed by the radar altimeter. The representation is only for an ideal flat surface, and since the ice surface observed in this study is not flat, has a snow cover and was formed in such a way that the elevation at certain points may be correlated to points some distance away, the area on the ground that could appear in the radar signal can be larger than the idealized footprint. This is shown in Figures 3.6 and 3.7, where increasing the footprint from a 20 by 2 meter rectangle to a circle with a radius of 15 to 20 meters decreases the mean and standard deviation of the error E_{ra} and penetration P_r. Since the mean penetration is less than 100 %, a decrease in its value would increase the deviation from the perfect value and increase the E_{ra}. Since E_{ra} also decreases towards the 15 to 20-meter radius, this indicates that a footprint of that size is improving the accuracy of the estimate.

This effect may be due to the roughness of the ice surface, where ice features that are elevated above the surface at the nadir can appear in the radar signal at distances proportional to their height (Newman et al., 2014). The pattern may also be a function of the spatial autocorrelation of the ice surface. By applying an exponential fit to a semi-variogram of the ice surface elevation, the autocorrelation range was determined to be approximately 6 meters. An ice surface measurement at the edge of the 5-meter cross-track footprint radius can be correlated to a point 6 meters away, potentially expanding the radius to 11 meters, which still does not extend to the 15 to 20-meter distance seen in Figure 3.7. Since the estimates of error E_{ra} and P_r incorporate the snow depth and snow surface elevation, measurements of those properties may affect the perceived footprint radius. Applying the same exponential fit to the snow depth and snow surface elevation measurements results in a spatial autocorrelation range of 15.88 and 14.32 meters respectively (Figure B.1). Spatial autocorrelations of 15 meters for the depth and surface topography of the snowpack could potentially extend the flat-surface (1 x 10 meters) footprint to correlate with surface characteristics of up to 20 meters from the nadir.

The offset-threshold relationship (Figure 3.4) for the R23 calibration and SS3 calibra-

tions are slightly positive, indicating that returns used for calibration likely had less surface interference from snow cover or ice roughness than the returns in the grid 3 zone, but more than over the R23 runway. This is expected for the SS3 calibration, which was done over ice covered by snow up to 10 cm deep, but not for the R23 runway, which was expected to be a flat surface with little to no snow cover. If its threshold-penetration slope approaches the shallow-snow calibration, then it is possible that the runway had a thin snow cover, or the geographical area used to limit observations to the runway included snow features.

The impact of retracker threshold selection on the penetration over the Grid 3 zone is shown in Figure 3.9, with the same patterns seen for all the calibration methods. For an ideal sensor offset that is constant across retracker thresholds, the penetration of the signal would be expected to increase with threshold. This effect should be accounted for by the per-threshold offset of calibration method (Figure 3.4), but all of the methods show an additional linear relationship between penetration and threshold (Figure 3.9). If the slope of the relationship is positive, it indicates that the slope of the threshold-offset relationship is too low, and that the signals of the calibration surface have a higher PP than the measured ice surface. This is the ideal case, since the calibration should be done over a flat runway and the ice surface may be rough. The penetration-threshold relationships in Figure 3.9 for both P (A,B) and P_r (C,D) are very similar, likely due to the correlation between penetration and snow depth described in section 3.3.4.

Ricker et al. (2014) highlighted the need for a better understanding of the relationship between retracker threshold and the snow-ice interface estimate, and how it is affected by changes in surface characteristics. Figures 3.12 and 3.13 show that the penetration not only increases with threshold, but the rate of increase is a function of ice surface and snowpack properties. The lack of a reliable sensor offset prevents a direct interpretation of the radar penetration distance as performed by Nandan et al. (2017b), but the penetration-threshold trends may provide insight into how the snow-ice interface estimate can be improved, if the trends are shown to hold true across different offsets. Figures 3.12 and 3.13 were calculated using the SS3 calibration, but the same analysis using the R23 and R26 calibrations is presented in the appendix sections A.1 and A.2 respectively.

Since the SS3 and R23 produce similar offset values, the results in section A.1 are very close to those of section 3.3.3, but with a consistently higher penetration of 1 cm to 2 cm

for the SS3 calibration. Using the R26 calibration (section A.2) shows completely different relationships between observed surface characteristics and the fraction of retracked elevations s_r within the snowpack, with no threshold consistently providing the best coverage like the 60% threshold in section 3.3.3. There is also no consistent pattern similar to that in Figures 3.9b and d, where a single threshold results in a lower variability in the penetration.

One consistent feature across all the calibrations is the relative change in the slope of the penetration-threshold curve among different categories of surface characteristics. All three calibrations show that the presence of deformed ice, deeper snow, the absence of snowpack salinity, and a higher grain size all cause the penetration to increase more rapidly with a larger threshold percentage, while a larger grain size ratio appears to have no effect on the relationship. The penetration-threshold curves also follow an inverse-sigmoid shape, supporting the idea that the leading edge can be approximated by a logistic or Gaussian function (Zygmuntowska et al., 2013).

Although a highest threshold selection results in a deeper estimated penetration, no threshold value provided an average 100% snowpack penetration P_r using the SS3 or R23 calibrations. The R26 calibration was able to reach a 100% penetration, but the ideal threshold used to reach that penetration varied depending on the surface characteristics value, and in some cases could not reach 100%. For example, in Figure A.7f, the ideal threshold is 60% for a snowpack with a depth between 4.42 cm to 17.9 cm and 95% for 17.9 cm to 31.4 cm, but no threshold can reach 100% penetration for deeper snow, which has a maximum penetration of 85%. A similar effect is seen in Figure A.8f, where a snowpack with a grain size of 1.68 mm to 2.42 mm has a maximum penetration of 90%.

The SS3 calibration likely produces an underestimate of the actual sensor offset due the possibility of scattering from within the thin snowpack, but this difference would only be a small portion of the 10 cm thick snow cover. The R26 calibration result is larger (giving a lower retracked elevation) than the SS3 by an average of 8 cm, suggesting that it overestimates the true sensor offset. Since using the R26 offset did not result in a 100% penetration at any threshold under certain surface conditions (Figures A.7f and A.8f), it is possible that Ku-band radar cannot fully penetrate a snowpack that is too deep or whose grain size is too large. Even if a correct sensor offset is established through some

calibration method (runway, leads or corner reflector) the retracked elevation would require an additional correction factor when measured over a snowpack that the Ku-band radar could not penetrate.

The surface characteristics that error E and penetration P are most strongly correlated with are the snow depth and the deformed ice classification. It is possible that a thicker snowpack would result in more volume scattering, obscuring the signal from the ice surface and reducing the accuracy of the retracker, but with a late-March frozen snowpack the effect would be negligible compared to the strong signals of the snow and ice surfaces (Makynen and Hallikainen, 2009). The correlation of error with the snow depth may also be a proxy for the correlation with the deformed ice class, where a rougher, deformed ice surface can collect deeper pockets of snow and shelter them from the wind.

The absolute error relative to the snow depth E_{ra} has no significant correlation with snow depth, but retains a correlation with the ice reformed class, indicating that part of the snow-depth correlation comes from the ice roughness. A deformed ice surface can have an adverse effect on the accuracy, where features within the radar footprint, protruding above the surface level of the ice at the nadir can appear as peaks before the ice surface peak in the waveform, obscuring the main scattering peak and reducing the accuracy of the retracker estimate.

The snow density is negatively correlated with all the measures of error, indicating that a higher density snowpack would reduce the error of the ice-surface elevation estimate. This effect is likely due to the correlation of snow density with the ice deformed class, but could also be caused by the relationship presented in equation 3.9, where the radar signal travels slower through snow that is denser. The maximum snow density observed in this study was $440\,\mathrm{kg/m^3}$ while the minimum was $196.5\,\mathrm{kg/m^3}$, which would yield an 11 percentage point difference in the speed of the radar (73 % vs. 84 % of c). Given a bin size of 10.98 cm in a vacuum, the bin size inside the snowpack can vary up to 1.20 cm (8.02 cm to 9.22 cm) based on changes in the snow density. A smaller bin size would improve the vertical resolution of the radar altimeter and consequently reduce the error of the estimate.

The strongest correlation concerning the measures of error is with characteristics that describe the shape of the trailing edge of the waveform. Both the PP and RW of the

leading edge have weak or insignificant correlations with the error, while the trailing edge RW is the most strongly correlated among all the variables. The reverse is true in the correlation of waveform shape with snow depth and h_{topo}, where the leading edge has a stronger relationship. This is likely because features of the snowpack and the snow surface affect the left side of the return, while features of the ice surface affect the right side of the return.

The ASIRAS waveform returned over a dry snowpack covering sea ice is comprised of three main parts: a weak echo from the air-snow interface, a stronger echo from the snow-ice interface and a negligible echo from the snowpack volume (Makynen and Hallikainen, 2009). Figure 3.22a shows how the echo from the air-snow interface in dry snow skews the returns, extending the width and reducing the PP of the leading edge. This bias is observed in the shape of average waveforms grouped by the the ice deformed class and snow density (Figures 3.15a and c), but is not visible when grouped over the snow depth and h_{topo} (Figures 3.15b and d). The effect of the snow depth and h_{topo} may not be visible because the surface of the snow and snowpack depth are affected by the topology of the ice surface, and their effect on the waveform is obscured by the effect of the ice surface. When the effect ice surface topology is accounted for by separately grouping the waveforms for deformed and undeformed ice (Figure 3.17, the snow depth and h_{topo} appear to have a stronger effect on the leading edge of the waveform, but only over smooth ice. This matches the observations of Makynen and Hallikainen (2009), who produced the results in Figure 3.22 over smooth level ice, and is consistent with the findings of Nandan et al. (2017a) who note that fluctuations in the scattering properties of the snowpack are less detectable over rougher first-year ice since they have a weaker effect than that of ice surface roughness.

Considering the effect of surface characteristics on the non-normalized waveform (Figure 3.15), the results are consistent with the correlation of the same characteristics on the waveform shape, where a positive correlation with PP (negative correlation with RW) shows a shorter, flatter peak as the value of the characteristics increases (ice deformed class, snow depth and h_{topo}) and vice versa (snow density). The average shape of waveforms categorized by the RW and PP in Figure 3.15e-h, shows that the two measures are inversely related. A large RW and a low PP is expressed by waveforms that are flat and wide, which is consistent with the shape properties that the values are intended to measure. The RW

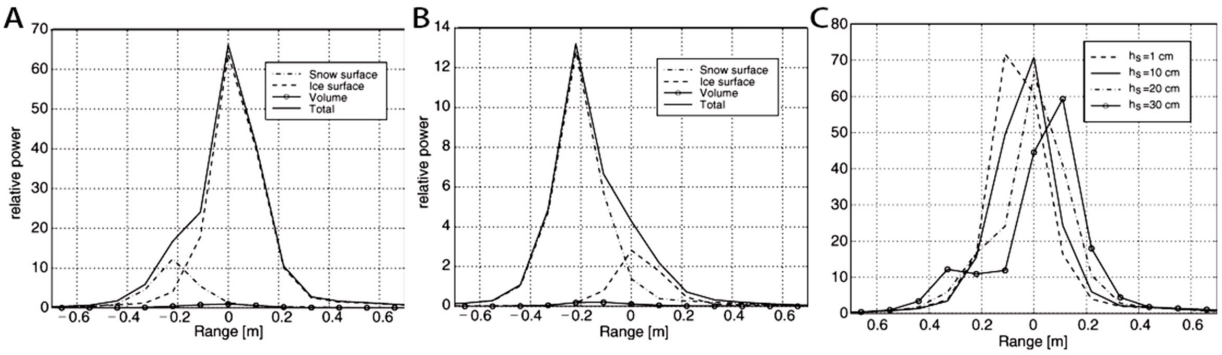

Figure 3.22: Selected figures of simulations of ASIRAS radar return waveforms over snow covered smooth, level sea ice from Makynen and Hallikainen (2009). A) dry snow cover of 20 cm B) Moist snow cover (volumetric wetness 1%) of 20 cm C) Dry snow cover at snow thicknesses of 1 to 30 cm.

and PP ratios appear to indicate the waveform's skew, with a low PP ratio (left-skewed) representing waveforms like those of dry snow in Figure 3.15a, and a high PP ratio (right-skewed) for waveforms of moist snow in Figure 3.15b, with the effect of the RW being inverted.

Unskewed or left-skewed is the expected shape for an echo returned over bare or dry-snow covered sea ice. A right-skewed echo may suggest the presence of moisture in the snow, but can also be due other factors. The right skewed waveforms that make up the Figure 3.21h high PP ratio class are unlikely to be caused by a moist snowpack, since snow temperature ranged between $-32\,°C$ and $-14\,°C$. Figure 3.22c shows that waveform shifts from right to left skewed as the snow depth increases and backscatter near the snow surface increases in magnitude. A weak version of this effect is observed over undeformed ice (Figure 3.16a) but is not supported by by the low and non-significant correlation of snow depth with the RW and PP ratio. Another cause may be a surface that is convex towards the radar emitter. When the elevation of the nadir is higher than the surrounding surface, the signal scatters from the surface for a longer period of time after the peak, stretching the trailing edge.

The right-skewed echo in Figure 3.22b is caused by moisture, but scattering within the snowpack and at the snow surface can also be caused by other factors. Radar scattering

occurs where there is a contrast in the dielectric permittivity between the medium it is travelling through and the medium it is entering. This contrast exists at the snow-air and snow-ice interfaces, but may also occur within the snowpack where salinity is present or where there are perturbations in snow properties such as snow grain radius Nandan et al., 2017a. Snow properties collected from snow pits and correlated with the echoes of nearby returns (Figure 3.19) showed that only the average grain size ratio significantly correlated with the waveform shape ratios, where a grain size ratio closer to 1 (rounder grain) was observed in returns that had the right-skewed shape. Nandan et al. (2017a) found that the salinity and grain size of the snow had the strongest effect on the Ku-band radar penetration, with snow density and temperature having a weaker influence. In a correlation of these properties with the measures of estimate error, only measures of snow grain size had a significant relationship. When the snow properties were compared to the average waveform shape (Figure 3.21), salinity was found to have a stronger influence than the grain size. The binary measurement of salinity presence in the snowpack had the strongest effect on the return power, but an increase in average snowpack salinity among pits who had saline layers did not cause a significant change in the waveform shape.

The results of this study suggest that the model for estimating snow-ice interface from Ku-band radar model could be improved by integrating the coupled effects of retracker threshold and surface properties on the radar signal. An ideal retracker threshold could be calculated based on the surface properties, with an additional correction factor for when observing a snowpack that inhibits full penetration. Since the final goal is to estimate sea ice freeboard at the Arctic scale, the surface properties would have to be measured or estimated without detailed in-situ measurements. The ice deformity in this study was based on C-band observations from the RADARSAT-2, whose coverage extends into the Arctic. Snow depth measurements were collected in the field, but previous studies have used the Warren 1999 climatology with a coefficient applied to account for changes due to Arctic warming (Laxon et al., 2013). Snow stratigraphy can also be estimated based on climatology and the sea ice type (Sturm et al., 2002). The analysis in section 3.3.5 found that snow depth, stratigraphy and salinity properties have an effect on the waveform shape, which open the possibility of using the waveform to directly estimate the a correction factor that would bring the retracked elevation closer to the actual snow-ice interface.

Future studies can potentially improve on these findings by collecting similar data with a more reliable offset between the radar and laser altimeter sensors. This could be done by flying over a flat, bare runway surface or open water. The ideal method would be to setup a corner reflector along the snow depth observations track (Willatt et al., 2011). Once the two sensors are reliably aligned, the position of the snow-ice interface can be accurately determine within the radar range window. Properties of the waveform shape and remotely sensor characteristics of the surface (such as ice deformity) can be analyzed and compared to the snow-ice interface elevation to build a model which more accurately predicts the ice surface elevation than using a single retracking threshold.

3.5 Conclusion

The objectives of this study were to evaluate the ASIRAS Ku-band radar penetration into the snowpack, its ability to measure the snow-ice interface elevation, investigate how these are affected by surface properties and explore methods which could improve the accuracy of the elevation estimate. Penetration P was estimated by calculating the distance between the snow surface s_{as}, observed by the ALS laser altimeter, and the elevation retracked from the ASIRAS radar altimetry signal s_r. The retracked elevation is intended to represent the snow-ice interface, and its distance to ice surface calculated from snow depths observed in the field s_{si} was the snow-ice interface estimate accuracy E.

Observations from the ASIRAS instrument appear below the ALS and require an offset to align them. The R23 and R26 calibrations used returns collected over a runway on two adjacent dates, while the SS3 calibration used returns over shallow snow covering flat ice in the Grid 3 zone. The R23 and SS3 methods yielded similar results (Figures 3.4 and 3.6), while the R26 method calibrated a large offset distance, resulting in a deeper estimated penetration P, a retracked elevation that was on average closer to the snow-ice interface and a lower error E.

The estimate of penetration P and error E were found to vary depending on the size of the footprint used to aggregate the ALS and snow depth observations to each ASIRAS radar return. Over a flat surface, the ASIRAS footprint should have been a rectangle with

a width of 20 meters by 2 meters. Aggregating surface observations to ASIRAS nadirs at a distance of 15 to 20 meters was found to minimize the mean and standard deviation of the penetration and relative to the snow depth P_r and E_{ra} (Figure 3.7), likely because it accounts for the spatial variability introduced by ice surface roughness and the spatial autocorrelation the of the snow and ice surfaces.

Selection of the retracker threshold was found to have a positive effect on the penetration distance P and relative penetration P_r. The properties of the surface affected both the starting penetration (at a threshold of 20%) and the rate at which penetration increased with threshold. A deformed ice surface, deeper snow cover, absence of salinity and larger grain size all caused the slope of the trend to increase. Even at the highest threshold of 100% the retracked elevation calculated using the SS3 and R23 calibrations were not able to achieve an average penetration of 100%. Applying the R26 calibration could result in an average 100% penetration, but the ideal threshold depended on the properties of the snow and ice surface, and could not be reached under some conditions.

The measures of estimate error P_r and E_{ra} were found to correlate slightly with surface characteristics such as the classification of ice deformity and snow density, and moderately with the measures of the waveform shape: pulse peakiness (PP) and return width (RW) (Figure 3.14). The measures of error had a much stronger correlation with the trailing edge (right of peak) of the waveform than the leading edge (left of peak). This effect could be seen as changes in the average waveform shape between stratified classes of variables correlated with the waveform shape (Figures 3.15,3.16 and 3.17).

Among snow properties collected from snow pits (salinity, stratigraphy, temperature and density), only the grain size was correlated with any measures of error (Figure 3.18). Salinity and grain size were also found to correlate with the waveform shape (Figure 3.19), but only the presence of salinity had a visible effect on the waveform, showing a significant reduction in return power when absent (Figure 3.20).

The results of this study suggest that estimating the snow-ice interface from Ku-band radar using the TFMRA method with a single retracker is not reliable due to the effects of various ice surface and snowpack characteristics on the penetration-threshold relationship. There may be potential to improve the accuracy of the snow-ice interface estimate by ap-

plying a correction factor to a retracked elevation to account for incomplete penetration of Ku-band radar. This correction factor could be modeled based on remotely sensed surface characteristics (such as ice deformity) and the waveform shape, but constructing such a model would require a more accurate alignment between the radar and laser altimeters. This alignment may be achieved by collecting observations over a flat and bare runway, open water, or through he setup of a corner reflector along the ground observations track.

Chapter 4

General Conclusions

4.1 Summary

One of the current methods for estimating Arctic sea ice thickness employs CryoSat-2's Ku-band SIRAL radar altimeter to measure the elevation of the sea ice freeboard (Kwok and Markus, 2018). For an ice floe in hydrostatic equilibrium, sea ice thickness can be calculated from the ice freeboard and snow depth based on a distribution model that combines airborne and ground surveys of the Arctic (R. Kwok and G. F. Cunningham, 2015; Laxon et al., 2013).

Ice freeboard measurement from CryoSat-2 relies on the assumption that Ku-band radar fully penetrates the snowpack and scatters primarily from the snow-ice interface, which was based on lab simulations performed by Beaven et al. (1995). Hendricks et al. (2010) and Willatt et al. (2011) both found that ASIRAS, an airborne version of CryoSat-2's Ku-band SIRAL radar altimeter, did not fully penetrate snow over sea ice. The observations were recorded in May when snow temperatures were near freezing (-4C to -8C), so metamorphosis or moisture could have impacted the result (Gerland et al., 2012). Ricker et al. (2014) identified systematic uncertainties in the ice thickness estimate that were caused by the lack of a known ideal retracker threshold and the unknown penetration of radar through snow. They recommended analysing the radar signal over snow covered sea ice at various thresholds and in different locations. Robert Ricker et al. (2015) concluded that the

presence of snow over the sea ice was responsible for uncertainty in the CryoSat-2 sea ice freeboard estimate. Nandan et al. (2017b) found that the presence of saline layers and permittivity contrast caused by perturbations in density and stratigraphy among snowpack layers resulted in the reduction of the Ku-band radar penetration through the snowpack.

The aim of this study was to improve the understanding of the freeboard estimate uncertainty by comparing an observed snow-ice interface elevation with the dominant scattering interface retracked from Ku-band radar altimetry. The radar altimetry signal was acquired from an ASIRAS radar altimeter flown over snow-covered landfast sea ice, and the observed snow-ice interface elevation was obtained by subtracting in-situ snow depth measurements from laser altimeter elevations of the snow surface from the ALS sensor. Due to the absence of a calibration surface, the offset between the ASIRAS and ALS sensor could not be reliably established. Alternative calibration methods were used, but could not be used to accurately determine the penetration distance of the radar through the snowpack. Despite this limitation, insights were gained by investigating results that remained consistent across different sensor offsets.

Increasing the retracker threshold caused the estimated penetration to increase, and the function of this relationship was dependent on the surface properties. The slope of the trend was increased by a deformed ice surface, a deeper snow cover, an absence of salinity and a larger snow grain size. As a result, the ideal retracked threshold, one that would achieve 100% penetration, varies depending on properties of the surface being observed. The R26 calibration method resulted in a larger overall estimated penetration, and a lower error due to the average retracked elevation's closer proximity to the snow-ice interface, but the threshold-penetration trends were consistent across all offsets. Even with the likely overestimated offset of the R26 calibration, the retracked elevation did not penetrate fully through the snowpack at any threshold under surface conditions where the snow was too deep or the snow grain size was too large.

These results suggest that using a single threshold with the TFMRA retracking method will not yield a reliable estimate of the snow-ice interface when observed over an area with diverse surface properties. Even at a 100% threshold, the TFMRA method can overestimate the snow-ice interface elevation, and requires an additional offset to account for the inability of the Ku-band radar to penetration the snowpack under some surface

conditions. There may be potential to improve the retracking method by incorporating knowledge of the sensed surface to select an appropriate retracker threshold, and apply an additional correction factor in areas where a 100% retracker threshold does not yield a full penetration of the snowpack.

4.2 Limitations

The primary limitation of this study is the uncertainty in the elevation offset between the radar altimeter (ASIRAS) and laser altimeter (ALS) measurements. This limitation is present due to the lack of a calibrating surface along the flight path from which both sensors would reflect with minimal penetration, such as a runway, bare ice or open water. Since ALS is assumed to be the snow surface elevation and is combined with the snow depth observations to calculate the ice surface elevation, uncertainties in the relative elevation of the ASIRAS and ALS data prevent an accurate interpretation of the radar waveform location relative to the boundaries of the snowpack. The runway calibration R23 and R26 could not be used as a definitive calibration since there was a difference of 5 to 15 cm between their offset results (Figure 3.4), suggesting that some property of the instrument setup affecting the offset changed between flights. The shallow snow calibration method is also unreliable because the Ku-band radar is not expected to fully penetrate the approximately 10 cm snow cover over the observations used in the calibration, underestimating the actual sensor offset. The sensor offset uncertainty could be addressed by using a corner reflector placed along the track and observed by the ASIRAS radar altimeter. Given the height of the corner reflector's apex above the snow surface, the location of the corner reflector's apex in the radar signal could be used to align the ASIRAS and ALS sensors (Willatt et al., 2011).

Another component of uncertainty in the results is the size and shape of the footprint that represents the area of the surface that affects the observed ASIRAS radar waveform. Based on the flight parameters and documentation (Section 3.2) the footprint over a flat surface should be approximately 2 meters in the long-track and 20 meters in the across-track direction, but the analysis in Section 3.3.1 suggested that the actual area of the surface

observed by the ASIRAS radar altimeter is larger, likely due to the surface roughness. This analysis could be improved by investigating the effect of scaling the footprint in the along and across-track direction independently, but there would still be uncertainty in how much of the effect is due to spatial autocorrelation in the surface properties versus the ice surface roughness.

The relationships between penetration P, ice surface estimate error E, waveform shape, surface properties and retracker threshold analysed in Sections 3.3.3 and 3.3.4 might not be as strong for CryoSat-2 due to its larger footprint. The ASIRAS platform is flown at a much lower altitude than CryoSat-2 (350 m compared to 730 km) and its 2 m along and 20 m across-track footprint is significantly smaller than the CryoSat-2 footprint, which varies between 13.6 km to 14.4 km along and 14.9 km to 15.8 km across-track (Scagliola, 2013). Since the larger CryoSat-2 footprint likely covers a more diverse range of surface features values, the small perturbations observed at the meters-scale might not have as large of an effect at the kilometers-scale scale due to aggregation. A model developed using ASIRAS observation would show potential for improving CryoSat-2 estimates, but it would have to be refitted using data that are aggregated to or cover the same scale as the CryoSat-2 footprint.

4.3 Recommendations

The results and insights from this study show that there is potential for future research that could improve the methods by which the sea ice surface elevation is estimated from Ku-band radar altimetry. Despite the limitations of the data used this study, further analyses can still be performed to develop a better understanding of the relationship between the radar altimetry signal, surface properties and the sea ice surface estimate.

This study only evaluated the threshold first-maxima retracker (TFMRA) method, but R. Kwok and G. F. Cunningham (2015) presented an alternative method for retracking the ice surface using the the centroid of the of the waveform area between the first unambiguous peak (with no local maxima in its leading edge) and the half-power point of the same peak. Kwok (2014) found this method to be less sensitive to scattering from the air-snow interface

and the snowpack, so its ice surface elevation estimate should be tested against the TFMRA results in Section 3.3.3 to determine to how it responds to difference surface conditions and whether the retracked elevation it produces fully penetrates the snowpack under the least favorable circumstances, such as deep snow or deformed ice.

As Section 3.3.4 indicated that the shape of the waveform and ice deformity has a significant correlation with the ice surface estimate error, there may be an opportunity to improve the TFMRA method by incorporating these properties into the retracking calculation. A linear regression combining the waveform shape parameters and ice deformation could provide an appropriate retracked threshold, which would exceed 100% where the peak elevation would not fully penetrate the snowpack, or estimate an additional offset to account for the incomplete penetration of Ku-band radar. The pulse peakiness and return width in this study were calculated using a margin of 3 returns and a threshold of 1% respectively based on current literature (Ricker et al., 2014; Zygmuntowska et al., 2013), but testing alternative values for these calculations may improve the fit of the model. A more complex method can apply a gaussian fit to the main waveform peak (Zygmuntowska et al., 2013) and used its mean and distribution parameters as inputs to estimate the retracker threshold, or use the power at spaced peak thresholds to estimate the retracking elevation as an offset from the peak directly.

Even if different models or methods are applied to the data used in this study, the results will be limited by the uncertainty in the sensor offset. Future studies and campaigns would benefit from securing a calibrating surface close to the observation track, or within the same flight. If the sensor offset is established, the observed relationship between the surface characteristics, waveform characteristics and ice surface elevation can give reliable insight into how Ku-band radar interacts with Arctic sea ice and its snow cover. An improved retracking model developed from these insights can then evaluated against CryoSat-2, Arctic-scale data, which would test the spatial limitations of this study. Since the ASIRAS radar has a much smaller footprint than CryoSat-2 and only covers a thin track of ice, interpretations based on its observations may be biased in the along-track direction and not yield the same relationship between surface characteristics and accuracy when applied to a wider coverage. To reduce these spatial alignment biases, the improved model must ingest observations that are measured at the same scale as the CryoSat-2, or that are

aggregated from multiple observations within the footprint that are evenly distributed to minimize bias.

If the proposed method can be shown to improve the accuracy of the radar freeboard estimate in approximating the true ice freeboard, it would have a positive impacts on the ability to measure the properties of sea ice. An improved location of the ice surface would reduce uncertainty not only in the ice freeboard estimate, but also improve the reliability of a snow depth estimation approach that combines the CryoSat-2 ice surface with an ICESat-2 snow surface (Kwok and Markus, 2018). Since snow load is a component of the hydrostatic equilibrium model used to calculate sea ice thickness from ice freeboard, improving the ice surface elevation estimate would yield a multi-pronged benefit to sea ice monitoring.

References

Aagard, K, and E.C.Carmack. 1989. "The role of sea ice and other fresh water in the Arctic circulation." *Journal of Geophysical Research* 94:14, 414–485, 498. ISSN: 0148-0227. doi:10.1029/JC094iC10p14485.

Akitaya, Eizi. 1974. "Studies on Depth Hoar": 68.

Beaven, S. G, G. L Lockhart, S. P Gogineni, A. R Hosseinmostafa, K. Jezek, AJ Gow, D. K Perovich, A. K Fung, and S. Tjuatja. 1995. "Laboratory measurements of radar backscatter from bare and snow-covered saline ice sheets." *International journal of remote sensing* 16:851–876. ISSN: 01431161, 13665901. doi:10.1080/01431169508954448.

Bourke, Robert H., and Robert P. Garrett. 1987. "Sea ice thickness distribution in the Arctic Ocean." *Cold Regions Science and Technology* 13 (April): 259–280. ISSN: 0165232X. doi:10.1016/0165-232X(87)90007-3.

Brath, Manfred, Stefan Kern, and Detlef Stammer. 2013. "Sea Ice Classification During Freeze-Up Conditions With Multifrequency Scatterometer Data." *IEEE Transactions on Geoscience and Remote Sensing* 51 (June): 3336–3353. ISSN: 0196-2892, 1558-0644. doi:10.1109/TGRS.2012.2222031.

Carsey, Frank D., ed. 1992. *Microwave remote sensing of sea ice.* Geophysical monograph. Washington, DC: American Geophysical Union. ISBN: 978-0-87590-033-9.

Chiles, Jean-Paul, and Pierre Delfiner. 2012. *Geostatistics: modeling spatial uncertainty.* 2nd ed. Wiley series in probability and statistics. Hoboken, N.J: Wiley. ISBN: 978-0-470-18315-1.

Curry, Judith A., Julie L. Schramm, and Elizabeth E. Ebert. 1995. "Sea Ice-Albedo Climate Feedback Mechanism." *Journal of Climate* 8 (February): 240–247. ISSN: 0894-8755. doi:10.1175/1520-0442(1995)008<0240:SIACFM>2.0.CO;2.

Day, J. J., E. Hawkins, and S. Tietsche. 2014. "Will Arctic sea ice thickness initialization improve seasonal forecast skill?" *Geophysical Research Letters* 41 (November): 7566–7575. ISSN: 00948276. doi:10.1002/2014GL061694.

Derocher, Ae, M Andersen, Ø Wiig, J Aars, E Hansen, and M Biuw. 2011. "Sea ice and polar bear den ecology at Hopen Island, Svalbard." *Marine Ecology Progress Series* 441 (November): 273–279. ISSN: 0171-8630, 1616-1599. doi:10.3354/meps09406.

Descamps, Sébastien, Jon Aars, Eva Fuglei, Kit M. Kovacs, Christian Lydersen, Olga Pavlova, Åshild Ø. Pedersen, Virve Ravolainen, and Hallvard Strøm. 2017. "Climate change impacts on wildlife in a High Arctic archipelago - Svalbard, Norway." *Global Change Biology* 23 (February): 490–502. ISSN: 13541013. doi:10.1111/gcb.13381.

Edwards, Margo H., and Bernard J. Coakley. 2003. "SCICEX Investigations of the Arctic Ocean System." *Geochemistry* 63:281–328. ISSN: 00092819. doi:10.1078/0009-2819-00039.

Evans, S. 1965. "Dielectric Properties of Ice and Snow–a Review." *Journal of Glaciology* 5:773–792. ISSN: 0022-1430, 1727-5652. doi:10.3189/S0022143000018840.

Forsström, Sanja, Sebastian Gerland, and Christina A. Pedersen. 2011. "Thickness and density of snow-covered sea ice and hydrostatic equilibrium assumption from in situ measurements in Fram Strait, the Barents Sea and the Svalbard coast." *Annals of Glaciology* 52:261–270. ISSN: 0260-3055, 1727-5644. doi:10.3189/172756411795931598.

Freitas, C, Km Kovacs, M Andersen, J Aars, S Sandven, M Skern-Mauritzen, O Pavlova, and C Lydersen. 2012. "Importance of fast ice and glacier fronts for female polar bears and their cubs during spring in Svalbard, Norway." *Marine Ecology Progress Series* 447 (February): 289–304. ISSN: 0171-8630, 1616-1599. doi:10.3354/meps09516.

Frey, Othmar, Charles L. Werner, and Andreas Wiesmann. 2015. "Tomographic profiling of the structure of a snow pack at X-/Ku-Band using SnowScat in SAR mode." In *2015 European Radar Conference (EuRAD),* 21–24. Paris, France: IEEE, September. ISBN: 978-2-87487-041-5. doi:10.1109/EuRAD.2015.7346227.

Gerland, Sebastian, Angelika H H Renner, Gunnar Spreen, Caixin Wang, Justin Beckers, Mats A Granskog, Jari Haapala, et al. 2012. "In-Situ calibration and validation of CryoSat-2 observations over Arctic sea ice north of Svalbard": 4.

Hallikainen, M., F. Ulaby, and M. Abdelrazik. 1986. "Dielectric properties of snow in the 3 to 37 GHz range." *IEEE Transactions on Antennas and Propagation* 34 (November): 1329–1340. ISSN: 0096-1973. doi:10.1109/TAP.1986.1143757.

Hansen, B. B., R. Aanes, and B.-E. Sæther. 2010. "Partial seasonal migration in high-arctic Svalbard reindeer (Rangifer tarandus platyrhynchus)." *Canadian Journal of Zoology* 88 (December): 1202–1209. ISSN: 0008-4301, 1480-3283. doi:10.1139/Z10-086.

Hawley, R. L., E. M. Morris, R. Cullen, U. Nixdorf, A. P. Shepherd, and D. J. Wingham. 2006. "ASIRAS airborne radar resolves internal annual layers in the dry-snow zone of Greenland." *European Space Agency, (Special Publication) ESA SP* 33:1–5. ISSN: 03796566. doi:10.1029/2005GL025147.

Helm, V., A. Humbert, and H. Miller. 2014. "Elevation and elevation change of Greenland and Antarctica derived from CryoSat-2." *The Cryosphere* 8 (August): 1539–1559. ISSN: 1994-0424. doi:10.5194/tc-8-1539-2014.

Hendricks, Stefan, Lars Stenseng, Veit Helm, and Christian Haas. 2010. "Effects of surface roughness on sea ice freeboard retrieval with an Airborne Ku-Band SAR radar altimeter": 3126–3129.

Hitchcock, R. Timothy. 2004. *Radio-frequency and microwave radiation.* 3rd ed. Nonionizing radiation guide series. Fairfax, Va: American Industrial Hygiene Association. ISBN: 978-1-931504-55-3.

Hvidegaard, S. M., J. E. Nielsen, S. L. Sandbjerg Sørensen, S. B. Simonsen, H. Skourup, V. Helm, and T. Bjerg. 2014. *ESA CryoVEx 2014 - Airborne ASIRAS radar and laser scanner measurements during 2014 CryoVEx campaign in the Arctic.* Technical report. European Space Agency.

Ivanova, N., L. T. Pedersen, R. T. Tonboe, S. Kern, G. Heygster, T. Lavergne, A. Sørensen, et al. 2015. "Satellite passive microwave measurements of sea ice concentration: an optimal algorithm and challenges." *The Cryosphere Discussions* 9 (February): 1269–1313. ISSN: 1994-0440. doi:10.5194/tcd-9-1269-2015.

Kern, S., K. Khvorostovsky, H. Skourup, E. Rinne, Z. S. Parsakhoo, V. Djepa, P. Wadhams, and S. Sandven. 2015. "The impact of snow depth, snow density and ice density on sea ice thickness retrieval from satellite radar altimetry: Results from the ESA-CCI Sea Ice ECV Project Round Robin Exercise." *Cryosphere* 9:37–52. ISSN: 19940424. doi:10.5194/tc-9-37-2015.

King, Jennifer, Henriette Skourup, Sine M. Hvidegaard, Anja Rösel, Sebastian Gerland, Gunnar Spreen, Chris Polashenski, Veit Helm, and Glen E. Liston. 2018. "Comparison of Freeboard Retrieval and Ice Thickness Calculation From ALS, ASIRAS, and CryoSat-2 in the Norwegian Arctic, to Field Measurements Made During the N-ICE2015 Expedition." *Journal of Geophysical Research: Oceans* 123. ISSN: 21699275. doi:10.1002/2017JC013233.

King, Joshua, Chris Derksen, Peter Toose, Alexandre Langlois, Chris Larsen, Juha Lemmetyinen, Phil Marsh, et al. 2018. "The influence of snow microstructure on dual-frequency radar measurements in a tundra environment." *Remote Sensing of Environment* 215:242–254. ISSN: 00344257. doi:10.1016/j.rse.2018.05.028.

King, Joshua, Stephen Howell, Chris Derksen, Nick Rutter, Peter Toose, Justin F. Beckers, Christian Haas, Nathan Kurtz, and Jacqueline Richter-Menge. 2015. "Evaluation of Operation IceBridge quick-look snow depth estimates on sea ice." *Geophysical Research Letters* 42:9302–9310. ISSN: 19448007. doi:10.1002/2015GL066389.

Kovacs, Austin, and Rexford M. Morey. 1978. "Radar anisotropy of sea ice due to preferred azimuthal orientation of the horizontal *c* axes of ice crystals." *Journal of Geophysical Research* 83:6037. ISSN: 0148-0227. doi:10.1029/JC083iC12p06037.

Kurtz, N. T., S. L. Farrell, M. Studinger, N. Galin, J. P. Harbeck, R. Lindsay, V. D. Onana, B. Panzer, and J. G. Sonntag. 2013. "Sea ice thickness, freeboard, and snow depth products from Operation IceBridge airborne data." *Cryosphere* 7:1035–1056. ISSN: 19940416. doi:10.5194/tc-7-1035-2013.

Kurtz, Nathan T, and Sinead L Farrell. 2011. "Large-scale surveys of snow depth on Arctic sea ice from Operation IceBridge." *Geophysical Research Letters* 38. ISSN: 00948276. doi:10.1029/2011GL049216.

Kwok, R. 2014. "Simulated effects of a snow layer on retrieval of CryoSat-2 sea ice freeboard." *Geophysical Research Letters* 41:5014–5020. ISSN: 19448007. doi:10.1002/2014GL060993.

———. 2018. "Arctic sea ice thickness, volume, and multiyear ice coverage: losses and coupled variability (1958–2018)." *Environmental Research Letters* 13 (October): 105005. ISSN: 1748-9326. doi:10.1088/1748-9326/aae3ec.

Kwok, R., and G. F. Cunningham. 2015. "Variability of Arctic sea ice thickness and volume from CryoSat-2." *Philosophical Transactions of the Royal Society A: Mathematical, Physical and Engineering Sciences* 373 (July): 20140157. ISSN: 1364-503X, 1471-2962. doi:10.1098/rsta.2014.0157.

Kwok, R., G. F. Cunningham, M. Wensnahan, I. Rigor, H. J. Zwally, and D. Yi. 2009. "Thinning and volume loss of the Arctic Ocean sea ice cover: 2003–2008." *Journal of Geophysical Research* 114 (July). ISSN: 0148-0227. doi:10.1029/2009JC005312.

Kwok, R, and C Haas. 2015. "Effects of radar side-lobes on snow depth retrievals from Operation IceBridge." *Journal of Glaciology* 61:576–584. ISSN: 00221430. doi:10.3189/2015JoG14J229.

Kwok, R, and T Markus. 2018. "Potential basin-scale estimates of Arctic snow depth with sea ice freeboards from CryoSat-2 and ICESat-2: An exploratory analysis." *Advances in Space Research* 62:1243–1250. ISSN: 0273-1177. doi:10.1016/j.asr.2017.09.007.

Kwok, R, B Panzer, C Leuschen, S Pang, T Markus, B Holt, and S Gogineni. 2011. "Airborne surveys of snow depth over Arctic sea ice." *Journal of Geophysical Research* 116 (November): C11018. ISSN: 0148-0227. doi:10.1029/2011JC007371.

Kwok, Ron. 2004. "ICESat observations of Arctic sea ice: A first look." *Geophysical Research Letters* 31:L16401. ISSN: 0094-8276. doi:10.1029/2004GL020309.

Kwok, Ron, and G F Cunningham. 2008. "ICESat over Arctic sea ice: Estimation of snow depth and ice thickness." *Journal of Geophysical Research: Oceans* 113. ISSN: 21699291. doi:10.1029/2008JC004753.

Kwok, Ron, Nathan T. Kurtz, Ludovic Brucker, Alvaro Ivanoff, Thomas Newman, Sinead L. Farrell, Joshua King, et al. 2017. "Intercomparison of snow depth retrievals over Arctic sea ice from radar data acquired by Operation IceBridge." *The Cryosphere* 11 (November): 2571–2593. ISSN: 1994-0424. doi:10.5194/tc-11-2571-2017.

Lacomme, Philippe, ed. 2001. *Air and spaceborne radar systems: an introduction.* Norwich, N.Y: William Andrew Publishing. ISBN: 978-0-85296-981-6 978-1-891121-13-5.

Laxon, Seymour W, Katharine A Giles, Andy L Ridout, Duncan J Wingham, Rosemary Willatt, Robert Cullen, Ron Kwok, et al. 2013. "CryoSat-2 estimates of Arctic sea ice thickness and volume." *Geophysical Research Letters* 40:732–737. ISSN: 19448007. doi:10.1002/grl.50193.

Lentz, H., H.-M. Braun, M. Younis, C. Fischer, W. Wiesbeck, and C. Mavrocordatos. 2002. "Concept and realization of an Airborne SAR/Interferometric Radar Altimeter System (ASIRAS)." *IEEE International Geoscience and Remote Sensing Symposium (IGARSS)* 6:3099–3101. doi:10.1109/IGARSS.2002.1027097.

Lindstad, Haakon, Ryan M. Bright, and Anders H. Strømman. 2016. "Economic savings linked to future Arctic shipping trade are at odds with climate change mitigation." *Transport Policy* 45 (January): 24–30. ISSN: 0967070X. doi:10.1016/j.tranpol.2015.09.002.

Liu, Xing-he, Long Ma, Jia-yue Wang, Ye Wang, and Li-na Wang. 2017. "Navigable windows of the Northwest Passage." *Polar Science* 13 (September): 91–99. ISSN: 18739652. doi:10.1016/j.polar.2017.02.001.

Maaß, N, L Kaleschke, X Tian-Kunze, and M Drusch. 2013. "Snow thickness retrieval over thick Arctic sea ice using SMOS satellite data." *Cryosphere* 7:1971–1989. ISSN: 19940416. doi:10.5194/tc-7-1971-2013.

Makynen, Marko P., and Martti T. Hallikainen. 2009. "Simulation of asiras altimeter echoes for snow-covered first-year sea ice." *IEEE Geoscience and Remote Sensing Letters* 6:486–490. ISSN: 1545598X. doi:10.1109/LGRS.2009.2015968.

Mallett, Robbie D. C., Isobel R. Lawrence, Julienne C. Stroeve, Jack C. Landy, and Michel Tsamados. 2019. "Brief Communication: Conventional assumptions involving the speed of radar waves in snow introduce systematic underestimates to sea ice thickness and seasonal growth rate estimates." doi:10.5194/tc-2019-198.

Mätzler, Christian. 1987. "Applications of the interaction of microwaves with the natural snow cover." *Remote Sensing Reviews* 2 (January): 259–387. ISSN: 0275-7257. doi:10.1080/02757258709532086.

Mavrocordatos, C, E Attema, M Davidson, H. Lentz, and U. Nixdorf. 2004. "Development of ASIRAS (airborne SAR/interferometric altimeter system)." In *IEEE International IEEE International IEEE International Geoscience and Remote Sensing Symposium, 2004. IGARSS '04. Proceedings. 2004,* 4:2465–2467. IEEE. ISBN: 0-7803-8742-2. doi:10.1109/IGARSS.2004.1369792.

Maykut, GA. 1985. "The Ice Environment." In *Sea Ice Biota.* CRC Press.

McPhee, Miles G., Timothy P. Stanton, James H. Morison, and Douglas G. Martinson. 1998. "Freshening of the upper ocean in the Arctic: Is perennial sea ice disappearing?" *Geophysical Research Letters* 25 (May): 1729–1732. ISSN: 00948276. doi:10.1029/98GL00933.

Melia, N., K. Haines, and E. Hawkins. 2016. "Sea ice decline and 21st century trans-Arctic shipping routes: Trans-Arctic shipping in the 21st Century." *Geophysical Research Letters* 43 (September): 9720–9728. ISSN: 00948276. doi:10.1002/2016GL069315.

Nakata, Kazuki, Kay I. Ohshima, and Sohey Nihashi. 2019. "Estimation of Thin-Ice Thickness and Discrimination of Ice Type From AMSR-E Passive Microwave Data." *IEEE Transactions on Geoscience and Remote Sensing* 57 (January): 263–276. ISSN: 0196-2892, 1558-0644. doi:10.1109/TGRS.2018.2853590.

Nakawo, M., and N.K. Sinha. 1984. "A note on brine layer spacing of first-year sea ice." *Atmosphere-Ocean* 22 (June): 193–206. ISSN: 0705-5900, 1480-9214. doi:10.1080/07055900.1984.9649193.

Nandan, Vishnu, Torsten Geldsetzer, Tanvir Islam, John J. Yackel, Jagvijay P S Gill, Mark C. Fuller, Grant Gunn, and Claude Duguay. 2016. "Ku-, X- and C-band measured and modeled microwave backscatter from a highly saline snow cover on first-year sea ice." *Remote Sensing of Environment* 187:62–75. ISSN: 00344257. doi:10.1016/j.rse.2016.10.004.

Nandan, Vishnu, Torsten Geldsetzer, John J. Yackel, Tanvir Islam, Jagvijay P.S. Gill, and Mallik Mahmud. 2017a. "Multifrequency Microwave Backscatter from a Highly Saline Snow Cover on Smooth First-Year Sea Ice: First-Order Theoretical Modeling." *IEEE Transactions on Geoscience and Remote Sensing* 55:2177–2190. ISSN: 01962892. doi:10.1109/TGRS.2016.2638323.

Nandan, Vishnu, Torsten Geldsetzer, John Yackel, Mallik Mahmud, Randall Scharien, Stephen Howell, Joshua King, Robert Ricker, and Brent Else. 2017b. "Effect of Snow Salinity on CryoSat-2 Arctic First-Year Sea Ice Freeboard Measurements." *Geophysical Research Letters* 44:10, 419–10, 426. ISSN: 19448007. doi:10.1002/2017GL074506.

Naoki, Kazuhiro, Jinro Ukita, Fumihiko Nishio, Masashige Nakayama, Josefino C. Comiso, and Al Gasiewski. 2008. "Thin sea ice thickness as inferred from passive microwave and in situ observations." *Journal of Geophysical Research* 113 (February). ISSN: 0148-0227. doi:10.1029/2007JC004270.

Newman, Thomas, Sinead L. Farrell, Jacqueline Richter-Menge, Laurence N. Connor, Nathan T. Kurtz, Bruce C. Elder, and David McAdoo. 2014. "Assessment of radar-derived snow depth over Arctic sea ice." *Journal of Geophysical Research: Oceans* 119 (December): 8578–8602. ISSN: 21699275. doi:10.1002/2014JC010284.

Notz, Dirk, and Julienne Stroeve. 2016. "Observed Arctic sea-ice loss directly follows anthropogenic CO2 emission." *Science* 354 (November): 747–750. ISSN: 0036-8075, 1095-9203. doi:10.1126/science.aag2345.

Overland, James E., and Muyin Wang. 2013. "When will the summer Arctic be nearly sea ice free?" *Geophysical Research Letters* 40:2097–2101. ISSN: 00948276. doi:10.1002/grl.50316.

Overland, James, Jennifer A. Francis, Richard Hall, Edward Hanna, Seong Joong Kim, and Timo Vihma. 2015. "The melting arctic and midlatitude weather patterns: Are they connected?" *Journal of Climate* 28 (October): 7917–7932. ISSN: 08948755. doi:10.1175/JCLI-D-14-00822.1.

Parkinson, Claire L, Donald J Cavalieri, Per Gloersen, H Jay Zwally, and Josefino C Comiso. 1999. "Arctic sea ice extents, areas, and trends, 1978-1996." *Journal of Geophysical Research: Oceans* 104 (September): 20837–20856. ISSN: 01480227. doi:10.1029/1999JC900082.

Peacock, Neil R, and Seymour W Laxon. 2004. "Sea surface height determination in the Arctic Ocean from ERS altimetry." *Journal of Geophysical Research C: Oceans* 109. ISSN: 01480227. doi:10.1029/2001JC001026.

Peings, Yannick, and Gudrun Magnusdottir. 2014. "Response of the wintertime northern hemisphere atmospheric circulation to current and projected arctic sea ice decline: A numerical study with CAM5." *Journal of Climate* 27 (January): 244–264. ISSN: 08948755. doi:10.1175/JCLI-D-13-00272.1.

Perey, F. G. J., and E. R. Pounder. 1958. "CRYSTAL ORIENTATION IN ICE SHEETS." *Canadian Journal of Physics* 36 (April): 494–502. ISSN: 0008-4204, 1208-6045. doi:10.1139/p58-050.

Provost, Christine, Nathalie Sennéchael, Jonas Miguet, Polona Itkin, Anja Rösel, Zoé Koenig, Nicolas Villacieros-Robineau, and Mats A. Granskog. 2017. "Observations of flooding and snow-ice formation in a thinner Arctic sea-ice regime during the N-ICE2015 campaign: Influence of basal ice melt and storms: SNOW-ICE FORMATION IN THE ARCTIC." *Journal of Geophysical Research: Oceans* 122 (September): 7115–7134. ISSN: 21699275. doi:10.1002/2016JC012011.

Quartly, Graham D., Eero Rinne, Marcello Passaro, Ole B. Andersen, Salvatore Dinardo, Sara Fleury, Kevin Guerreiro, et al. 2018. "Review of Radar Altimetry Techniques over the Arctic Ocean: Recent Progress and Future Opportunities for Sea Level and Sea Ice Research." *The Cryosphere Discussions:* 1–51. doi:10.5194/tc-2018-148.

Rees, Gareth. 2006. *Remote Sensing of Snow and Ice.* 1st. Boca Raton, Florida.

Rémy, Frédérique, Thomas Flament, Aurélie Michel, and Denis Blumstein. 2015. "Envisat and SARAL/AltiKa Observations of the Antarctic Ice Sheet: A Comparison Between the Ku-band and Ka-band." *Marine Geodesy* 38 (September): 510–521. ISSN: 0149-0419, 1521-060X. doi:10.1080/01490419.2014.985347.

Ricker, R, S Hendricks, V Helm, H Skourup, and M Davidson. 2014. "Sensitivity of CryoSat-2 Arctic sea-ice freeboard and thickness on radar-waveform interpretation." *Cryosphere* 8:1607–1622. ISSN: 19940424. doi:10.5194/tc-8-1607-2014.

Ricker, Robert, Stefan Hendricks, Donald K Perovich, Veit Helm, and R??diger Gerdes. 2015. "Impact of snow accumulation on CryoSat-2 range retrievals over Arctic sea ice: An observational approach with buoy data." *Geophysical Research Letters* 42:4447–4455. ISSN: 19448007. doi:10.1002/2015GL064081.

Rignot, Eric, Keith Echelmeyer, and William Krabill. 2001. "Penetration depth of interferometric synthetic-aperture radar signals in snow and ice." *Geophysical Research Letters* 28 (September): 3501–3504. ISSN: 00948276. doi:10.1029/2000GL012484.

Röhrs, J., and L. Kaleschke. 2012. "An algorithm to detect sea ice leads by using AMSR-E passive microwave imagery." *The Cryosphere* 6 (March): 343–352. ISSN: 1994-0424. doi:10.5194/tc-6-343-2012.

Rosenzweig, Cynthia, David Rind, Andrew Lacis, and Danielle Manley. 2019. "Arctic Sea Ice and Its Role in Global Change." 1.

Rostosky, Philip, Gunnar Spreen, Sinead L. Farrell, Torben Frost, Georg Heygster, and Christian Melsheimer. 2018. "Snow Depth Retrieval on Arctic Sea Ice From Passive Microwave Radiometers—Improvements and Extensions to Multiyear Ice Using Lower Frequencies." *Journal of Geophysical Research: Oceans* 123 (October): 7120–7138. ISSN: 2169-9275, 2169-9291. doi:10.1029/2018JC014028.

Rothrock, D. A., and Mark Wensnahan. 2007. "The Accuracy of Sea Ice Drafts Measured from U.S. Navy Submarines." *Journal of Atmospheric and Oceanic Technology* 24 (November): 1936–1949. ISSN: 0739-0572, 1520-0426. doi:10.1175/JTECH2097.1.

Rothrock, D. A., Y. Yu, and G. a. Maykut. 1999. "Thinning of the Arctic sea-ice cover." *Geophysical Research Letters* 26:3469. ISSN: 0094-8276. doi:10.1029/1999GL010863.

Scagliola, M. 2013. "CryoSat footprints Aresys Technical Note": 8.

Schwarz, J., and W. F. Weeks. 1977. "Engineering Properties of Sea Ice." *Journal of Glaciology* 19:499–531. ISSN: 0022-1430, 1727-5652. doi:10.3189/S0022143000029476.

Schweiger, Axel, Jinlun Zhang, Ron Lindsay, Mike Steele, and Harry Stern. 2019. *PIOMAS Arctic Sea Ice Volume Reanalysis.*

Serreze, Marc C., and Julienne Stroeve. 2015. "Arctic sea ice trends, variability and implications for seasonal ice forecasting." *Philosophical Transactions of the Royal Society A: Mathematical, Physical and Engineering Sciences* 373:20140159. doi:10.1098/rsta.2014.0159.

Serreze, Mark C., and Walter N. Meier. 2019. "The Arctic's sea ice cover: trends, variability, predictability, and comparisons to the Antarctic: Variability, trends and predictability of sea ice." *Annals of the New York Academy of Sciences* 1436 (January): 36–53. ISSN: 00778923. doi:10.1111/nyas.13856.

Shokr, Mohammed, and Nirmal Sinha. 2015. *Sea ice: physics and remote sensing.* Geophysical monograph. Washington, D.C. : Hoboken, New Jersey: American Geophysical Union ; John Wiley & Sons. ISBN: 978-1-119-02789-8.

Smith, Doug M., James A. Screen, Clara Deser, Judah Cohen, John C. Fyfe, Javier García-Serrano, Thomas Jung, et al. 2018. "The Polar Amplification Model Intercomparison Project (PAMIP) contribution to CMIP6: investigating the causes and consequences of polar amplification." *Geoscientific Model Development Discussions* (June): 1–42. ISSN: 1991-962X. doi:10.5194/gmd-2018-82.

Smith, Thomas G., and Christian Lydersen. 1991. "Availability of suitable land-fast ice and predation as factors limiting ringed seal populations, Phoca hispida, in Svalbard." *Polar Research* 10 (January): 585–594. ISSN: 1751-8369. doi:10.3402/polar.v10i2.6769.

Stiles, W. H., and F. T. Ulaby. 1981. *Dielectric properties of snow.* Technical report. Greenbelt, Md. USA: NASA.

Sturm, Matthew, John Holmgren, and Donald K Perovich. 2002. "Winter snow cover on the sea ice of the Arctic Ocean at the Surface Heat Budget of the Arctic Ocean (SHEBA): Temporal evolution and spatial variability." *Journal of Geophysical Research* 107:8047. ISSN: 0148-0227. doi:10.1029/2000JC000400.

Thomas, David N, and Gerhard Dieckmann. 2010. *Sea ice.* Chichester, UK: Wiley-Blackwell. ISBN: 978-1-4443-1715-2.

Ulaby, F T, R K Moore, and A K Fung. 1982. *Microwave remote sensing: Active and passive. Volume 2-Radar remote sensing and surface scattering and emission theory.*

Vihma, Timo. 2014. "Effects of Arctic Sea Ice Decline on Weather and Climate: A Review." *Surveys in Geophysics* 35:1175–1214. ISSN: 01693298. doi:10.1007/s10712-014-9284-0.

Warren, Stephen G., Ignatius G. Rigor, Norbert Untersteiner, Vladimir F. Radionov, Nikolay N. Bryazgin, Yevgeniy I. Aleksandrov, and Roger Colony. 1999. "Snow depth on Arctic sea ice." *Journal of Climate* 12:1814–1829. ISSN: 08948755. doi:10.1175/1520-0442(1999)012<1814:SDOASI>2.0.CO;2.

Webster, Melinda A., Ignatius G. Rigor, Son V. Nghiem, Nathan T. Kurtz, Sinead L. Farrell, Donald K Perovich, and Matthew Sturm. 2014. "Interdecadal changes in snow depth on Arctic sea ice." *Journal of Geophysical Research: Oceans* 119 (August): 5395–5406. ISSN: 21699275. doi:10.1002/2014JC009985.

Weeks, W. F., and S. F. Ackley. 1986. "The Growth, Structure, and Properties of Sea Ice." In *The Geophysics of Sea Ice,* edited by Norbert Untersteiner, 9–164. Boston, MA: Springer US. ISBN: 978-1-4899-5354-4 978-1-4899-5352-0. doi:10.1007/978-1-4899-5352-0_2.

Weeks, W. F., and A. J. Gow. 1978. "Preferred crystal orientations in the fast ice along the margins of the Arctic Ocean." *Journal of Geophysical Research* 83:5105. ISSN: 0148-0227. doi:10.1029/JC083iC10p05105.

Weeks, W. F, and W. D Hibler. 2010. *On sea ice.* Fairbanks: University of Alaska Press. ISBN: 978-1-60223-101-6.

Willatt, Rosemary, Seymour Laxon, Katharine Giles, Robert Cullen, Christian Haas, and Veit Helm. 2011. "Ku-band radar penetration into snow cover on Arctic sea ice using airborne data." *Annals of Glaciology* 52:197–205. ISSN: 02603055. doi:10.3189/172756411795931589.

Woodhouse, Iain H. 2006. *Introduction to Microwave Remote Sensing.* 1st. Boca Raton, Florida: Taylor / Francis Group. ISBN: 978-0-415-27123-3.

Zygmuntowska, M., K. Khvorostovsky, V. Helm, and S. Sandven. 2013. "Waveform classification of airborne synthetic aperture radar altimeter over Arctic sea ice." *Cryosphere* 7:1315–1324. ISSN: 19940416. doi:10.5194/tc-7-1315-2013.

Appendix A

Retracker Threshold Selection Analysis

A.1 March 23rd Runway Calibration

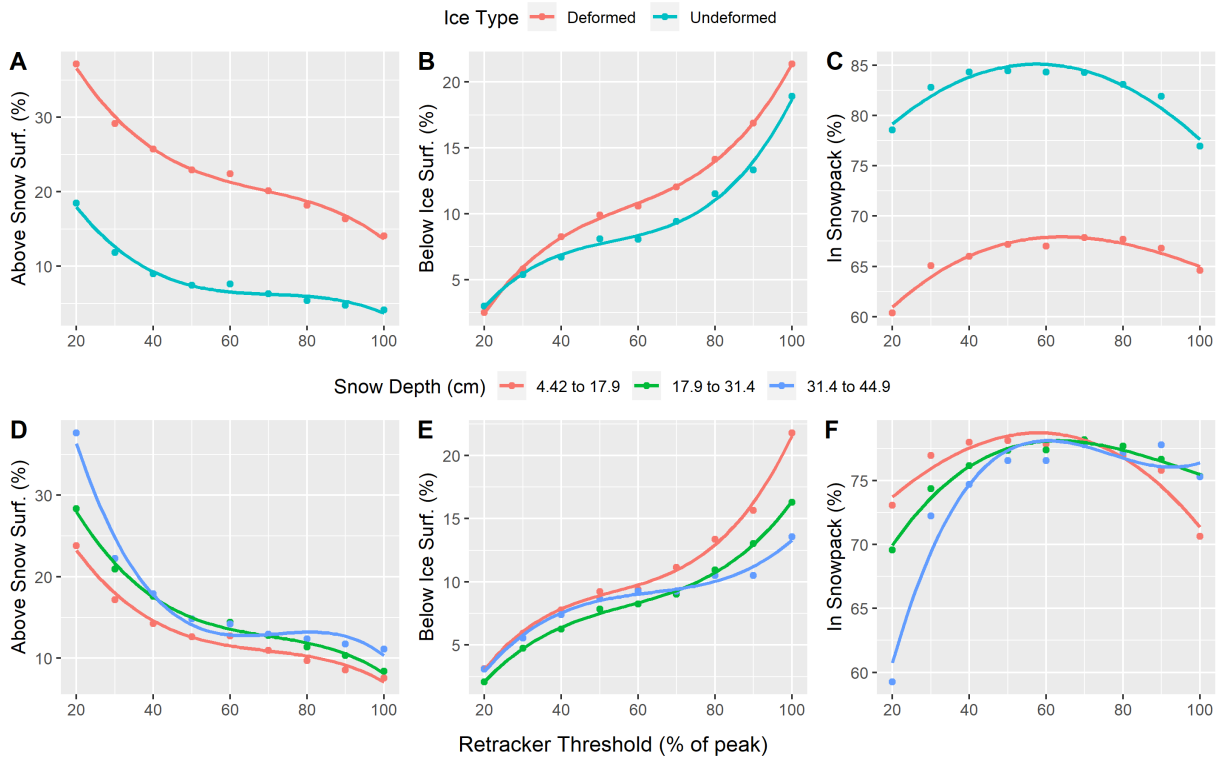

Figure A.1: Proportion of retracked scattering surfaces (s_r) located above the snowpack, below the ice surface and within the snowpack. Proportions are shown across retracker threshold selections for evenly stratified categories of surface characteristics A-C) ice deformed classification D-F) snow depth

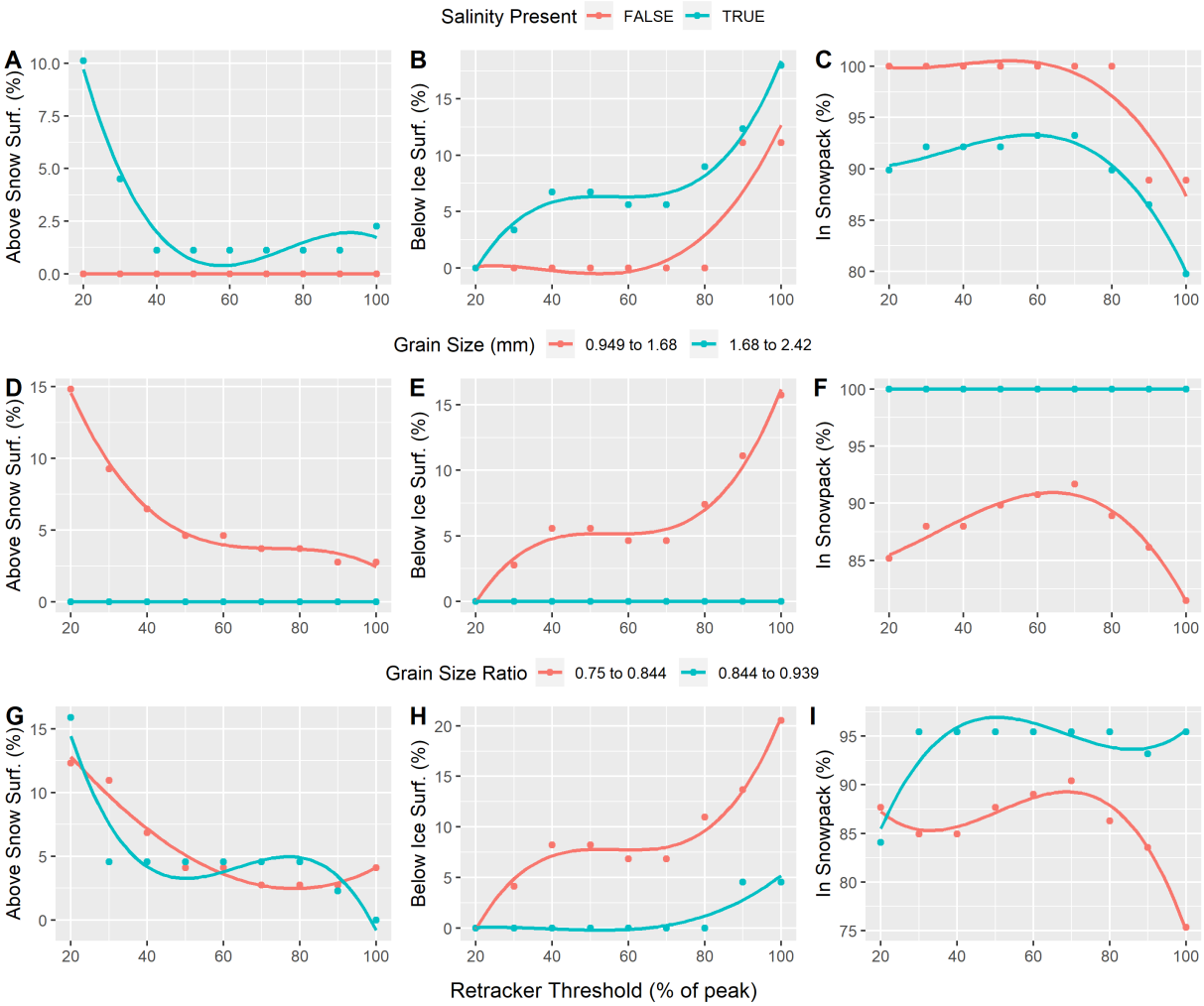

Figure A.2: Proportion of retracked scattering surfaces (s_r) located above the snowpack, below the ice surface and within the snowpack. Proportions are shown across retracker threshold selections for evenly stratified categories of snow pit characteristics A-C) presence of salinity in the snowpack D-F) average snow grain size G-I) snow grain size ratio (between smallest and largest diameter of selected grains)

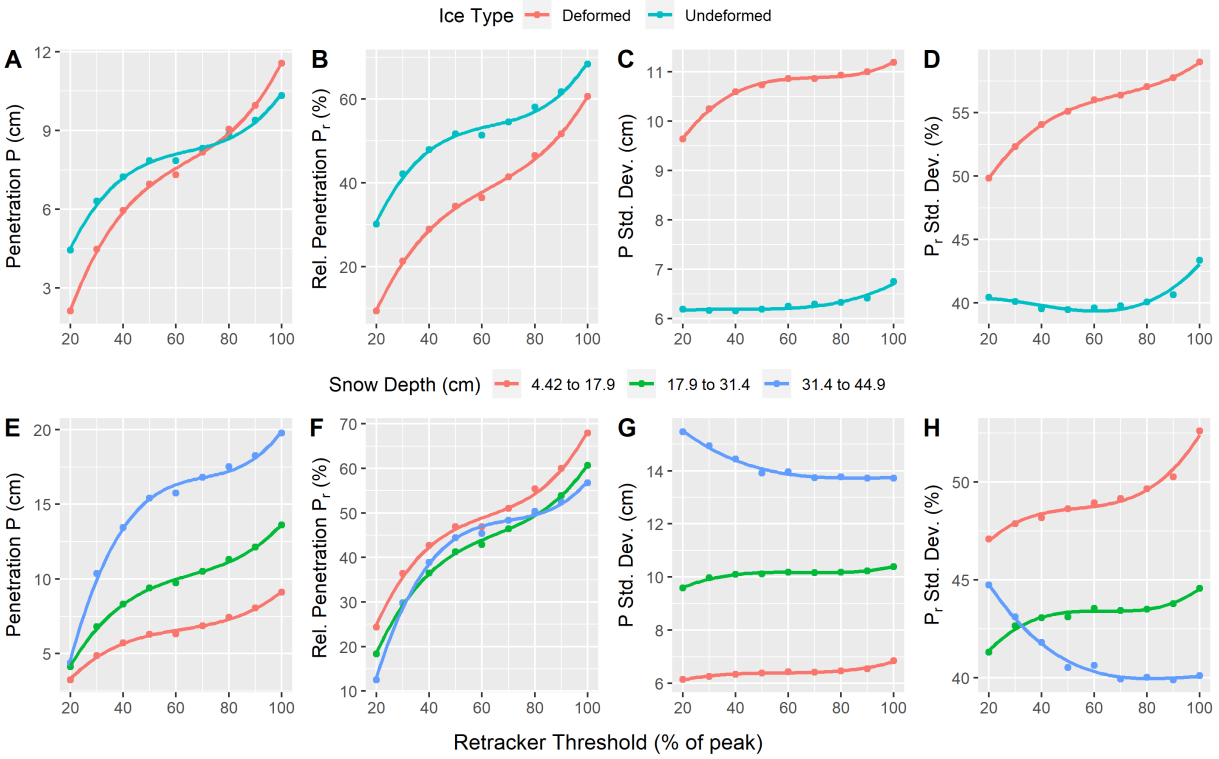

Figure A.3: Mean and standard deviation of the estimated penetration P and penetration relative to the snowpack depth P_r across retracker threshold selections for evenly stratified categories of surface characteristics A-D) ice deformed classification D-F) snow depth

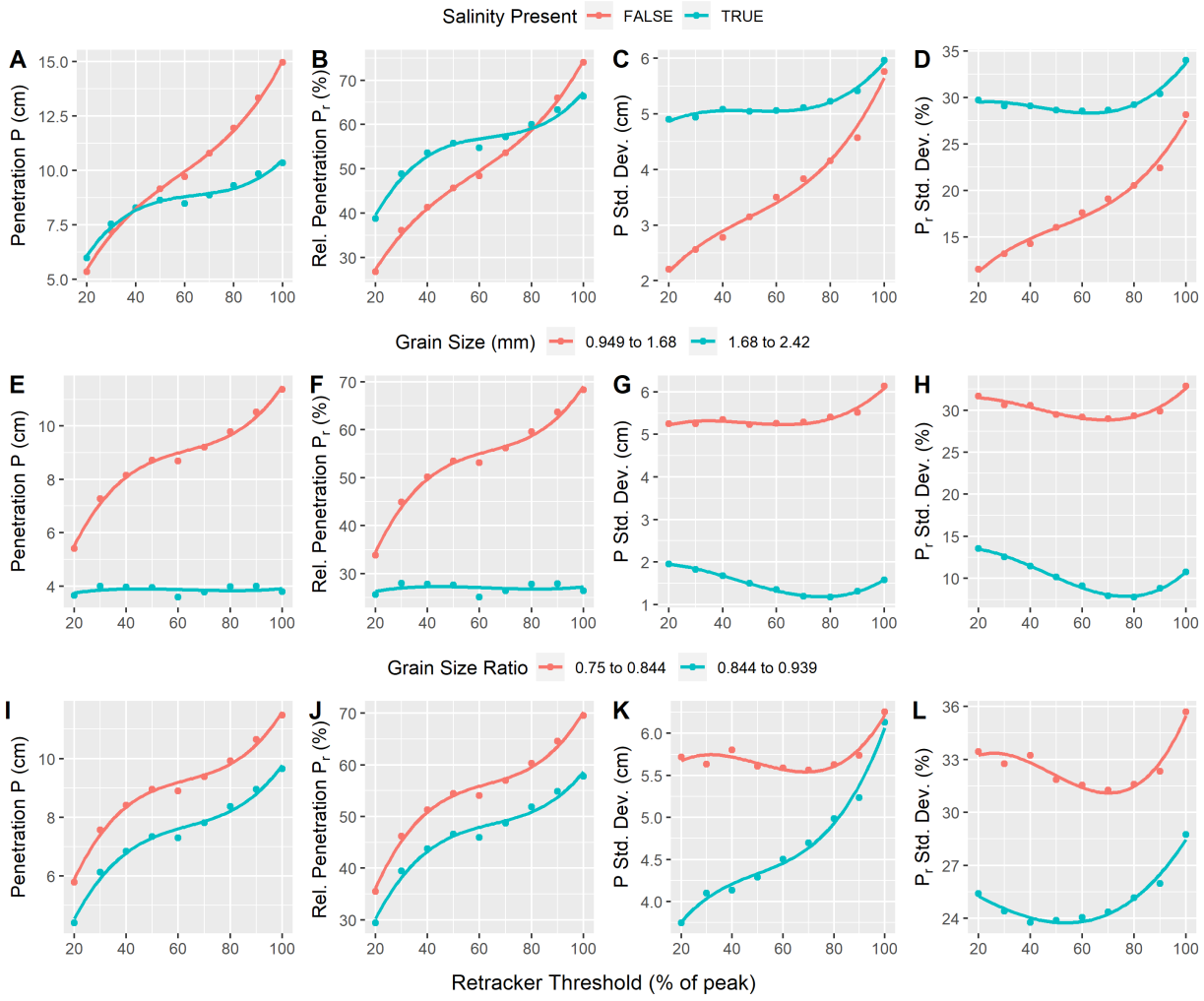

Figure A.4: Mean and standard deviation of the estimated penetration P and penetration relative to the snowpack depth P_r across retracker threshold selections for evenly stratified categories of snow pit characteristics A-C) presence of salinity in the snowpack D-F) average snow grain size G-I) snow grain size ratio (between smallest and largest diameter of selected grains)

A.2 March 26th Runway Calibration

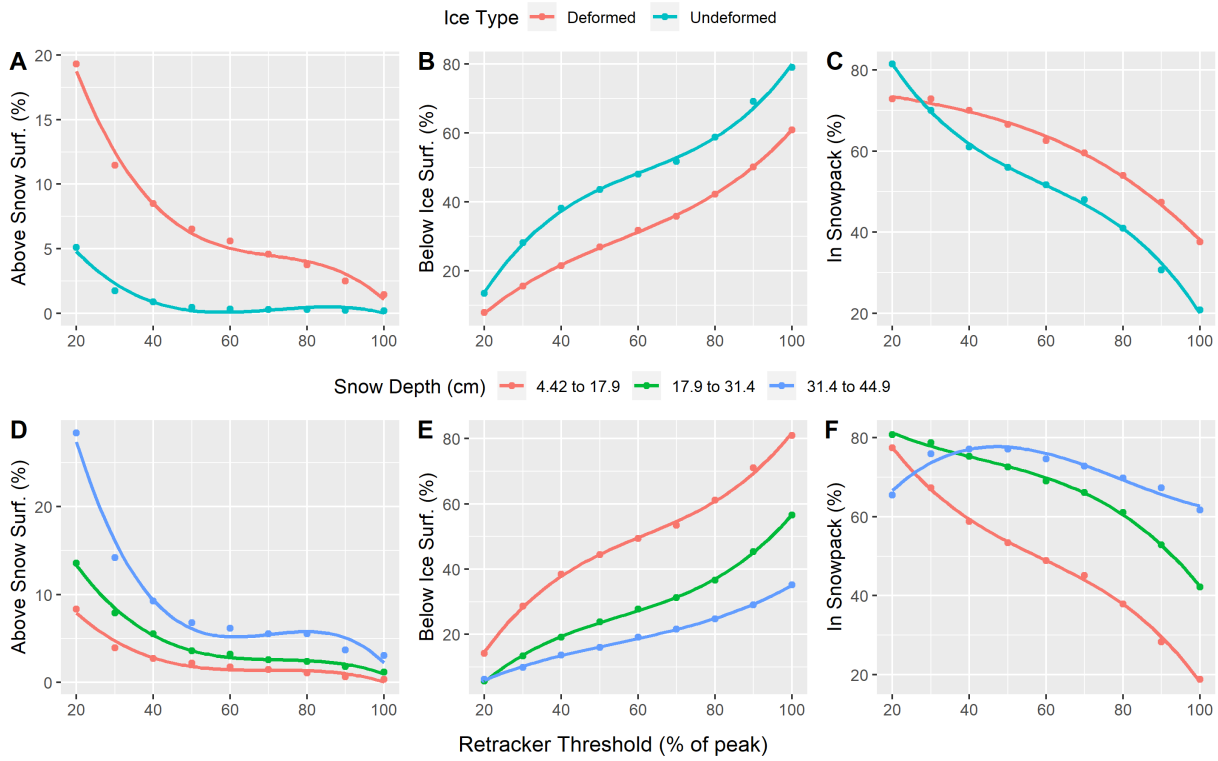

Figure A.5: Proportion of retracked scattering surfaces (s_r) located above the snowpack, below the ice surface and within the snowpack. Proportions are shown across retracker threshold selections for evenly stratified categories of surface characteristics A-C) ice deformed classification D-F) snow depth

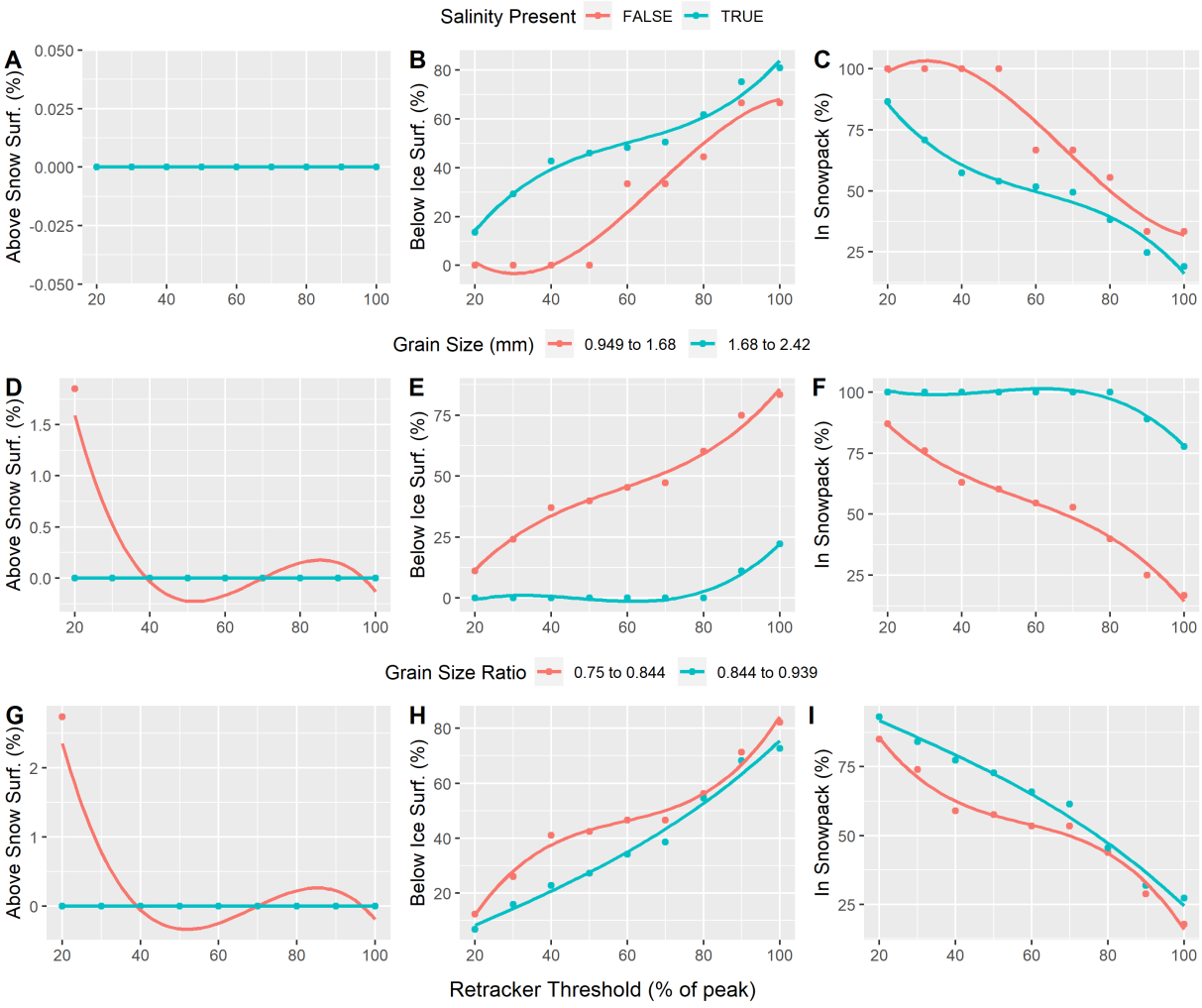

Figure A.6: Proportion of retracked scattering surfaces (s_r) located above the snowpack, below the ice surface and within the snowpack. Proportions are shown across retracker threshold selections for evenly stratified categories of snow pit characteristics A-C) presence of salinity in the snowpack D-F) average snow grain size G-I) snow grain size ratio (between smallest and largest diameter of selected grains)

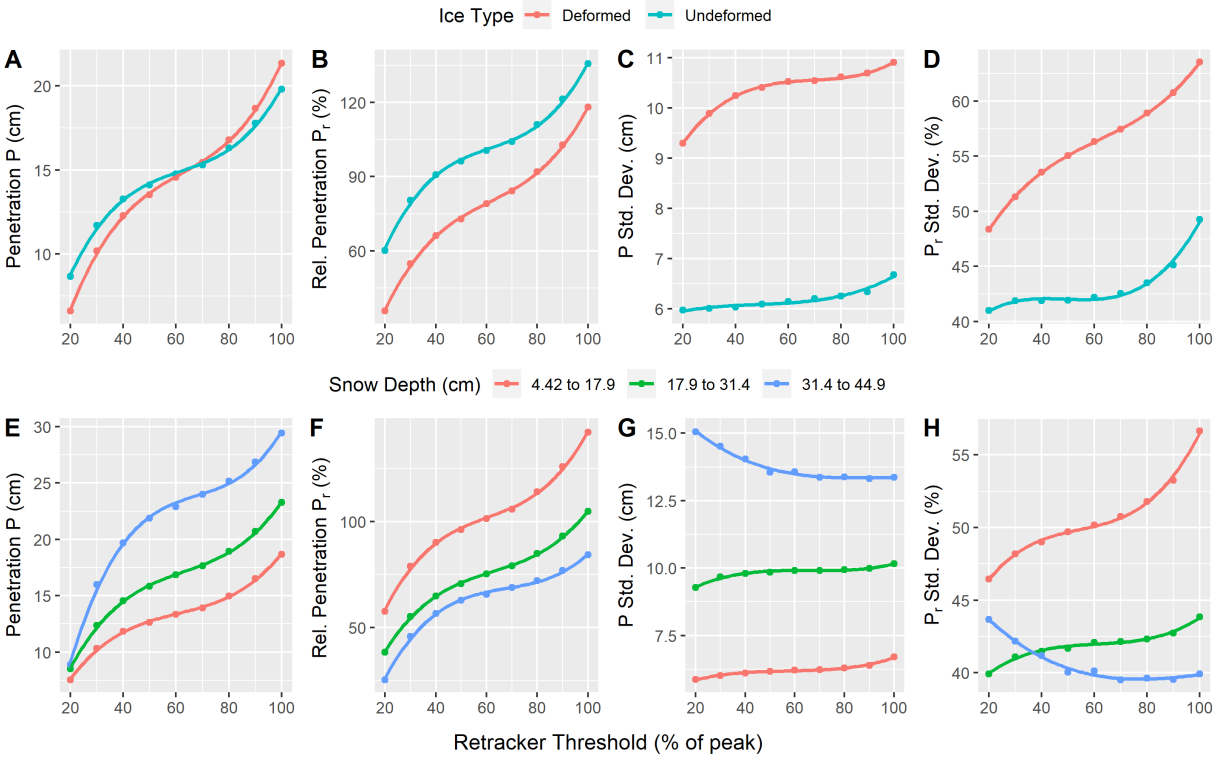

Figure A.7: Mean and standard deviation of the estimated penetration P and penetration relative to the snowpack depth P_r across retracker threshold selections for evenly stratified categories of surface characteristics A-D) ice deformed classification D-F) snow depth

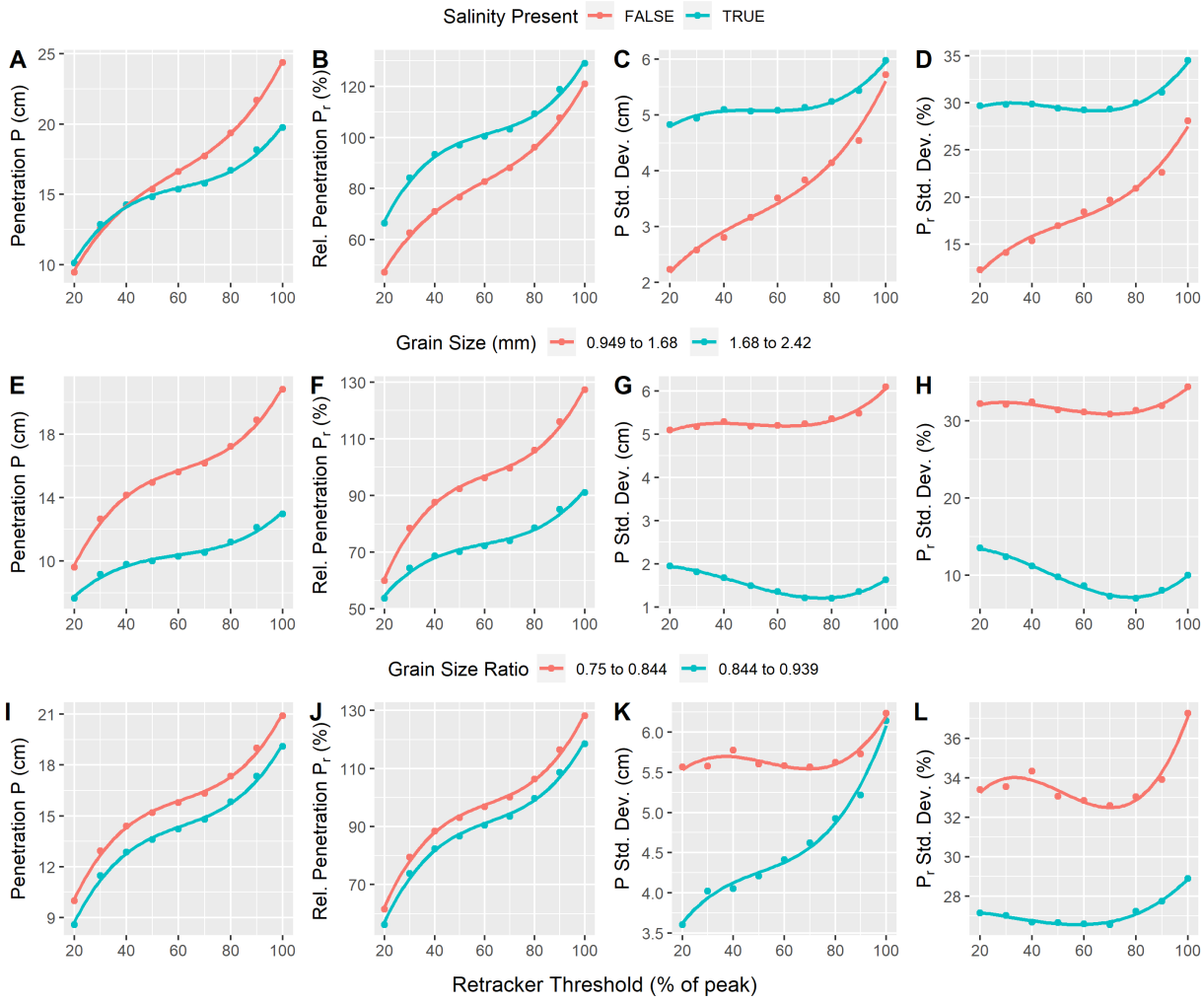

Figure A.8: Mean and standard deviation of the estimated penetration P and penetration relative to the snowpack depth P_r across retracker threshold selections for evenly stratified categories of snow pit characteristics A-C) presence of salinity in the snowpack D-F) average snow grain size G-I) snow grain size ratio (between smallest and largest diameter of selected grains)

Appendix B

Surface Observations Semivariograms

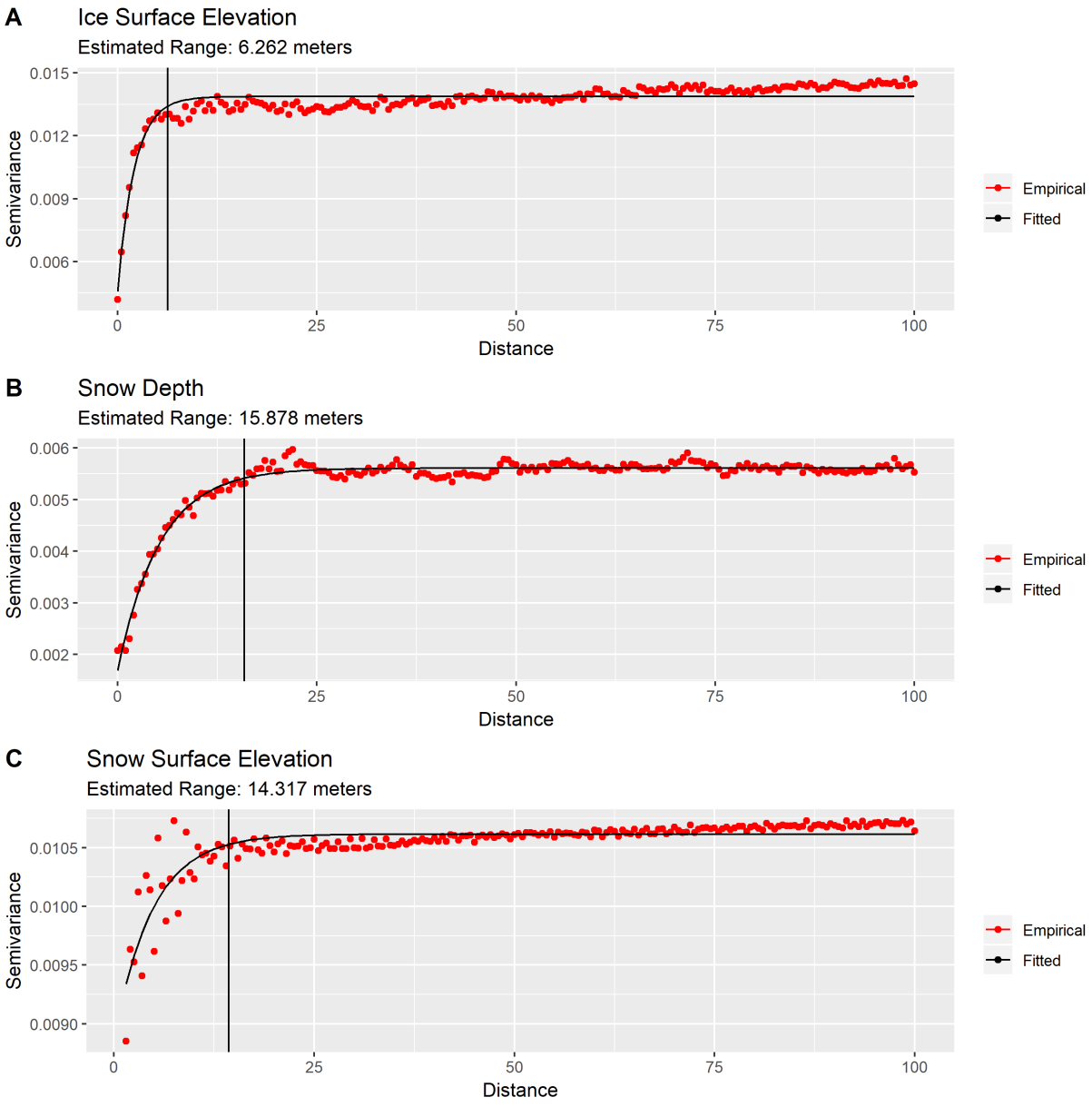

Figure B.1: Semivariogram for A) ice surface elevation B) snow depth and C) snow surface elevation within the Grid 3 zone. Fitted using an exponential model $f(x) = (s-n)(1-e^{\frac{-x}{\alpha r}}) + n$ where s is the sill, n is the nugget and r is the range, with an α of 1/3 (Chiles and Delfiner, 2012)